Energy transfer dynamics in luminescent Eu^{3+} complexes adsorbed on dielectric and metallic substrates

Zur Erlangung des akademischen Grades eines

Doktors der Naturwissenschaften

von der Fakultät für Physik
des Karlsruher Instituts für Technologie
genehmigte

Dissertation

von

Adrian Ebert, M.Sc.

aus Rosenheim

Datum der mündlichen Prüfung:	08. Mai 2026
Referent:	Prof. Dr. Wulf Wulfhekel
Korreferent:	Prof. Dr. David Hunger

Dedicated to my late grandfather, Giancarlo Senese.

Contents

1 Introduction

Human curiosity has always driven the desire to understand the world we live in. It was therefore inevitable that questions would sooner or later arise asking about what is beyond our direct comprehension, be it the origin of our universe, the movement of celestial bodies, or the smallest building blocks of everything that exists. Answering these questions that we would now attribute to the field of physics were as fundamental as unraveling the very nature of humanity. It is therefore of no surprise that the same group of intellectuals - early philosophers - addressed these problems. Leucipus and his student Democritus, who lived at the same time as the famous philosopher Socrates in the 5th century BC, reduced existence down to two things: the void and matter. They suggested that matter consists of tiny objects that cannot be divided further, hence the name atom - indivisible. Now, over two thousand years later, we have proof, that the objects we still call atoms are in fact not indivisible. The existence of even smaller, sub-atomic particles was proven experimentally at the beginning of the 20th century by tracking their traces in a cloud chamber. The invention of the scanning tunneling microscope (STM) by G. Binnig and H. Rohrer in 1981, which awarded them the Nobel price in physics, allowed to not only visualize atomic structures on conducting surfaces but also give insight in their electron density. Finally, we do not need to speculate anymore. Molecular orbitals and covalent bonds can now be grasped by eye, albeit with the help of electronics.

The downsizing of electronic devices is driven by the insatiable desire to increase computational power per volume. Moore's law famously states that the amount of transistors within integrated circuits doubles in regular time intervals. It was therefore only a question of time until integrated circuits reach the nanoscale. Addressing single molecules is of paramount importance for developing devices on the nanoscale and increasing their efficiency. The ultimate goal is an electronically controlled device consisting of a single molecule. Prominent examples include the conversion of electricity into light by a single photon light source [1] or the construction of graphene based transistors [2, 3]. This thesis discusses STM for imaging light sensitive organic molecules as well as graphene based molecules.

My journey as a PhD. student began in the group of Prof. Axel Enders at the University of Bayreuth where I investigated graphene nano ribbons (GNRs). A single graphene sheet consists of a hexagonal lattice of carbon atoms. Such a sheet can be separated from a graphite crystal with adhesive tape by pulling an individual graphene layer off of the crystal as was shown in the ground braking work of K. S. Novoselov et al. in 2004, already demonstrating the electric field effect in graphene layers [4]. GNRs can be thought of as a strip that is cut out of the graphene sheet. Early reports for manufacturing GNRs indeed used lithography methods, such as unzipping carbon nano tubes [5] or masking graphene with

nanowires followed by edging away material [6]. Later, the so called bottom-up-approach was developed by J. Cai et al. in 2010 [7]. This method allows to manufacture GNRs out of molecular building blocks, referred to as precursors. Precursors are monomers, which means repetition units out of which polymers can be formed. The precursors are usually organic molecules with halogen atoms attached at specific positions. When the halogen-carbon bond breaks, the resulting unpaired electron is free to connect with the unpaired electron of another precursor, thus inducing polymerization. The precursors can be deposited on a metal substrate and polymerization subsequently induced by heating. Polymers are characterized by individual sites, e.g. phenyl groups attached to a polymeric backbone. The phenyl groups are terminated with hydrogen atoms. The carbon-hydrogen bonds break upon additional heating, again creating unpaired electrons. The unpaired electrons of different phenyl groups may form a bond. Now, the molecule is no longer characterized by a polymeric backbone with individual phenyl sites, but by a system of interconnected carbon atoms with an extended system of delocalized electrons - a GNR. The formation of a GNR by heating of a polymer is called cyclodehydrogenation. This bottom-up-approach opens the possibility for on-surface synthesis, which means depositing precursors on a single crystal substrate followed by inducing polymerization and cyclodehydrogenation. This preparation method is ideal for preparing samples suitable for STM.

GNRs usually have the shape of a ribbon, which means a long and a narrow side. The confinement of electrons along the narrow side leads to a quantization of the possible energies the electron can have, analogous to the theoretical model of a particle in a potential well. The distance between the possible energy values, specifically between the valence- and conduction band defines the bandgap of the GNR. It can be modified by changing the GNR width [8–11], its edge structure [12–14], doping [15, 16] or creating nanopores within the carbon lattice [17–20]. The possibility to modify the properties of GNRs makes them highly attractive for applications in quantum electronics [21–23], as well as spintronic [12, 24, 25] and optoelectronic [26–28] devices.

The first precursors used for the bottom-up-approach are called C90 due to their 90° degree bonding angle [7]. The C refers to the chevron style GNRs obtained from these precursors. T90-molecules are a truncated version of C90 that open the possibility to grow GNRs with periodic notches, therefore influencing the edge state [29, 30]. C30-precursors, another variant of C90, featuring a 30° degree bonding angle has found application in manufacturing OLED devices [31, 32]. The 30° degree bonding angle also allows to manufacture GNRs with nanopores that were shown to induce a state localized at the pores influencing the bandgap [18, 33]. T30-precursors are a truncated version of C30 that allow to manufacture porous GNRs with armchair edge [18, 20, 33].

The research done on GNRs is presented in chapter 4. It provides an in depth introduction to the concept of graphene and GNRs, outlining the underlying solid state physics, on-surface synthesis via the bottom-up-approach (section 4.1) and methods for modifying the bandgap (section 4.2). Furthermore, the experimental set-up for sample characterization (section 4.3.1) and preparation via direct contact transfer (DCT) and electro-spray

deposition (ESD) (section 4.3.2) is briefly described. The experimental results focus on the polymeric phase of T90-molecules [33] (section 4.4.1), the growth and electronic properties of T30-GNRs, the possibility of creating heterostructures from T30- and C30-precursors, and the self-assembly of C30-4Br-precursors and GNRs.

The research conducted as part of the group of Prof. Wulf Wulfhekel at KIT focuses on light emission from Eu^{3+} complexes. Eu^{3+} complexes are molecules consisting of an Eu^{3+} ion incorporated in an organic structure. The structure can consist of ligands attached to the Eu^{3+} core or the Eu^{3+} ion can be incorporated in a chelating scaffold. In both cases, the surrounding structure has to oxidize Eu to its trivalent form while also facilitating the interaction of light with the Eu^{3+} core. The latter aspect is necessary due to the electronic structure of Eu^{3+} ([Xe] $4f^6$). The orbitals of the 4f shell, while being the highest in energy, do not extent farthest from the center of the Eu^{3+} ion. Instead it is shielded by the 5s and 5p orbitals. This shielding reduces the interaction of the Eu^{3+} ion with its surrounding, which decreases the probability to excite it with light. The probability for excitation is further reduced by the fact that the main transitions happen within the 4f shell which makes them forbidden according to Laporte selection rules [34]. However, exactly these properties which reduce the excitation probability also lead to unique photophysical properties which make Eu^{3+} complexes worth investigating. All emission spectra of different Eu^{3+} complexes have a characteristic signature. The differences among the emission of different complexes are comparatively minor due to the Eu^{3+} center being shielded and therefore less sensitive to their chemical and optical environment than other chromophores. The minor differences in the emission spectra from different complexes give insight in the local order and electronic properties of the Eu^{3+} environment [34–39].

The emission spectrum arises from individual transitions that emit photons when radiatively decaying from an excited state to a state with lower energy. Populating an excited state can be done by light, the emission is then called photoluminescence (PL). The excitation involves the coupling of the dipole moment of the complex to the dipole moment of the excitation light. Usually, the coupling to the dipole moment of the electric mode of the electromagnetic field of light is stronger than the coupling to the magnetic mode. For this reason, the transitions are called induced electric dipole (ED) transitions. However, emission from Eu^{3+} has the unique property of having one magnetic dipole (MD) transition that is considered insensitive to the environment of the Eu^{3+} ion to such an extent that its emission can be used as a reference for normalizing the emission spectrum. The relative intensities of individual emission bands can thus be compared across samples.

PL spectra are an important tool to determine the chemical environment and symmetry of the first coordination sphere of the Eu^{3+} ion and can already provide insights in the overall emission intensity. However, to understand the dynamics of excitation, charge transfer and emission, the decay of the PL intensity after excitation needs to be tracked. This is done by the method of time correlated single photon counting (TCSPC). Tracking the PL decay allows to determine the total transition rate and observed lifetime of the excited state. The total transition rate is determined by radiative and non-radiative processes. Non-radiative

de-excitation processes reduce the luminescence intensity. This is referred to as quenching. In the context of complexes adsorbed on metal surfaces, which means samples suitable for STM measurements, quenching mechanisms include charge transfer [40] by electron transport from complex to metal and vibrational relaxation [41–44]. The de-excitation of an excited state can also lead to the excitation of electron-hole pairs [45] and image charge oscillations [46] in the metal, surface plasmons [47, 48], or, in the context of STM, gap plasmons [49] which may dissipate and therefore not contribute to the luminescence intensity. However, the transition rate is also influenced by many factors for complexes that are not near a metal surface. The refractive index of the surrounding medium and the photonic density of states has for example to be taken into account [34, 50–53]. Furthermore, vibrational relaxation can lead to de-excitation [41–44].

To investigate luminescence of complexes adsorbed on substrates in ultrahigh vacuum (UHV) conditions, a modified version of an STM is used. A normal STM uses a sharp metallic tip to probe the surface of the substrate. In the STM used here, the tip is incorporated in the center of a parabolic mirror. Tip and mirror are microfabricated as a solid piece by the direct laser writing (DLW) approach developed by the group of Prof. Wegener at KIT [54–57]. Using this special tip allows to collect light emitted in the tunnel junction without the need to use lenses that cover a smaller solid angle and require adjustment. The STM is referred to as γ-STM [58, 59]. It was used in previous work to collect light from molecules excited by tunneling electrons [60–62]. Furthermore, a second PL set-up was built and added to the UHV system that allows to collect luminescence from complexes on substrates in UHV without needing to use the STM. It was mostly used for investigating thin films of complexes on dielectric substrates at room temperature.

Chapter 2 provides the theoretical context, describing the working principles of an STM and the concept of quantum tunneling as the underlying principle for scanning tunneling microscopy and scanning tunneling spectroscopy (section 2.1). Furthermore, the concept of electro-luminescence is introduced (section 2.2). The theory of transition rates as determined by Fermi's golden rule is discussed together with the factors influencing transition rates, such as plasma oscillations, and dipole emission in front of metallic surfaces, highlighting the difference in transitions induced by coupling to the electric and magnetic modes of light (section 2.3). A description of the contributions to the transition rate and the observed lifetime is provided (section 2.5). The emission spectrum of Eu^{3+} and the transitions involved are detailed (section 2.6) and Judd-Ofelt (JO) theory introduced as a powerful tool for analyzing emission spectra (section 2.7). Finally the ligand antenna effect explains the idea behind the structure of Eu^{3+} complexes (section 2.8).

The experimental details and results focusing on Eu^{3+} complexes are presented in chapter 3. The experimental set-ups consisting of the UHV system, the γ-STM and the optical set-up for PL and TCSPC are described in detail (section 3.1). The section on sample preparation (section 3.2) details the steps of substrate cleaning as well as the deposition methods of thermal sublimation and vacuum spray deposition. Furthermore, the full names and structure drawings of all complexes are listed.

The experimental results start with STM topography data of the betadiketonate based complexes [Eu(tta)$_3$(bpy)], [Eu(btfa)$_3$(bpy)] and [Eu(tta)$_3$(H_2O)$_2$] (section 3.3), highlighting the importance of controlled material deposition via sublimation and purification of the material by degassing. Furthermore, STM topography data of the trensal based complexes [Eu(trensal)], [Eu(trensal-O-Bn)], [Eu(trensal-Ph-SMe)] and the platform complex [Tb(TACN)] prepared via sublimation and vacuum spray deposition is shown (section 3.4). This is followed by a brief outline of the experiments performed on obtaining electroluminescence from Eu^{3+} complexes (section 3.5).

The most important results focus on the photophysical properties of Eu^{3+} complexes. First, a method to perform TCSPC experiments at different wavelenghts with a single 30 ps excitation pulse inside the STM is established (section 3.6.2). It is shown that the PL decay of thin films on metal substrates does not depend on the distance between sample and mirror tip. Furthermore, measurement artifacts within the first 200 ns after excitation are demonstrated. Afterwards, PL spectra and lifetimes of [Eu(tta)$_3$(bpy)], [Eu(btfa)$_3$(bpy)] and [Eu(tta)$_3$(H_2O)$_2$] in drop-casted and sublimed films on glass substrates are presented, supplemented by TCSPC measurements of powder samples and molecules in solution. The results are quantified by estimating the radiative and non-radiative lifetimes derived from JO analysis (section 3.6.1). Vibrational relaxation due to OH-vibrations are pointed out as a major quenching process. Furthermore, the impact of the medium surrounding the Eu^{3+} ion is demonstrated and inhomogeneous film growth leading to line broadening in the emission spectra is discussed. Investigating the stability of complexes under UV illumination (section 3.6.3) indicates that the photo-bleaching probability is not sufficient for extended single molecule experiments. Advancing from material in bulk and solution, PL spectra and lifetimes of [Eu(tta)$_3$(bpy)], [Eu(btfa)$_3$(bpy)] and [Eu(trensal)] in thin films (∼20 nm) on dielectric and metallic substrates are discussed (section 3.6.4). The structural difference between [Eu(trensal)] and the betadiketonate based complexes [Eu(btfa)$_3$(bpy)] and [Eu(tta)$_3$(bpy)] was found to make the former more susceptible to structural changes upon sublimation as can be seen in the emission and decay data. Furthermore, investigating the PL decay at different wavelengths with the established single pulse TCSPC method reveals the charge transfer mechanisms within betadiketonate and trensal complexes (section 3.6.5). It was found that the energy is first transferred from the ligands of the Eu^{3+} complex to higher excited states of Eu^{3+} and not directly to its first electronic state from which the main emission takes place. Finally, the photophysical properties of [Eu(tta)$_3$(bpy)] films with different thicknesses down to 2.8 nm are probed therefore enabling to determine the energy transfer rate to the metal substrate (section 3.6.6).

2 Theoretical background

This chapter provides an introduction to the working principle of an STM, briefly describing its historical context and pointing out its relevance for modern physics. The idea of quantum tunneling is treated mathematically in the general case, as well as in the context of STM. Different ways of charge transfer and luminescence induced by tunneling electrons are described. Since this work does not only focus on STM but also on luminescence, the quantum mechanical principles of radiative transitions are provided putting a special focus on light being emitted inside the STM cavity. The manifold transitions of Eu^{3+} are described in detail, pointing out the characteristics of the resulting emission spectra. Furthermore, extracting information from the spectra by utilizing Judd-Ofelt theory is demonstrated.

2.1 Scanning tunneling microscopy

Microscopy based on optical imaging is limited by Abbe's law [63]. This law states that the features of an object need to be at least of the size of $d = \frac{\lambda}{2\mathrm{NA}}$ to be resolved with optical imaging methods. λ describes the wavelength of the light used for imaging, while NA refers to the numerical aperture. Imaging methods that do not rely on conventional optics have been developed that are able to circumvent this limit. In 1986 G. Binnig and H. Rohrer were awarded the Nobel price in physics for developing the first scanning tunneling microscope [64]. While the set-up became more and more refined over the years, the basic components and the working principle remained the same. A sharp electrically conducting tip is positioned in proximity to the sample to be investigated. A bias voltage is applied between the tip and the sample and the distance between them decreased to about 100 pm until a tunneling current sets in.

An electric current in general refers to the amount of charge being transported per time. The tunneling current describes the amount of electrons being transported per time by quantum tunneling. It depends exponentially on the width of the tunneling gap but also on the density of states in the tip and the sample. An STM utilizes this exponential dependence to probe molecular structures in the picometer regime. The most common imaging method in STM is the constant current mode (Fig. 2.1). The tip scans across an area on the surface of the sample typically ranging between 5 and several 100 nm. The tunneling current is kept constant by a feedback loop that controls the piezo elements moving the tip. This way, the size of the gap between tip and sample is adjusted by moving the tip in z-direction. However, the tunneling condition depends not only on the position of the atomic cores modifying the width of the gap, but also on their electron density. In constant current mode, the z-position of the tip therefore corresponds to surfaces of constant electron density. The STM image

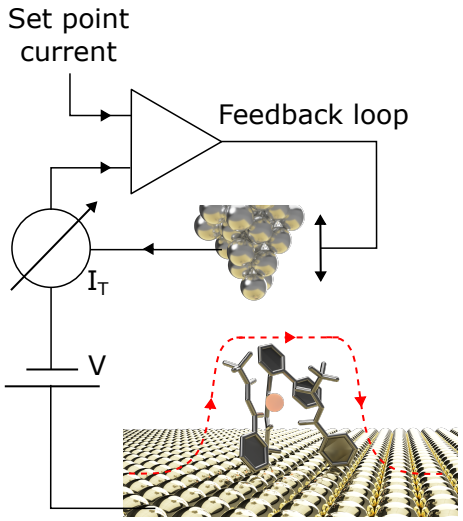

Figure 2.1: Illustration of the working principle of an STM. A bias voltage V is applied between the tip and the sample to create a net tunneling current I_T. The tip-sample distance is adjusted by the feedback loop so the tunneling current matches the set point current.

is created by displaying the values of the z-position of the tip for each data point of the scan area. The resulting data is called apparent height. In this work, all STM topography images are edited by leveling the background, filtering noise and choosing a suitable color scale.

2.1.1 Quantum tunneling in the context of STM

When two materials with different Fermi energies are brought into close contact, quantum tunneling occurs, when the wavefunctions of the electrons in both materials overlap. Electrons will then tunnel from the material with higher Fermi energy to the material with lower Fermi energy until the density of states of both materials are equally filled and equilibrium is reached. A continuous net tunneling current can be achieved when the Fermi energies of both materials are shifted by applying a bias voltage V_B. As displayed in Fig. 2.2 a), the wave function propagates through the material with higher Fermi energy E_F, decays exponentially in the potential barrier and continues propagation in the second material, with E_F being shifted by eV_B. Φ describes the work function of the tip and E_n the energy of the tunneling electrons. This situation can be described mathematically by considering the wavefunction $\psi(z)$ of the electron that satisfies the one dimensional time independent Schrödinger equation:

$$E\psi(z) = -\frac{\hbar^2}{2m}\frac{d^2\psi(z)}{dz^2} + U(z)\psi(z) \tag{2.1}$$

$U(z)$ is the potential barrier, m the mass of the electron, and $\hbar$ the reduced Planck constant. The solution of this differential equation is given by $\psi(z) = \psi(0)e^{\pm ikz}$, when $E > \mid U(z) \mid$, which is the case outside of the potential barrier, k is then given by:

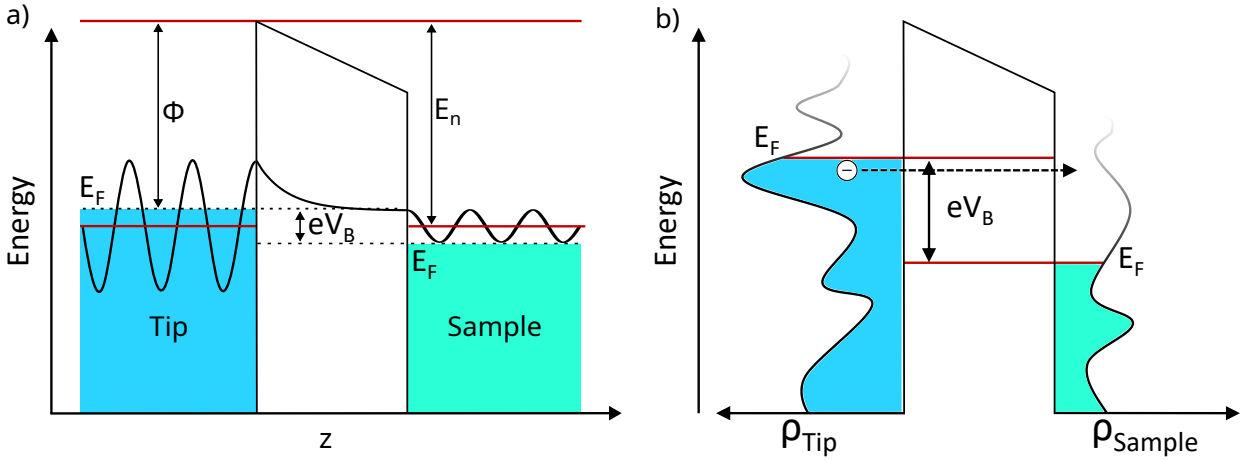

Figure 2.2: Schematic illustration of: a) An electron wave function tunneling through a potential barrier. E_F of the tip and E_F of the sample are shifted by eV_B. Φ is the work function of the tip and E_n is the energy of the tunneling electrons. After [65]. b) An electron tunneling from the STM tip to the sample. The Fermi energies E_F of tip and sample are shifted by the bias voltage V_B. ρ_{Tip} and ρ_{Sample} describe the density of states of the tip and the sample. After [33].

$$k = \frac{\sqrt{2m(E - U(z))}}{\hbar}. \tag{2.2}$$

$\psi(z)$ then has the form of a plane wave. Inside the barrier, where $E < U(z)$, the solution is $\psi(z) = \psi(0)e^{-\kappa z}$ with κ given by:

$$\kappa = \frac{\sqrt{2m(U(z) - E)}}{\hbar}, \tag{2.3}$$

This solution describes a declining exponential function with decay constant κ.
In reality, the density of states varies for different materials with energy as schematically shown in Fig. 2.2 b). For the tunneling process in an STM, the density of states of the tip is usually assumed to be flat such that the density of states of the sample can be probed. The tunneling current can be described by Bardeen's formula [65].

$$I_T = \frac{4\pi}{\hbar} \int_0^{eV} \rho_{\text{Tip}}(E_F - eV_B + \epsilon)\rho_{\text{Sample}}(E_F + \epsilon) \mid M \mid^2 d\epsilon \tag{2.4}$$

ρ_{Tip} and ρ_{Sample} describe the density of states of the tip and the sample, E_F the Fermi energy, and M describes the tunneling matrix element. This model was simplified by J. Tersoff and D. R. Hamann [65] who suggested that the wave function of the tip can be assumed to be spherical because only the contributions of the s orbital of the outermost atom of the tip need to be considered. Furthermore, the variation of the density of states of the tip is considered to be negligible in the energy range of interest. This leads to Tersoff and Hamann's simplified description of the tunneling current [65]:

$$I_T \propto \int_0^{eV_B} \rho_{\text{Sample}}(E_F + \epsilon, \mathbf{r}_0) d\epsilon. \tag{2.5}$$

With these simplifications, the tunneling current is directly proportional to the density of states of the sample.

2.1.2 Scanning tunneling spectroscopy

Scanning tunneling spectroscopy (STS) allows measuring the electronic density of states of the investigated material. In STM, the bias voltage is fixed and the distance between tip and sample adjusted to keep the tunneling current constant while scanning across an area. The obtained data then contains information about the topography of the sample and its density of states in this area. In STS, the tip is positioned stationary, and the bias voltage swept while the current is recorded. The derivative of this $I(V)$ data with respect to the applied bias voltage is the differential conductance dI/dV which is proportional to the probed density of states (see Eq. 2.5). STS usually refers to point spectra but also an image of the differential conductance can be taken when the DC bias voltage is overlaid with an AC modulation to probe the states at the DC±AC interval. The tunneling current then responds with an oscillation of the same frequency as the bias modulation. Using the lock-in technique, the states within the modulation range can be probed. The obtained image of the differential conductance is referred to as a dI/dV-map.

2.2 Electro-luminescence

Electro-luminescence (EL) describes the process of converting electricity into light. While it is not the primary focus of this work, it will be discussed briefly. EL offers a wide range of applications and is therefore desirable to achieve with any light sensitive molecule. It seems obvious to perform EL experiments, when considering light emitting molecules inside a tunneling junction. The γ-STM used in this thesis was indeed used successfully for that in the past [60–62]. However, EL inherently requires some degree of conductivity which means charge carrier transport. Light emission on the other hand, requires some electronic decoupling between molecule and substrate. This is explained by Fig. 2.3. A molecule adsorbed on the surface may hybridize with the sample (Fig. 2.3 a)). For this reason, the HOMO is below the Fermi energy of the substrate. The Fermi energy of the tip is shifted with respect to the Fermi energy of the substrate by the product of bias voltage and elementary charge eV_B. At suitable bias voltage, the LUMO of the molecule is at the Fermi energy of the tip, which allows an electron to tunnel from the tip through the vacuum barrier and then through the molecule into an empty state (hole) in the substrate. However, this process does not excite the molecule. Excitation, i.e. the formation of an electron-hole pair, which means first an electron must populate the LUMO followed by a hole populating the HOMO or vice versa. EL therefore leads at some point to a charged molecule, because an additional electron is either added to or removed from the neutral molecule before the charge is compensated by the opposite charge carrier. This is an inherent difference to PL where an electron is excited from the HOMO to the LUMO. For EL the molecule has to

keep electron and hole in LUMO and HOMO long enough so recombination can occur. This is unlikely, when either charge carrier can easily propagate to the substrate. For this reason decoubling between molecule and substrate is required [40, 66–68]. Decoupling by placing the molecule on a dielectric spacer (Fig. 2.3 b)) allows the density of states of the molecule to shift with respect to the tip and the substrate by the applied bias voltage. The HOMO of the molecule can then be above the Fermi energy of the substrate which facilitates the creation of a hole in the HOMO. Furthermore, the potential barrier between molecule and substrate prevents hybridization and therefore hinders the direct propagation of the excited electron to the substrate. This allows transiently charged states. When the electron-hole pair recombines, a photon may be emitted.

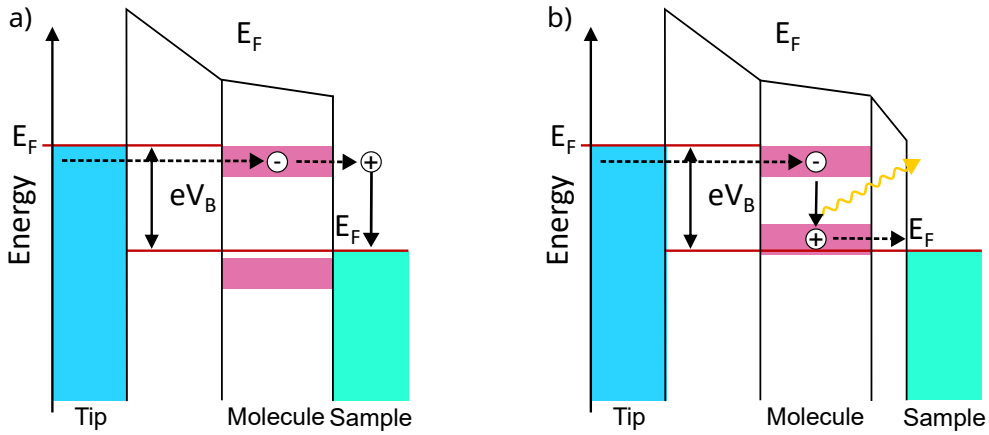

Figure 2.3: Schematic illustration of a) an electron tunneling from the tip through a potential barrier into the LUMO of the molecule adsorbed on the sample. The electron propagates from the LUMO of the molecule into an empty state (hole) in the sample. The Fermi energies E_F of tip and sample are shifted by the potential difference eV_B. The HOMO and LUMO of the molecule are depicted in purple. b) An electron tunneling from the tip through a potential barrier into the LUMO of the molecule that is decoupled from the sample. The HOMO of the molecule can now be shifted to the Fermi energy of the sample, allowing the creation of an electron-hole pair with sufficient lifetime. The electron-hole pair may emit a photon upon recombination. After [59, 69].

2.3 Radiative transitions in a quantum mechanical picture

This section is mostly based on *Electronic Processes in Organic Semiconductors* [70] which offers an in depth description on photophysical processes in organic semiconductors.

The rate k_{if} for a transition between an initial state $\mathbf{\Psi_i}$ and a final state $\mathbf{\Psi_f}$ is given by Fermi's golden rule:

$$k_{if} = \frac{2\pi}{\hbar}\rho(\omega) \mid \langle \mathbf{\Psi_f} \mid \hat{H}' \mid \mathbf{\Psi_i} \rangle \mid^2, \tag{2.6}$$

where $\rho(\omega)$ is the density of the final states that depends on the frequency ω of the involved modes. The transition is expressed by a perturbation $\hat{H}'$ that is added to the unperturbed Hamiltonian $\hat{H}_0$ according to $\hat{H} = \hat{H}_0 + \hat{H}'$. In the case of a transition caused by the absorption of light, the dipole approximation may be used. $\hat{H}'$ is then given by the electric and magnetic dipole operators $\hat{\mathbf{d}}$ and $\hat{\mathbf{m}}$ acting on the electric and magentic fields $\hat{\mathbf{E}}$ and $\hat{\mathbf{B}}$, respectively. The perturbation then is $\hat{H}' = -\hat{\mathbf{d}} \cdot \mathbf{E} - \hat{\mathbf{m}} \cdot \mathbf{B}$. Inserting this in eq. 2.6 gives:

$$k_{if} = \frac{2\pi}{\hbar}\rho(\omega)\Big[\mid \langle \mathbf{\Psi_f} \mid \hat{\mathbf{d}} \mid \mathbf{\Psi_i} \rangle \cdot \mathbf{E} \mid^2 + \mid \langle \mathbf{\Psi_f} \mid \hat{\mathbf{m}} \mid \mathbf{\Psi_i} \rangle \cdot \mathbf{B} \mid^2 + 2 \mid \langle \mathbf{\Psi_f} \mid \hat{\mathbf{d}} \mid \mathbf{\Psi_i} \rangle \cdot \mathbf{E} \mid\mid \langle \mathbf{\Psi_f} \mid \hat{\mathbf{m}} \mid \mathbf{\Psi_i} \rangle \cdot \mathbf{B} \mid \Big]. \tag{2.7}$$

The mixed term vanishes since $\hat{\mathbf{E}} \perp \hat{\mathbf{B}}$ which simplifies this to:

$$k_{if} = \frac{2\pi}{\hbar}\rho(\omega) \left[\mid \langle \mathbf{\Psi_f} \mid \hat{\mathbf{d}} \mid \mathbf{\Psi_i} \rangle \cdot \mathbf{E} \mid^2 + \mid \langle \mathbf{\Psi_f} \mid \hat{\mathbf{m}} \mid \mathbf{\Psi_i} \rangle \cdot \mathbf{B} \mid^2 \right]. \tag{2.8}$$

In the case of a dipole inside a cavity of two metal electrodes, $\rho(\omega)$ contains the enhancement of the local density of states due to the Purcell effect [71]. The radiative transition rate of a dipole inside a cavity can be obtained when describing the photonic density of states with $\rho(\omega)$ and considering the quantized electric field $E_z(\mathbf{M})$ which considers the root mean square of the local zero-point electric field at position $\mathbf{M}$ of the system which arises from the non vanishing zero point energy. The perturbation is then given by the electric dipole moment when neglecting magnetic dipole transitions. This leads to the radiative transition rate k_{rad} [72]:

$$k_{\mathrm{rad}} = \frac{2\pi}{\hbar}\rho(\omega) \mid \langle \mathbf{\Psi_f} \mid \hat{\mathbf{d}} \mid \mathbf{\Psi_i} \rangle \mid^2 E_z(\mathbf{M})^2. \tag{2.9}$$

The total molecular wavefunction has electric ($\mathbf{\Psi_{el}}$), spin ($\mathbf{\Psi_{spin}}$) and vibrational ($\mathbf{\Psi_{vib}}$) contributions. Using the Born-Oppenheimer aproximation and neglecting the magnetic dipole interaction leads to [70]:

$$k_{if} = \frac{2\pi}{\hbar}\rho(\omega) \mid \langle \mathbf{\Psi_{el,f}} \mid e\hat{\mathbf{r}} \mid \mathbf{\Psi_{el,i}} \rangle \mid^2 \mid \langle \mathbf{\Psi_{vib,f}} \mid \mathbf{\Psi_{vib,i}} \rangle \mid^2 \mid \langle \mathbf{\Psi_{spin,f}} \mid \mathbf{\Psi_{spin,i}} \rangle \mid^2, \tag{2.10}$$

with the electric dipole operator $\hat{\mathbf{d}} = e\hat{\mathbf{r}}$, where e is the elementary charge and $\hat{\mathbf{r}}$ the position operator. The overlap of the electronic wavefunctions of initial and final states is responsible for the intensity of the transition. The electric dipole operator has an odd symmetry under spatial inversion. For this reason, the electronic integral $\mid \langle \mathbf{\Psi_{el,f}} \mid e\hat{\mathbf{r}} \mid \mathbf{\Psi_{el,i}} \rangle \mid^2$ requires different parity between $\mathbf{\Psi_{el,i}}$ and $\mathbf{\Psi_{el,f}}$, otherwise the integral will be zero and the transition is considered electric dipole forbidden. The Franck-Condon factor $\langle \mathbf{\Psi_{vib,f}} \mid \mathbf{\Psi_{vib,i}} \rangle \mid^2$ gives the probability of the transition from the vibrational ground state of the electronic ground state to a vibrational excited state of an electronic excited state (see Fig. 2.7). The spin integral $\langle \mathbf{\Psi_{spin,f}} \mid \mathbf{\Psi_{spin,i}} \rangle$ can have a value of 0 or 1 depending on whether $\mathbf{\Psi_i}$ and $\mathbf{\Psi_f}$ have same or opposite spin. When they have the same spin, the transition is spin allowed, otherwise it is forbidden. Radiative emission from spin allowed transitions are called fluorescence, emission from spin forbidden transitions are called phosphoresence. The

observation of the forbidden phosphoresence is enabled by spin-orbit coupling, which means the change in spin S can be compensated by a change in the orbital angular momentum L since only the sum $J = L + S$ has to be conserved.

2.4 Light emission inside the STM cavity

Among other things, this thesis focuses on the luminescence of molecules adsorbed on metal surfaces inside the STM cavity. For this reason, the interaction of the electromagnetic field and the metal will be discussed in this section, outlining the characteristics of plasma oscillations and highlighting the differences in the electric and magnetic field components of dipole radiation in front of metal surfaces.

2.4.1 Plasma oscillations

This section is mostly based on *Principles of Nano-Optics* [73] which provides an in depth description of the interaction of matter and light at the nano scale.

An idealized metal can be described as a lattice of ions and a free electron gas. When the electrons are homogeneously distributed their charge cancels the opposite charge of the ions and the total charge of the metal is neutral. When an electron is displaced, the local equilibrium is broken and the positive charge of the lattice is no longer fully compensated. This creates and electric field between the electron and the vacant position and concomitantly a restoring force that acts upon the electron. This problem can be described by a harmonic oscillator. In this idealized model, damping is not considered and the solution to the differential equation of the harmonic oscillator is given by the volume plasma frequency ω_p:

$$\omega_p = \sqrt{\frac{ne^2}{m\epsilon_0}}. \tag{2.11}$$

n describes the electron density, e the elementary charge, m the effective electron mass and ϵ_0 the vacuum dielectric constant. The quantization of these charge oscillations arising from quantummechanics are called plasmons.

When light, i.e. an electromagnetic wave, hits a metallic surface, it can be reflected or transmitted, when damping which means absorption is neglected. When the free space frequency of the light ω is lower than the plasma frequency ω_p ($\omega < \omega_p$) the free electrons in the metal will move in sync with the electric field of the light, but with a phase shift of 180°. These image charge oscillations compensate the electric field inside the metal, while creating a reflected wave outside the metal. When $\omega > \omega_p$, the electrons cannot follow the excitation due to their inertia and the metal becomes predominantly transparent, e.g. for X-rays. When the electromagnetic field has longitudinal components, for example in a non-uniform field, bulk plasmons can be excited.

Another type of plasmons can be found at the interface between two media when the dielectric function ϵ of one medium is positive, and negative for the other. This is the case for the interface between a dielectric such as vacuum and a metal. Electrons may be excited to coherent oscillations that propagate along the interface as delocalized waves. These oscillations are referred to as surface plasmon polaritons (SPPs). To excite a SPP, the momentum of the excitation light needs to match the momentum of the SPP. The dispersion relation is schematically displayed in Fig. 2.4. The frequency of bulk plasmons ω_{Bulk} is shown in green, the frequency of free photons is shown in red and the frequency of SPPs in blue. The maximum frequency of SPPs $\omega_{\text{SPP}}^{\text{max}}$ for large wavevectors is indicated by the lower dashed horizontal line. The upper dashed horizontal line represents the plasma frequency ω_p. Photons describe free electromagnetic waves in the far field. Their frequency and thus energy is limited by $\omega = ck$. When plasmons are considered, the parallel wavevector $k_{\parallel}$ along the interface is portrayed along the x-axis. This leads to a so called light cone as depicted in gray, since the wave vector perpendicular to the surface can vary. Light propagating in the far field as photons only exists within the light cone.

SPP can be understood when considering Maxwell's equation for the electric field at an interface at $z = 0$ [73]:

$$\mathbf{E_j} = E_0 \begin{pmatrix} 1 \\ 0 \\ -k_x/k_{j,z} \end{pmatrix} e^{ik_{j,z}|z|+k_x x-\omega t}, \tag{2.12}$$

$j = 1, 2$ hereby describe the two half spaces at the interface $z = 0$ defined by the dielectric functions ϵ_1 and ϵ_2 of metal and vacuum, respectively. The wavevectors k_x and $k_{j,z}$ are given by:

$$k_x^2 = \frac{\epsilon_1\epsilon_2}{\epsilon_1+\epsilon_2}\frac{\omega^2}{c^2}, \tag{2.13}$$

$$k_{j,z}^2 = \frac{\epsilon_j^2}{\epsilon_1+\epsilon_2}\frac{\omega^2}{c^2}. \tag{2.14}$$

When absorption is neglected, ϵ_1 and ϵ_2 are real. Furthermore, for a vacuum-metal interface, ϵ_1 is negative and large in comparison to ϵ_2 so the conditions $\epsilon_1\epsilon_2 < 0$ and $\epsilon_1 + \epsilon_2 < 0$ are met. For this reason k_x is real and $k_{j,z}$ is imaginary, the wave is therefore localized on the interface and decays exponentially into both media. The magnetic field is equally confined to the surface and oscillates in phase with the electric field. The thus defined charge carrier oscillations are called SPPs. Their frequency ω_{SPP} is given by:

$$\omega_{\text{SPP}} = \frac{\omega_p}{\sqrt{\epsilon_2+1}}. \tag{2.15}$$

While SPPs can travel along the interface, their propagation is limited to several 10 µm. It is apparent from the dispersion relation that the free space lightwaves and SPPs cannot interact with each other due to the mismatch in momentum. This means free space light cannot excite SPPs and SPPs cannot couple into free space light in the idealized model of a plane interface. In reality, however, the surface roughness, the presence of scattering centers

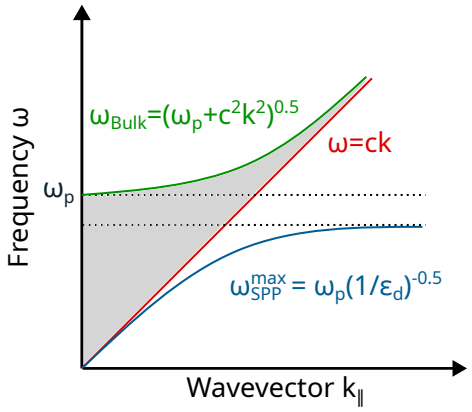

Figure 2.4: Dispersion relation of the frequency of bulk plasmons ω_{Bulk} (green), photons in vacuum ω (red) and SPPs (blue). The light cone describing propagating photons is indicated in gray. The maximum frequency of SPPs is given by $\omega_{\mathrm{SPP}}^{\mathrm{max}}$. After [62, 74].

and, in the context of this work, the STM tip will break the lateral translation invariance [59].

The SPPs of two metals in proximity can couple when their evanescent waves overlap [62, 75]. This interaction of coupled charge carriers on both metals separated by a dielectric spacer is called a gap plasmon. This situation is found in the STM junction where a metallic tip is in proximity to a metallic substrate separated by the vacuum. The resonance condition is fulfilled for integer values of the mode index l ($l = 0, 1, 2...$) [72] when the tip-sample distance d is equal to half of the wavelength of the gap plasmon also called localized surface plasmon (LSP). The resonance frequency ω_l is then given by [72]:

$$\omega_l \approx \omega_p \sqrt{(l + 0.5)\sqrt{\frac{d}{2R}}}. \tag{2.16}$$

R describes the radius of curvature of the tip apex. The exact tip configuration does therefore greatly influence emission from gap plasmons. In the case of STML, LSPs may be excited by inelastic tunneling [76]. When the match in momentum is given, LSPs can radiate into the far field by emitting photons. In the context of STML, the energy of these photons is limited by the bias voltage [62].

2.4.2 Dipole emission in front of metallic and dielectric surfaces

K. H. Drexhage discovered that the exited state lifetime of a light emitting molecule will vary when placed in front of a mirror. Using Eu^{3+} complexes on top of dielectric spacers of varying thicknesses, he observed an oscillatory behavior of the lifetime when varying the distance to the mirror [77]. H. Kuhn describes this dependence as an interference effect between the dipole and its image charge by considering the retardation induced upon reflection [78]. In a classical and idealized picture, this problem can be described by a dipole

inducing an image charge oscillating out of phase and interfering with the dipole [78, 79]. Therefore, the distinction between the electric and magnetic field becomes apparent, since only the electric field experiences a phase shift of 180° upon reflection at frequencies below the plasma frequency. When the oscillating point charge of the dipole is described by a harmonic oscillator, the dampening is given by the energy loss due to radiation, while the image charge can be treated as an additional force acting on the oscillating point charge [80].

When the distance between dipole and mirror surface is decreased, the dipole transfers energy to the metal [80], which opens de-excitation pathways in the case of excited molecules. For molecule-mirror distances larger than atomic distances, but smaller than the emission wavelength, this problem is analogous to a dipole antenna close to the ground whose radiation is partially absorbed and partially reflected [79, 80]. The first theoretical solution to this problem was provided by A. Sommerfeld, who already realized the possibility of surface waves [80, 81]. Similar to the surface waves described by Sommerfeld, an emitting molecule in front of a metal couples to plasmons [80, 82]. This is due to localized electronic energy being converted into charge-density oscillations at the metal surface [74]. While Kuhn's approach is in agreement with Sommerfeld's findings and suitable for large distances, the energy flux method described by R. R. Chance et al. allows to consider the impact of radiative and non-radiative energy transfer separately [80]. This method considers the energy flux through two infinite planes, above and below the dipole, respectively. For large distances, the terms describing the energy transfer to the metal by far field radiation are dominant. The energy flux method described by Chance et al. [80] leads to the same results regarding the radiative decay rates as the interference approach by Drexhage [77, 80], but also describes the non-radiative decay rate due to energy transfer to the metal. For small distances, the non-radiative decay rate $\hat{b}_{\mathrm{nonrad}}$ is proportional to the distance d with $\hat{b}_{\mathrm{nonrad}} \sim \hat{d}^{-3}$. While Förster type energy transfer might be expected to be the main mechanism for the energy being transferred from the molecule to the metal, this was shown to be insufficient [80]. The luminescence decay of a molecule at a distance to a metal surface smaller than the emission wavelength was also considered by H. Morawitz et al. [74]. They found a drastic reduction in the lifetime when approaching the metal surface which leads to a diverging emission linewidth.

The expression for the energy transfer rate γ_{ET} of dipole emission in front of a metal surface at distance d is given by [46, 49, 80, 82, 83]:

$$\gamma_{\mathrm{ET}} = \gamma_{\mathrm{rad0}} \cdot \frac{3}{16k^3} \mathrm{Im}\left(\frac{\varepsilon_{\mathrm{metal}} - \varepsilon_{\mathrm{mol}}}{\varepsilon_{\mathrm{metal}} + \varepsilon_{\mathrm{mol}}}\right) \cdot \frac{p_x^2 + p_y^2 + 2p_z^2}{|\mathbf{p}|^2} \cdot \frac{1}{d^3}. \tag{2.17}$$

γ_{rad0} describes the radiative rate in free space, k the wavevector, $\varepsilon_{\mathrm{metal}}$ the permittivity of the metal surface, $\varepsilon_{\mathrm{mol}}$ the permittivity of the environment of the molecular dipole, $p_{x,y,z}$ the components of the transition dipole moment and d the distance between the dipole emitter and the metal surface. For the main Eu^{3+} transition $^5D_0 \rightarrow {}^7F_2$, $\lambda = 2\pi/k$ can be approximated to 615 nm. The permittivities of organic complexes and a silver substrate are given by $\varepsilon_{\mathrm{mol}} = 2.56$ [34] and $\varepsilon_{\mathrm{metal}} = -16 + 0.6\,\mathrm{i}$ [84]. An an-isotropic medium, i.e. a random orientation of dipole moments leads to $\frac{p_x^2+p_y^2+2p_z^2}{|\mathbf{p}|^2} = 4/3$. Using these values, γ_{ET} is

given by:

$$\gamma_{\mathrm{ET}} \approx \gamma_{\mathrm{rad0}} \cdot \frac{4030}{\{d\}^3}. \tag{2.18}$$

$\{d\}$ denotes the value of the distance d ($[d]$=nm) without dimension. The decay rate as expressed by $\gamma_{\mathrm{obs}} = \gamma_{\mathrm{rad0}} + \gamma_{\mathrm{ET}} + \gamma_{\mathrm{nonrad}}$ then is:

$$\gamma_{\mathrm{obs}} = \gamma_{\mathrm{rad0}} \cdot \left(1 + \frac{4030}{\{d\}^3}\right) + \gamma_{\mathrm{nonrad}}. \tag{2.19}$$

It should be noted that early publications report that the de-excitation of molecules via so called lossy surface waves approaches 100 % with vanishing distance to the metal surface [82]. Significant de-excitation via photon emission and the excitation of SPPs is only expected for distances larger than 10 nm. A more recent report states that the identical cubic distance dependence for the energy transfer rate and the decay rate of gap plasmons indicates that these processes are of the same nature for vanishing distances [49].

L. Novotny and B. Hecht provide a quantitative description on the lifetime of a dipole in front of metallic and dielectric surfaces in a modern context [73]. For small distances, the lifetime of a vertical electric dipole in front of a dielectric surface is always larger than for a vertical electric dipole in front of a metallic surface. For a horizontally oriented dipole in front of a metal, the lifetime shows an oscillatory behavior. These oscillations are less pronounced in front of a dielectric surface. At small distances, the lifetime of the horizontal dipole approximates zero in front of a metal, while the lifetime of the dipole in front of the dielectric is close to the lifetime of a dipole at infinite distance. The graphs of the lifetime in front of a metal and in front of a dielectric intersect at 8.3 nm for an aluminium surface. The regime of distances around 20 nm is of most interest in this thesis, since thin films of approximately this height were investigated.
The difference in emission of electric and magnetic dipoles in front of a metallic surface is illustrated in Fig. 2.5. A dipole antenna radiates mostly perpendicular to its axis. For an optical fiber positioned perpendicular to a metallic surface, the highest light collection would therefore be expected for a dipole oriented parallel to the surface, i.e. perpendicular to the optical fiber. However, in the context of Eu^{3+} complexes adsorbed on the metal surface, both, the electric and magnetic dipole transitions have to be considered.

In an idealized picture, an electric dipole above a metallic surface induces an opposing image charge in the metal. When the electric dipole moment $\mathbf{d}$ is oriented parallel to the surface, the electric dipole moment of the image charge $\mathbf{d_I}$ points in the opposite direction (Fig. 2.5 a). For an electric dipole with $\mathbf{d}$ perpendicular to the surface, $\mathbf{d_I}$ points in the same direction (Fig. 2.5 b). In both cases, there is an attractive force between dipole and image charge, but when $\mathbf{d}$ and $\mathbf{d_I}$ point in opposite directions, they interfere destructively reducing the transition probability [85]. In the context of STML this reduces the light collected from ED transitions with the optical fiber. When $\mathbf{d}$ and $\mathbf{d_I}$ point in the same direction, they interfere constructively enhancing the transition probability and therefore light collection [85]. The opposite is true for a magnetic dipole. A magnetic dipole in front of a metallic

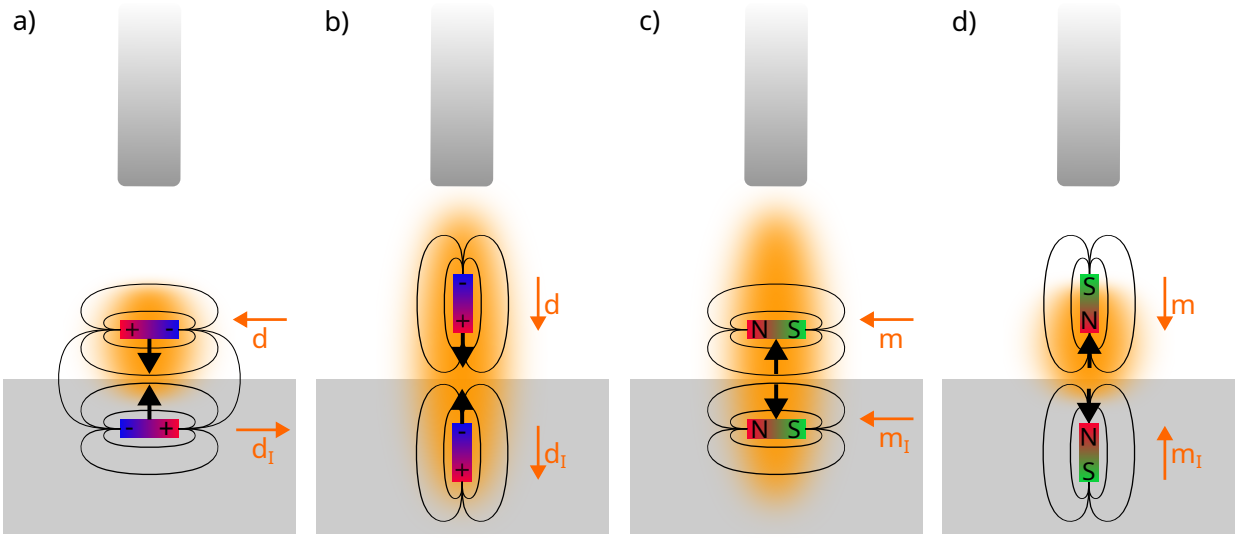

Figure 2.5: ED and MD emission in front of a metallic surface with induced image charge for parallel and perpendicular oriented electric (**d**) and magnetic (**m**) dipole moments. The optical fiber is perpendicular to the surface. The force between the dipole and its image charge is indicated by the black arrows. For an electric dipole, the force between itself and its image charge is attractive (a,b). For a magnetic dipole, the force is repulsive (c,d). The orientation of the electric and magentic dipole moment is indicated by the orange arrows. **d** interferes destructively (a) (constructively (b)) with the electric dipole moment of its image $\mathbf{d_I}$ when it is oriented parallel (perpendicular) to the surface. **m** interferes constructively (c) (destructively (d)) with the magnetic dipole moment of its image $\mathbf{m_I}$ when it is oriented parallel (perpendicular) to the surface.

surface will lead to a charge carrier distribution that induces a repulsive force to its source. For a magnetic dipole moment **m** parallel to the surface, the dipole moment of its image $\mathbf{m_I}$ points in the same direction resulting in constructive interference and therefore an increased transition probability [85] and enhanced light collection from the MD transition (Fig. 2.5 c)). When the magnetic dipole moment is oriented perpendicular to the surface (Fig. 2.5 d)) it interferes destructively with its image reducing the transition probability [85] and light collection. When light is collected mostly perpendicular to the metal surface, emission from MD transitions is preferably detected.

Another way of looking at this is by considering the boundary conditions of the electromagnetic field at the metal interface. For a mode of the electromagnetic field with wavevector normal to the surface, the electric field has a node at the interface, while the magnetic field has a maximum. This is synonymous with the electric field experiencing a phaseshift of 180° upon reflection at the metal surface. This results in a vanishing transition probability for an ED transition and a maximum transition probability for a MD transition according to Fermi's golden rule.

2.5 Transition rates and observed lifetime

When several molecules are excited and the luminescence signal is measured, its intensity $I(t)$ will decline exponentially over time. The exponential decay can be explained as follows: For simplicity, we consider only one kind of molecule and follow the decay of one particular excited state. This state then has the same probability to decay in each infinitesimal time interval. Analogous to radioactive decay, this probability does not depend on the history of excitation and is independent on the time spent in the excited state. In reality, there are multiple pathways for de-excitation. An excited state can either relax radiatively, or non-radiatively. A radiative decay is defined as the emission of electromagnetic radiation. All processes that lead to the de-excitation of the excited state without emitting electromagnetic radiation are called non-radiative. A radiative transition is characterized by the transition rate k_{rad}, a non-radiative transition by the non-radiative transition rate k_{nonrad}. Since a single state cannot simultaneously decay radiatively and non-radiatively, these processes are non-independent. The total transition rate then is $k_{\mathrm{tot}} = k_{\mathrm{rad}} + k_{\mathrm{nonrad}}$. There are several pathways for non-radiative transitions that will be discussed later. Each pathway has a specific transition rate. k_{nonrad} is therefore the sum of all non-radiative transition rates. The more pathways for non-radiative transitions exist, the higher k_{nonrad} will be, since each transition contributes its rate. An increasing amount of de-excitation pathways therefore leads to a faster exponential decay. The rate of a transition depends on the probability of the transition between initial and final state according to Fermi's golden rule and is an inherent property of the transition. k_{tot} is an inherent property of the excited state and not of a specific transition, since it contains contributions of all transitions starting at this state. k_{tot} can be derived directly from experimental data when the PL intensity after excitation is tracked over time. For every measurement time interval, each molecule has the probability of decaying by a radiative or non-radiative transition after being excited by a light pulse. The probability of detecting a photon emitted from the excited state is not only determined by k_{rad} but by k_{tot}, since the population of excited molecules that could potentially emit a photon decreases, with k_{tot}. The PL intensity declines according to:

$$I(t) = I_0 e^{-t \cdot k_{\mathrm{tot}}}, \tag{2.20}$$

where I_0 is the maximal intensity. It is therefore sufficient to track a single decay process of the excited state to derive its k_{tot}. In experiment, this can be done by tracking the emission caused by a radiative decay of the excited state into the far field at a specific wavelength that does not overlap with emission from other excited states. When the emission spectrum from one excited state overlaps with emission from other excited states, the decays of these two populations lead to a sum of exponential functions when the decaying PL intensity is tracked at a wavelength within the overlap. The intensity is then given by:

$$I(t) = \sum_i I_{0,i} e^{-t \cdot k_{\mathrm{tot},i}}. \tag{2.21}$$

This can be the case for emission with spectral overlap from different electronic states but also for molecules in the same electronic state but different surroundings. In the context of this thesis for example for thin films of Eu^{3+} complexes on a substrate, some molecules

are adsorbed on the substrate, some are surrounded by other molecules and some are at the interface to the vacuum. This already creates three different environments that interact with the excited molecules, thus providing three different kinds of molecules with different transition rates.

The observed lifetime can be derived from the total transition rate, according to the definition $\tau_{\text{obs}} = 1/k_{\text{tot}}$. It describes the time after which the intensity of the PL signal has dropped to $1/e$ of its initial value. Measuring τ_{obs} will be discussed in section 3.1.3. The radiative lifetime $\tau_{\text{rad}} = 1/k_{\text{rad}}$ cannot directly be determined from experiment, but derived from Judd-Ofelt (JO) theory in the case of emission from Eu^{3+} as will be shown in section 2.7. In the case of lanthanides, τ_{obs} is exceptionally high due to the shielding of the 4f shell.

Molecules cannot be considered as single isolated entities. In this thesis they were investigated in a crystalline powder as obtained after synthesis, dissolved in an alcoholic solution, and as films on dielectric and metallic substrates. Each of these samples provide different environments and decay channels that may reduce luminescence and are therefore critical to improve the electron to light conversion. For molecules adsorbed on a metal surface, decay processes include the excitation of SPPs [47, 48], excitation of image charge oscillations [46], the creation of electron-hole pairs in the metal [45] and electron transport from the molecule to the metal [40]. SPPs can emit into the farfield, when the surface of the metal is appropriately structured [47]. Otherwise their energy will be lost to vibrations within the metal. In the case of a molecule in the STM cavity, there are additional de-excitations given by the excitation of LSPs [49]. Molecules can be placed on dielectric films ontop of the metal substrate to reduce charge transfer from the excited molecule to the metal substrate and increase luminescence [40, 66–68]. In contrast to depositing the molecules on a dielectric substrate, this technique allows to perform STM measurements. The transition rate of a light emitting molecule furthermore depends on its distance to the metal center as was shown in section 2.4.2. This is also true for dielectric surfaces but to a smaller extent. The distance dependence of the transition rate becomes important when investigating films of Eu^{3+} complexes as will be discussed in section 3.6.6. Depositing molecules on a dielectric substrate eliminates decay by charge transfer, plasmonic excitation, image charge oscillations, and electron-hole pair creation. For a dielectric surrounding, the impact of the refractive index becomes apparent: the photonic local density of states increases with increasing refractive index which leads to an enhancement of the radiative transition rate [50–52]. Furthermore, the refractive index of the surrounding medium is known to impact Förster type energy transfer [53]. It should be pointed out that even in isolated molecules non-radiative de-excitation channels exist. A famous example is the quenching of luminescence due to relaxation caused by OH-vibrations [42–44]. The high frequency of OH-vibrations (~ 3500 cm^{-1} [86]) efficiently quenches luminescense as can be seen when considering the energy gap law. This states that the non-radiative transition rate for vibronic relaxations k_{vib} scales according to $k_{\text{vib}} \propto \exp(-\gamma \Delta E/(\hbar\omega_M))$ [70]. ΔE is the energy difference between initial and final state, γ a term accounting for molecular parameters, and ω_M the frequency of the mode with highest energy. The high frequency of OH-vibrations leads to a large k_{vib}. For this reason hydrogen is often replaced by the heavier deuterium

to reduce quenching [86, 87]. In solution, vibrational relaxation can be mediated by higher harmonics of hydrogen bond vibrations [41–43].

2.6 Emission from 4f transitions in Eu^{3+}

The electronic configuration of Eu is $[Xe]4f^76s^2$. However in its trivalent form (Eu^{3+}), the configuration is $[Xe]4f^6$. Although the 4f shell is the highest in energy, it does not extent farthest from the atomic nucleus. Instead, it is shielded by the 5s and 5p orbitals. The six valence electrons of Eu^{3+} are distributed in the seven f orbitals of the f shell according to Hund's rule [63]. The term symbol of the ground state of Eu^{3+} is ^7F_J. The term symbol describes the spin multiplicity S, the orbital momentum L and the total angular momentum J of a state according to $^{2S+1}L_J$ where J ranges from $\mid L-S \mid$ to $\mid L+S \mid$ in integer steps. Each of the seven f orbitals within the f shell can hold up to two electrons with opposite spin according to Pauli's principle [63]. Hence, there are $\binom{14}{6} = 3003$ different ways to distribute the six valence electrons within the f shell. Electron repulsion places quantum mechanical restrictions on the distribution of electrons which splits the 4f shell into 119 different terms. This means there are 118 excitations possible by redistributing the electrons within the 4f shell. Laporte selection rules require a change in parity when transitioning from one orbital to another in a centrosymmetric environment that is given for isolated atoms [34]. This is a direct consequence of the electronic integral in Fermi's golden rule requiring a change in parity to not vanish. Transitions within the 4f shell of an isolated atom are inherently Laporte forbidden. However, when Eu^{3+} is embedded in a complex consisting of Eu^{3+} as the metal center, surrounded by ligands, the selection rules are relaxed by the ligand field and vibronic coupling. These transitions are then called induced electric dipole transitions. These transitions are comparatively long lived (see section 3.1) due to their forbidden nature [34]. The selection rules for induced electric dipole transitions according to Judd [34, 88, 89] are listed in Table 2.1. The resulting long lifetimes in connection with the shielding effect makes Eu^{3+} complexes highly interesting for applications in optoelectronics [90–92], sensors [93–96] and spintronic devices [97, 98].

ED transition	**Induced ED transition**	**MD transition**
$\Delta S = 0$	$\mid \Delta S \mid = 0$	$\Delta S = 0$
$\mid \Delta L \mid \leq 1$	$\mid \Delta L \mid \leq 6$	$\Delta L = 0$
$L = 0 \nleftrightarrow L' = 0$		
$\mid \Delta J \mid \leq 1$	$\mid \Delta J \mid \leq 6$	$\Delta J = 0, \pm 1$
$J = 0 \nleftrightarrow J' = 0$	$\mid \Delta J \mid = 2, 4, 6$ if $J = 0$ or $J' = 0$	$J = 0 \nleftrightarrow J' = 0$
Oscillator strength:		
$\sim 0.01 - 1$	$\sim 10^{-4}$ of ED	$\sim 10^{-6}$ of ED

Table 2.1: Selection rules for electric dipole (ED) transitions, induced ED transitions and magnetic dipole (MD) transitions within the 4f shell with approximate magnitude of oscillator strength after [34, 89]. "$\nleftrightarrow$" indicates a forbidden transition.

The PL spectrum of Eu^{3+} complexes is dominated by the fine structure resulting from radiative transitions from the first excited state $^5D_0$ to the ground states ^7F_J with $J = 0 - 6$ (Fig. 2.6). The degeneracy of the total angular momentum J is lifted by spin-orbit coupling, leading to seven main emission bands in the visible range. The shielding of the 4f orbital leads to the characteristic emission spectrum that only changes slightly with different environments, e.g. different ligands. The shielding effect also reduces broadening of the emission bands by interaction with the environment resulting in sharp emission bands. Each emission band of the fine structure consists of several ligand field sub levels arising from the Stark effect lifting the $2J + 1$ degeneracy. The Stark effect describes the splitting of emission lines due to an electric field. The distribution of the electric field at the metal center of the complex depends on the type and orientation of the ligands. Therefore, an analysis of the ligand field sublevels allows to draw conclusions about the symmetry of the environment of the light emitting metal center. In general, the number of observed ligand field levels increases with decreasing symmetry [34, 89]. When emission results from transitions within several complexes, the interaction between the complexes has to be regarded, as well. A single crystal of complexes offers a well defined environment, resulting in sharp crystal field levels.

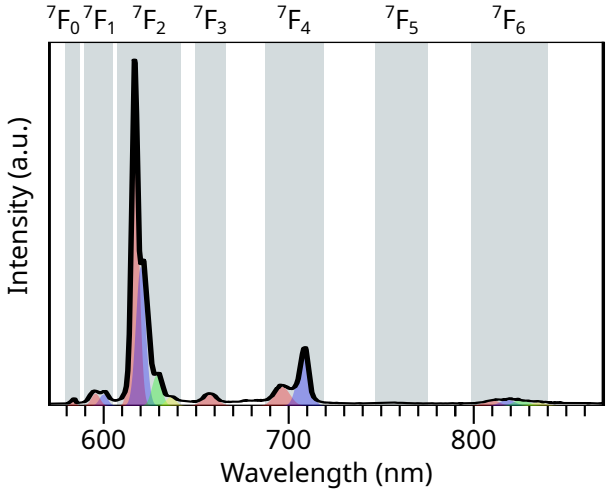

Figure 2.6: Emission spectrum of Eu^{3+} with main emission bands from $^5D_0 \rightarrow {}^7F_{J=0-6}$ transitions on gray background and ligand field sublevels exemplary highlighted in color. Emissions from $^5D_0 \rightarrow {}^7F_5$ and $^5D_0 \rightarrow {}^7F_6$ are very weak.

An overview of the main transitions in the emission spectrum of Eu^{3+} is given in table 2.2. The $^5D_0 \rightarrow {}^7F_0$ emission band lacks degeneracy because of $J = 0$. This leads to one sharp emission line at 570-585 nm from an induced ED transition. Due to its sharpness, it is often used as an indicator for the local environment and symmetry of the light emitting site. The $^5D_0 \rightarrow {}^7F_0$ transition is not only Laporte forbidden, but it is also not allowed according to the selection rules for induced ED transitions, because J and $J' = 0$. It is still a topic of discussion why its emission can be observed nonetheless. Mostly, the relaxation of selection

rules is attributed to J mixing caused by the ligand field [34–38], or to a distortion of the environment due to charge transfer [39]. The $^5D_0 \rightarrow {}^7F_1$ transition is of magnetic dipole character. While MD transitions are typically about two orders of magnitude less intense than induced ED transitions, the $^5D_0 \rightarrow {}^7F_1$ emission band can usually be well observed at 585-600 nm. This transition is unique within the main emission spectrum of Eu^{3+}, since it is the only MD transition. This makes it less sensitive to the environment, which allows to normalize the spectrum and compare different spectra to one another. Furthermore, when the light emitting molecule is in proximity to metal surfaces or islands, the emissions from induced electric dipole transitions can be quenched in comparison to the MD transition, or vice versa (see section 2.4.2). The red color of the Eu^{3+} emission spectrum arises from the most intense emission band from the $^5D_0 \rightarrow {}^7F_2$ induced ED transition at 610-630 nm. This transition in considered hypersensitive to the environment surrounding the light emitting site [34, 89]. The $^5D_0 \rightarrow {}^7F_3$ and $^5D_0 \rightarrow {}^7F_5$ transitions whose emissions can be observed at 640-660 nm and 740-770 nm, respectively, are forbidden according to the selection rules for induced ED transitions, with the $^5D_0 \rightarrow {}^7F_5$ sometimes being hardly visible. Emission from the $^5D_0 \rightarrow {}^7F_4$ transition can be observed at 680-710 nm. This transition depends on the environment of the light emitting molecule, but it is not hypersensitive to it. Emission from the $^5D_0 \rightarrow {}^7F_6$ transition at 810-840 nm is very weak.

Transition	**Dipole character**	**Wavelength range (nm)**	**Relative intensity**	**Remarks**
$^5D_0 \rightarrow {}^7F_0$	ED	570-585	vw to s	Forbidden transition; only observed in C_n, C_{nv} and C_s symmetry
$^5D_0 \rightarrow {}^7F_1$	MD	585-600	s	Intensity largely independent of environment
$^5D_0 \rightarrow {}^7F_2$	ED	610-630	s to vs	Hypersensitive transition; intensity very strongly dependent on environment; most prominent transition in all Eu^{3+} spectra in this work
$^5D_0 \rightarrow {}^7F_3$	ED	640-660	vw to w	Forbidden transition
$^5D_0 \rightarrow {}^7F_4$	ED	680-710	m to s	Intensity dependent on environment, but no hypersensitivity
$^5D_0 \rightarrow {}^7F_5$	ED	740-770	vw	Forbidden transition
$^5D_0 \rightarrow {}^7F_6$	ED	810-840	vw to m	Rarely measured and observed in literature

Table 2.2: Main transitions of an Eu^{3+} emission spectrum. vw: very weak, w: weak, m: medium, s: strong, vs: very strong. $^5D_0 \rightarrow {}^7F_3$ and $^5D_0 \rightarrow {}^7F_5$ are forbidden according to selection rules for induced dipole transitions. After [34].

While the typical Eu^{3+} spectrum arises from the radiative transitions mainly from the $^5D_0$ excited levels to the $^7F_{0-6}$ ground states, emission from and $^5D_1$ to ^7F_J is sometimes also observed and can overlap with emission from $^5D_0$. An overview of the emission from $^5D_0$,

$^5D_1$ and $^5D_2$ is given in table 2.3. The excited levels with higher energy, e.g. $^5D_1$ can relax non-radiatively into lower levels as will be shown in section 3.6.5.

	$^7\mathbf{F_0}$	$^7\mathbf{F_1}$	$^7\mathbf{F_2}$	$^7\mathbf{F_3}$	$^7\mathbf{F_4}$	$^7\mathbf{F_5}$	$^7\mathbf{F_6}$
$^5\mathbf{D_0}$	580	594	618	652	696	751	817
$^5\mathbf{D_1}$	527	538	558	586	621	664	715
$^5\mathbf{D_2}$	466	475	490	512	538	570	608

Table 2.3: Approximate wavelengths in nm of emission from transitions between $^5D_{0-2}$ to $^7F_{0-6}$. After [34].

2.7 Determining Judd-Ofelt parameters from Eu^{3+} emission

When exciting light emitting molecules and tracking the exponential decay of the PL signal, only the observed lifetime τ_{obs} is directly accessible. τ_{obs}^{-1} is determined by the sum off all possible de-excitation mechanisms (see section 2.3). However, for optimizing the quantum yield, the radiative lifetime τ_{rad} is of interest. For the case of emission from Eu^{3+}, τ_{rad} can be estimated from the PL spectrum by using the JO parameterization. This section is mostly based on [34]. The main emission bands of the Eu^{3+} spectrum are characterized by their J quantum number. The Einstein coefficient $A(\mathbf{\Psi_J}, \mathbf{\Psi'^{J'}})$ describes the rate for spontaneous emission from $\mathbf{\Psi'^{J'}} \rightarrow \mathbf{\Psi_J}$. It is given by:

$$A(\mathbf{\Psi_J}, \mathbf{\Psi'^{J'}}) = \frac{64\pi^4\tilde{\nu}^3}{3h(2J+1)}\left[\frac{n(n^2+2)^2}{9}D_{\text{ED}} + n^3 D_{\text{MD}}\right]. \tag{2.22}$$

$\tilde{\nu} = 1/\lambda$ is the average wavenumber of the $J \rightarrow J'$ transition, h the Planck constant, and D_{ED} and D_{MD} the electric and magnetic dipole strengths, respectively. The factor $2J+1$ accounts for the J degeneracy of the initial state. For the initial state of Eu^{3+} ($^5D_0$), $2J+1 = 1$. Since Eu^{3+} is usually incorporated in a medium or adsorbed on a surface, the refractive index n of this medium has to be considered. The Eu^{3+} ion is not only influenced by the electric field of the excitation light, but also by the electric field of the dipoles in the medium. The electric field in the medium is expressed by the Lorentz local field correction. This leads to the factor $\sqrt{n^2(n^2+2)^2/9}$ when also considering the speed of light in the medium. The average wavenumber of the transition $\tilde{\nu}_\lambda$ can be derived from the PL spectrum by weighing the wavenumber $\tilde{\nu}$ with the intensity at that wavenumber $I(\tilde{\nu})$ for the particular emission band from $\Psi'^{J'} \rightarrow \Psi_J$, therefore calculating the center of the band according to:

$$\tilde{\nu}_\lambda = \frac{\int \tilde{\nu}\, I(\tilde{\nu})\, d\tilde{\nu}}{\int I(\tilde{\nu})\, d\tilde{\nu}}. \tag{2.23}$$

$\lambda = 2, 4, 6$ corresponds to emission from the ${}^5D_0 \rightarrow {}^7F_{2,4,6}$ transitions. The magnetic dipole strength D_{MD} is zero for all transitions except for the magnetic dipole allowed ${}^5D_0 \rightarrow {}^7F_1$ transition. The value for $D_{\mathrm{MD}} = 9.6 \cdot 10^{-6}$ Debye^2 can be calculated exactly [34, 99, 100]. The electric dipole strength D_{ED} can be derived from the JO parameters Ω_λ. It is given by:

$$D_{\mathrm{ED}} = e^2 \sum_{\lambda=2,4,6} \Omega_\lambda \left\langle \mathbf{\Psi_J} \middle\| U^{(\lambda)} \middle\| \mathbf{\Psi^{J'}} \right\rangle^2. \tag{2.24}$$

Values for the squared reduced matrix elements $\left\langle \mathbf{\Psi_J} \middle\| U^{(\lambda)} \middle\| \mathbf{\Psi^{J'}} \right\rangle^2$ can be taken from literature [34, 99, 100] and are summarized in table 2.4.

	$\left\langle \mathbf{\Psi_J} \middle\| U^{(2)} \middle\| \mathbf{\Psi^{J'}} \right\rangle^2$	$\left\langle \mathbf{\Psi_J} \middle\| U^{(4)} \middle\| \mathbf{\Psi^{J'}} \right\rangle^2$	$\left\langle \mathbf{\Psi_J} \middle\| U^{(6)} \middle\| \mathbf{\Psi^{J'}} \right\rangle^2$
$\mathbf{{}^5D_0 \rightarrow {}^7F_2}$	0.0032	0	0
$\mathbf{{}^5D_0 \rightarrow {}^7F_4}$	0	0.0023	0
$\mathbf{{}^5D_0 \rightarrow {}^7F_6}$	0	0	0.0002

Table 2.4: Squared reduced matrix elements for induced electric dipole transition used for the calculation of the electric dipole strength and JO parameters. After [34, 99, 100].

For determining the JO parameters Ω_λ, only the average wavenumber of the ${}^5D_0 \rightarrow {}^7F_1$ transition $\tilde{\nu}_1$ and the average wavenumbers $\tilde{\nu}_\lambda$ for emission bands from ${}^5D_0 \rightarrow {}^7F_{J=2,4,6}$ need to be calculated from the experimental data. Ω_λ is then given by:

$$\Omega_\lambda = \frac{D_{\mathrm{MD}}\, \tilde{\nu}_1^3}{e^2\, \tilde{\nu}_\lambda^3 \left\langle \mathbf{\Psi_J} \middle\| U^{(\lambda)} \middle\| \mathbf{\Psi^{J'}} \right\rangle^2} \frac{9n^3}{n\left(n^2+2\right)^2} \frac{\int I_\lambda(\tilde{\nu})\, d\tilde{\nu}}{\int I_1(\tilde{\nu})\, d\tilde{\nu}}. \tag{2.25}$$

$\Omega_{\lambda=2,4,6}$ corresponds to the induced electric dipole transitions ${}^5D_0 \rightarrow {}^7F_{J=2,4,6}$.

For Eu^{3+}, τ_{rad} can easily be derived from the emission spectrum. The spectrum needs to be corrected for detection efficiency, so the ratios of the individual emission lines are accurate. The rate for radiative emission A_{rad} is then given by:

$$A_{\mathrm{rad}} = \frac{1}{\tau_{\mathrm{rad}}} = A_{\mathrm{MD},0}\, n^3 \left(\frac{I_{\mathrm{tot}}}{I_{\mathrm{MD}}} \right). \tag{2.26}$$

I_{tot} is the integrated intensity of all emission lines, I_{MD} the integrated intensity of the MD allowed transition ${}^5D_0 \rightarrow {}^7F_1$. n is the refractive index of the medium surrounding the Eu^{3+} ion and $A_{\mathrm{MD},0}$ the spontaneous emission probability of the ${}^5D_0 \rightarrow {}^7F_1$ transition in vacuum ($A_{\mathrm{MD},0} = 14.65\ \mathrm{s}^{-1}$ [34]). The rate for non-radiative transition A_{nonrad} can be calculated when the observed lifetime τ_{obs} is known from PL decay experiments by:

$$A_{\mathrm{nonrad}} = A_{\mathrm{tot}} - A_{\mathrm{rad}} = \frac{1}{\tau_{\mathrm{nonrad}}} = \frac{1}{\tau_{\mathrm{obs}}} - \frac{1}{\tau_{\mathrm{rad}}}. \tag{2.27}$$

$A_{tot} = \tau_{obs}^{-1}$ describes the total transition rate.

The quantum yield Φ is defined by the ratio of emitted photons to absorbed photons. The intrinsic quantum yield Φ_{Ln}^{Ln} is the quantum yield, when the Eu^{3+} ion is excited directly. It can be calculated by:

$$\Phi_{Ln}^{Ln} = \frac{\tau_{obs}}{\tau_{rad}}. \tag{2.28}$$

2.8 Excitation via the ligand antenna effect

The shielding of the 4f shell by the 5s and 5p shells decreases the probability for exciting the Eu^{3+} ion. The excitation efficiency can be increased by utilizing the ligand antenna effect. For this reason, the ligands attaching to the Eu^{3+} ion must not only have suitable chemical properties for oxidizing Eu to Eu^{3+}, but also facilitate excitation of the Eu^{3+} core by having a broad absorbance in the UV-vis region and efficient charge transfer to the metal center. The ligand antenna effect describes the excitation of the light emitting metal ion via non-radiative intramolecular energy transfer [101–104]. It is well documented in betadiketonates such as 1-(2-Thenoyl)-3,3,3-trifluoroacetone (tta) [92, 105–107] and 1-Phenyl-3,3,3-trifluoro-2,4-pentanedione (btfa) [91, 108–110]. Depending on the requirements to the complex, other ligands such as 2,2'-bipyridine (bpy) [91, 92, 105–110] or H_2O [42, 95, 111, 112] might be used. The OH-vibrations in H_2O are known to quench luminescence by providing a pathway for non-radiative deactivation [42–44] which can be used for determining the impact of ligands on lifetimes and PL [52]. The onset of absorbance in bpy is at 380 - 325 nm, tta and btfa start absorbing at around 400 nm [107–109]. Recently, Eu^{3+} was incorporated into 2,2',2''-tris(salicylideneimino)triethylamine) (trensal) which also starts to absorb at around 400 nm [113]. An overview of the ligands and complexes is given in section 3.2.4, Fig. 3.6 and 3.7.

The excitation via the ligand antenna effect and the emission from the Eu^{3+} excited states of an Eu^{3+} complex are depicted in Fig. 2.7. The ground singlet state of the ligand S_0 and the excited singlet and triplet states S_1 and T_1 are depicted by the potential wells. These potentials wells describe the vibronic excitation of the molecule. The horizontal shift between the potential wells corresponds to the increased equilibrium distance upon excitation. The excitation is displayed by the blue solid arrow stretching from the vibronic ground state of S_0 to a higher vibronic state of S_1 according to the Franck-Condon principle [70]. The excited vibrational state relaxes via the emission of phonons to the vibrational ground state of S_1 [70]. This process tipically takes about a picosecond [70]. From the vibrational ground state of S_1, the triplet state T_1 can be populated via inter system crossing (ISC) which is followed by vibrational relaxation. Ligand emission from S_1 and T_1 to S_0 can occur. The excited states of the Eu^{3+} ion can be populated from S_1 or T_1. Energy might be transferred back from the Eu^{3+} ion to S_1 or T_1. Non-radiative transitions can occur from S_1, T_1 and from the excited states of Eu^{3+}. Although populating the excited levels of Eu^{3+} from the triplet state T_1 requires a spin forbidden ISC from S_1 to T_1, this process is favored by Eu^{3+}

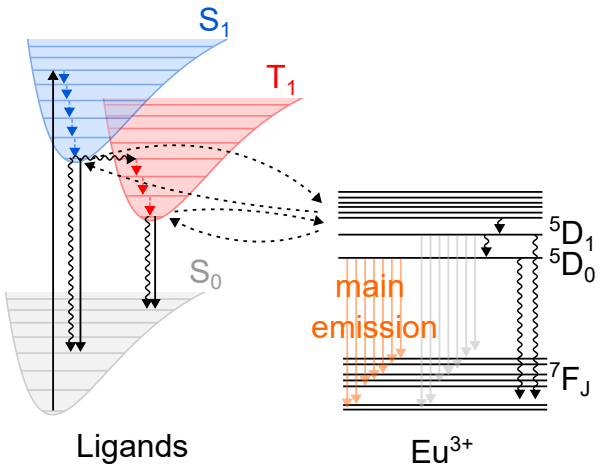

Figure 2.7: Excitation and transition scheme of Europium complexes utilizing the ligand antenna effect after [101]. The vibrational ground state of S_0 is excited to a higher vibrational state of S_1 (solid black arrow). The higher vibrational state relaxes by emitting phonons into the vibrational ground state of S_1 (blue arrows). From there, radiative or non-radiative transitions to S_0 (vertical curvy and solid arrow), or ISC to T_1 can occur (horizontal curvy arrow). After vibrational relaxation, T_1 can decay radiatively, or non-radiatively to S_0 (vertical curvy and solid arrows) or transfer its energy to the excited levels of Eu^{3+} (dashed arrows). The excited levels of Eu^{3+} can decay by emitting a photon to ${}^7F_J$ or by non-radiative processes (vertical curvy arrows). Higher excited levels such as ${}^5D_2$ or ${}^5D_1$ might decay to ${}^7F_J$ directly or by relaxing to lower excited levels first.

complexes due to strong spin orbit coupling [101, 114].

In order to optimize light emission from the Eu^{3+} complex, the possibility for non-radiative decay to the ground states of either ligands or Eu^{3+} needs to be minimized. Also radiative decay from S_1 and T_1 will reduce emission from the Eu^{3+} ion. Furthermore, an efficient energy transfer from T_1 to the excited states of Eu^{3+} has to be ensured. Energy transfer from a donor to an acceptor moiety is usually regarded as Förster or Dexter type. Förster type energy transfer happens via coulombic dipole-dipole interaction between donor and acceptor [70]. Transitions involving triplet states are not possible since Förster transfer conserves the spin of donor and acceptor individually. Due to the coulombic interaction, it relies on strong dipole transition moments that are not given for 4f materials. Energy transfer from the antenna ligands to the Eu^{3+} metal center is therefore mostly considered to take place via Dexter transfer [103], although the presence of additional transfer pathways has been reported [115]. Dexter type energy transfer relies on the exchange of electrons between donor and acceptor. For this reason, it requires sufficient overlap of the wavefunctions and is therefore short range.

3 Photophysical properties of Eu^{3+} complexes

This chapter focuses on the photophysical properties of Eu^{3+} complexes. The experimental set-up used for sample preparation and the set-up for characterization of the optical properties will be described. Both were established as part of this thesis. The experimental findings discuss STM topography data of betadiketonate and trensal based complexes adsorbed on Ag(111) and Au(111) substrates, highlighting the impact of the sample preparation method. Furthermore, the performed EL experiments will briefly be shown. The most important results focus on the dynamics of the 4f transitions within Eu^{3+} complexes, including a qualitative comparison of the PL spectra both in bulk and in thin films, as well as radiative and non-radiative transition rates derived from JO analysis. The decay dynamics are quantitatively treated by TCSPC measurements which enable to access the filling effect of the first electrically excited state of Eu^{3+}, proving that charge is transferred from the ligands to higher excited states first. Finally, evaluating the light-matter interaction and light emission from complexes in proximity to metal surfaces allows determining the main quenching mechanism for luminescence of complexes on metal surfaces.

3.1 Experimental set-up

The experimental set-up used for investigating Eu^{3+} complexes consists of the UHV set-up, the γ-STM and the optical set-up. This section provides details for each part, putting a special focus on the optical set-up that was built on the basis of previous work.

3.1.1 UHV set-up

Imaging single molecules with an STM requires UHV conditions at low temperature. UHV greatly reduces contamination from the atmosphere, while low temperature reduces the thermal drift between tip and sample and drastically reduces diffusion of the molecule on the surface. STM measurements are usually carried out at LHe temperatures of around 4.5 K. The UHV set-up (Fig. 3.1 a)) has been discussed in great detail already [59] and will only be described briefly here. The set-up consists of three chambers separated by gate valves: the load-lock, the preparation chamber, and the STM-chamber. A rotary vane pump creates a pressure of 10^{-2} mbar. Turbomolecular pumps attached to each chamber reduce the pressure to 10^{-10} mbar. Ion getter pumps attached to the preparation and STM-chamber allow to maintain 10^{-10} mbar when switching off the turbomolecular pumps during STM measurements. A titanium sublimation pump attached to the preparation chamber helps to reduce residual gas. The cryostate attached to the STM-chamber freezes gas molecules,

effectively also acting as a pump. After the set-up was vented for maintenance or repair, the preparation and STM-chambers are baked at ∼120 °C for around three days.

For transferring the sample between preparation and STM chamber, a stage attached to a manipulator is used. The stage features a filament for annealing the sample with electron bombardment. A sputter gun is also attached to the preparation chamber for cleaning the sample (see section 3.2). A *Kentax 3 cell* evaporator is used for the thermal deposition of molecules. It can be attached to the preparation chamber or the load-lock depending on the experiment.

3.1.2 γ-STM

An STM allows the imaging of nanostructures and investigation of their electronic properties. The home-built γ-STM [58, 59] (Fig. 3.1 b)) extents the possibilities of experiments by enabling the interaction of light with the nanostructures inside the tunneling junction. The γ-STM features a mirror tip [58, 59], microfabricated by direct laser writing (DLW) [54–57]. The direct laser writing process was developed by the Wegener group. It is based around the principle of polymerizing liquid resin with highly focused laser light, thus creating nanostructures. Since the material used for DLW is neither electrically conducting, nor particularly reflective, the mirror tip is coated with chromium and silver by sublimation in the load-lock. The mirror tip design features a parabolic mirror that incorporates the STM tip (Fig. 3.1 d)). This design increases the photon collection efficiency about an order of magnitude [58] in comparison to conventional γ-STMs using lenses to focus the light, hence covering a smaller solid angle. The mirror tip is printed on a metal carrier disc that is attached to a ferule (Fig. 3.1 c)). The end of the optical fiber has a corresponding counter piece that allows to attach the mirror tip by using the friction between ferrule and counter piece. A modified sample plate featuring magnets is used for exchanging the mirror tip in the STM without opening the UHV system.

The body of the γ-STM is based on the Pan design [116], the cryostate is based on the design by Zhang et al. [117]. The sample can be moved by piezo elements in both horizontal directions, while additional piezo elements enable the coarse motion of the scanner tube in the vertical direction. The scanner tube itself is also made out of piezo elements that control the fine motion of the tip which creates the STM topography image. The STM body can be pressed against the cryostate to maximize thermal contact which is helpful to cool down samples faster. Additionaly, fine copper wires transport heat between the cryostate and the STM body. This way, the STM is thermally connected to the cryostate also during scanning, when the STM body is suspended on springs to decrease vibrations.

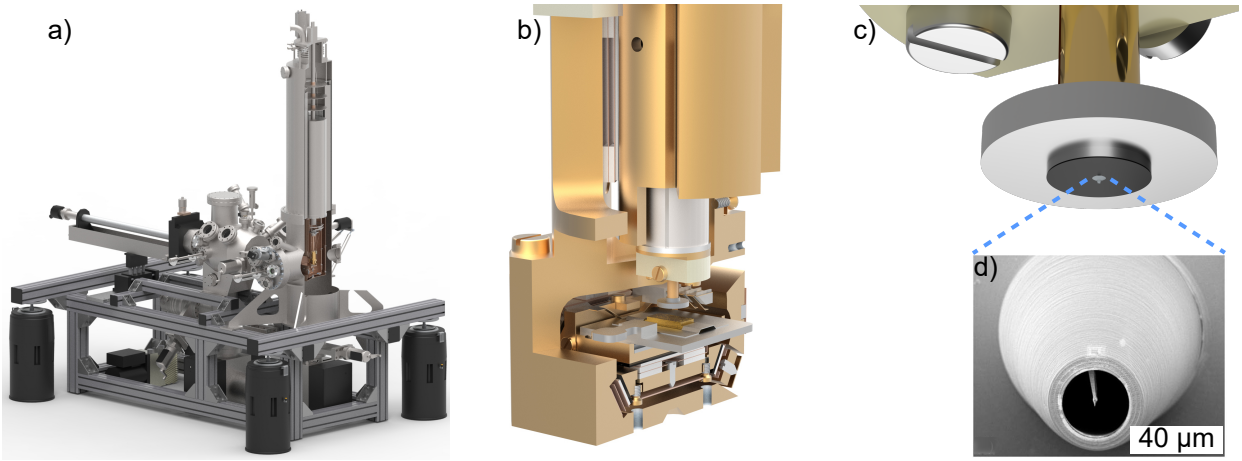

Figure 3.1: a) Render of the UHV set-up. b) Render of the γ-STM body with sample and mirror tip. c) Close-up render of the mirror tip printed on a metal disc with ferrule attached to the glass fiber. d) SEM picture of a mirror tip with parabolic mirror on the outside and STM tip on the inside. a), b) and d) are reprinted from [58], with the permission of AIP Publishing.

3.1.3 Optical set-up for PL and TCSPC

The optical set-up for investigating the light emitted inside the tunneling junction [58, 59] (Fig. 3.3) was extended as part of this thesis to improve accessibility and flexibility and enable time correlated single photon counting (TCSPC) measurements. While the previous setup was based on the 300 mm cage system by *Thorlabs*, the improved setup is mounted on an optical breadboard within a dark enclosure. A *9530 Series Pulse Generator* by *Quantum Composers, Inc.* sends a trigger signal to the light source. In this work, an *Alphalas Picosecond Laser Diode Driver PLDD-100M* with a *PICOPOWER-LD-375* laser diode ($\lambda = 375$ nm, 30 ps, 1 W peak power) (Fig. 3.3, blue lines) was used. The light is then guided through an optical fiber towards an array of lenses and filters. A replaceable filter ensures a narrow wavelength range. The lenses focus the light through an opening in the off-axis parabolic mirror onto an angled physical contact (APC) optical fiber that guides the light either into the preparation chamber or the STM chamber in UHV. In the preparation chamber (set-up A) two optical fibers are used, one for excitation and one for light collection. This reduces auto-fluorescence from the glass of the optical fibers. In the STM chamber, either a mirror tip (set-up C) or an optical fiber without mirror tip (set-up B) is used. Not using a mirror tip increases light collection due to covering a larger solid angle. In this case, an empty mirror tip carrier disc is attached to the metal ferrule of the glass fiber as a spacer and for protecting the fiber from contamination. For set-up A, the PL response (red lines) is guided towards the SPADs or towards the spectrometer with a mirror insert (iv). For set-ups B and C, the PL response is reflected by the off axis parabolic mirror onto a motorized mirror (i). The off-axis parabolic mirror was chosen over a dichroic beamsplitter to reduce the amount of interfaces and increase collection efficiency. The PL light is guided through a longpass filter by the off-axis parabolic mirror. The longpass filter blocks most of the signal in the range of the exciting light. The motorized mirror allows to guide the light either towards

the SPADS via a second mirror (ii) or towards the spectrometer. The motorized mirror furthermore allows automatizing measurements by being able to switch between SPADs and spectrometer electronically, but adjustment can be tedious. For this reason, a mirror insert (iv) was used instead. A dichroic beamsplitter insert (iv) can also be used to measure PL and TCSPC at the same time. However, this reduces the signal, and was therefore avoided. The spectrometer consists of an *Acton SP-2156* spectrograph with a diffraction grating with 300 grooves/nm^2 and a *PyLoN 100 B CCD camera* by *Princeton Instruments*. The SPADs are two photon counting modules *SPCM-AQRH-14TR-BR1* from *Excelitas* (max. countrate 37 Mcps, 22 ns dead time) forming a HBT interferometer when used in combination with a beam splitter. The HBT set-up reduces dead times, but for most experiments only one SPAD is used for simplicity. Both SPADs are equipped with a motorized filter wheel. The SPADs are connected to a *qutag-standard time to digital converter* from *qutools*. A high frequency optical chopper (5 Hz - 110 kHz) from *Edmund optics* was added to the set-up for discretizing the PL light, if needed.

For the first experiments, PL measurements were carried out in atmosphere, but they were soon moved inside the UHV set-up to avoid contamination and possible degradation by oxygen and water. A PL set-up inside the preparation chamber was developed that allows to measure PL of samples placed in the stage of the manipulator (Fig. 3.4 a)). This way, the progress of our experiments was accelerated, because STM measurements could be carried out in parallel. Furthermore, this PL set-up allowed to have two individual glass fibers for excitation and light collection, which reduces autofluorescence. Developing this set-up was an important step towards the understanding of molecular films on substrates and allowed us to gain understanding in the impact of metallic vs. dielectric substrates on light emission. Next to the PL set-up in the preparation chamber, PL measurements can also be performed inside the STM with or without the mirror tip (Fig. 3.4 b)). Using the mirror tip focuses the excitation light onto a small area and increases the Purcell factor for molecules within the tunnel junction. However, for PL measurements on films of several 10 ML, illuminating a bigger area is advantageous. For this reason, an empty tip carrier disc with a hole of the size of the glass fiber might be used. This empty disc acts as a spacer between fiber and sample while also enabling tunneling for the approach. Approaching the glass fiber until tunneling contact is reached ensures a reproducible fiber-sample distance.

Optical fibers are known to exhibit autofluorescence, which means their material is susceptible to being excited by the transmitted light to emit luminesce, itself. This undesired signal has been a topic of research especially in the medical sector [118–120]. The autofluorescence signal exited within the fiber is assumed to scatter uniformly forwards, i.e. towards the sample and backwards, i.e. back towards the optical set-up. Therefore, when a single optical fiber is used for excitation and light collection, as is the case for PL experiments inside the STM, half of the autofluorescence signal goes towards the spectrometer or the SPADs. Since emission from autofluorescence covers a large wavelength range, it cannot entirely be blocked by a longpass filter. For this reason, the suppression of autofluorescence by photo-bleaching is of interest for PL experiments. Silica fibers doped with Germanium show a fast bleaching of the autofluorescence within the first few minutes [121] going down

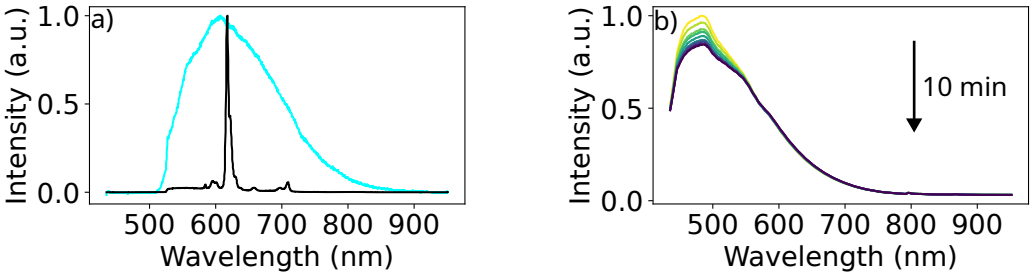

Figure 3.2: Normalized autofluorescence signal of the optical fibers with: a) a clean glass sample (cyan) and a reference Eu^{3+} PL signal (black) in the PL set-up with two optical fibers in the preparation chamber at room temperature with a 525 nm longpass filter. λ = 375 nm, f=50 MHz. b) A clean Ag(111) sample in the PL set-up inside the STM at 4.5 K with a 400 nm longpass filter. The autofluorescence signal decreases about 10 % within 10 min due to bleaching of the optical fiber. λ = 375 nm, excitation frequency = 50 MHz.

as much as 25 % within a few hours [122]. However, the bleaching of autofluorescence is also known to recover with time [123] and temperature [124, 125].

The autofluorescence was measured for the PL set-up utilizing two fibers in the preparation chamber and for the PL set-up using the γ-STM. In both cases a clean sample was used as a reference and a pulsed laser with 375 nm running at 50 MHz used for excitation. For the measurement in the preparation chamber, a clean glass sample was placed underneath the optical fibers. The response normalized to its maximum is shown in Fig. 3.2 a). A longpass filter suppresses most of the excitation light and part of the PL signal. The spectrum is not smooth but shows some characteristic shoulders. While Eu^{3+} contamination within the UHV system cannot be excluded with certainty, the signal of the clean sample does not seem to match with the overlaid Eu^{3+} spectrum. The features of the spectrum might therefore be intrinsic to the sample or the fibers but was not investigated in detail. For the measurement in the γ-STM a clean Ag(111) sample was placed underneath the optical fiber with an empty tip carrier disc installed. The PL signal was measured at an excitation wavelength of 375 nm with a frequency of 50 MHz. A 400 nm longpass filter was usually used to suppress the excitation light. The time resolved PL signal shows a reduction in intensity of about 10 % during the measurement period of 10 min (Fig. 3.2 b)) which is attributed to a bleaching of the optical fiber. A possible bleaching of the glass sample is considered negligible, given that the optical fiber consists of a lot more fluorescing material. It has a length of approximately 2 m while the glass substrate has a thickness of 1 mm. The autofluorescence signal depends greatly on the exact position and orientation of the optical fiber towards the sample. It is therefore not possible to simply subtract the reference signal of the clean sample from the PL signal of interest. For this reason, the autofluorescence background was subtracted in this work by fitting a suitable spline [126].

TCSPC measurements rely on the principle of measuring the time difference between the

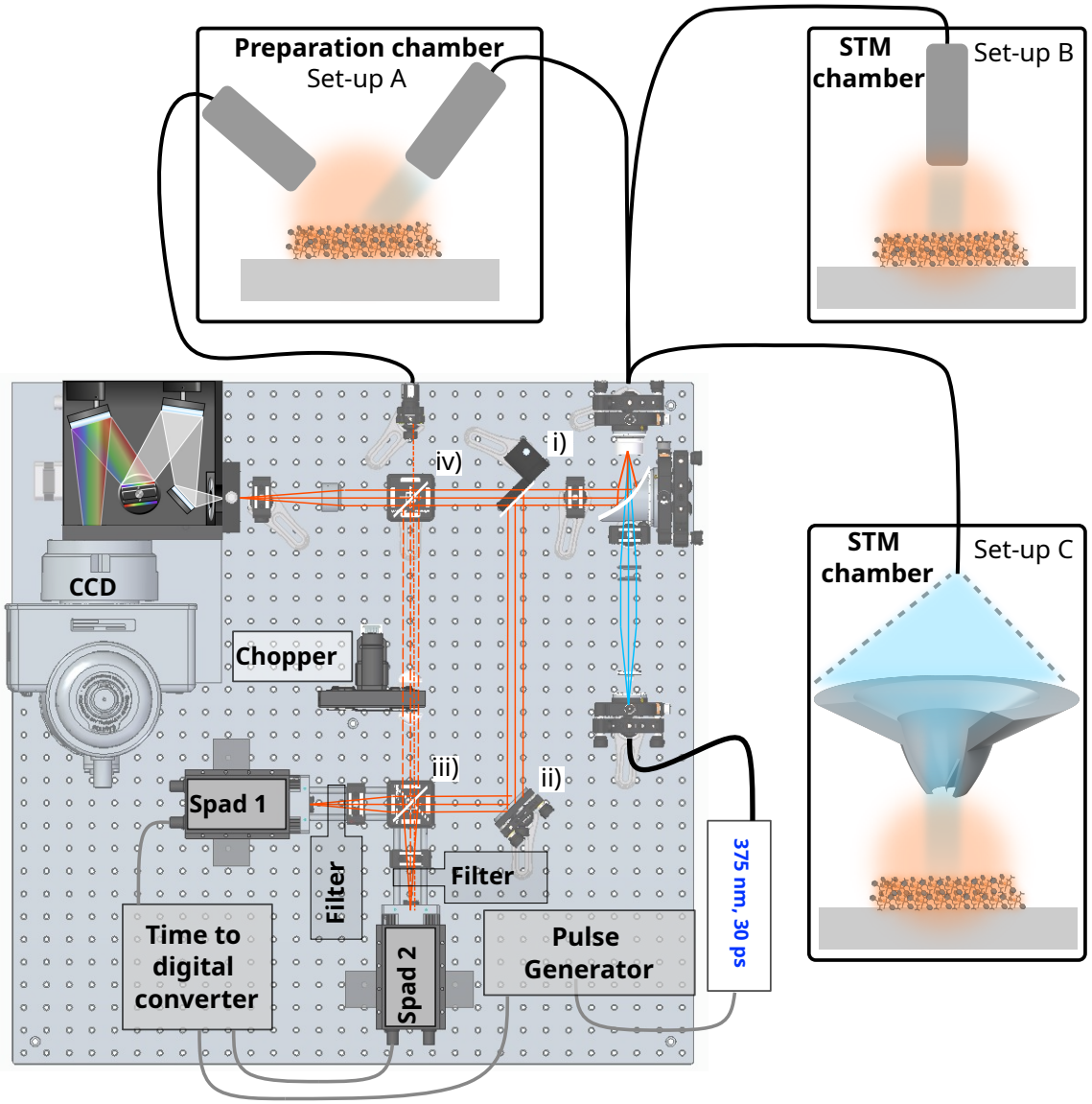

Figure 3.3: Schematic drawing of the optical set-up. The Quantum composer sends a trigger signal to the pulsed laser (375 nm, 30 ps) represented by blue lines. The light is guided through an off-axis parabolic mirror with an opening and coupled into an optical fiber leading either inside the preparation chamber or the STM chamber in UHV. The set-up in the preparation chamber features two optical fibers (set-up A). In the STM chamber either a glass fiber (set-up B), or a mirror tip (set-up C) can be used. For set-up A, the PL response (red lines) is guided towards the SPADs or towards the spectrometer using a mirror insert (iv). For set-ups B and C, the PL response is reflected by the off-axis parabolic mirror either onto a motorized mirror (i), followed by a second mirror (ii) towards the SPADs or, when the motorized mirror clears the path, towards the spectrometer. Instead of using the motorized mirror, the PL response from set-up B and C can also be guided towards the SPADs by a mirror insert (iv), when automization by the motorized mirror is not needed. The PL light can be divided between both SPADs with a dichroic beam splitter insert (iii). Filter wheels in front of both Spads allow to detect the PL response at different wavelengths. A chopper wheel was implemented for discretizing the PL response, if needed.

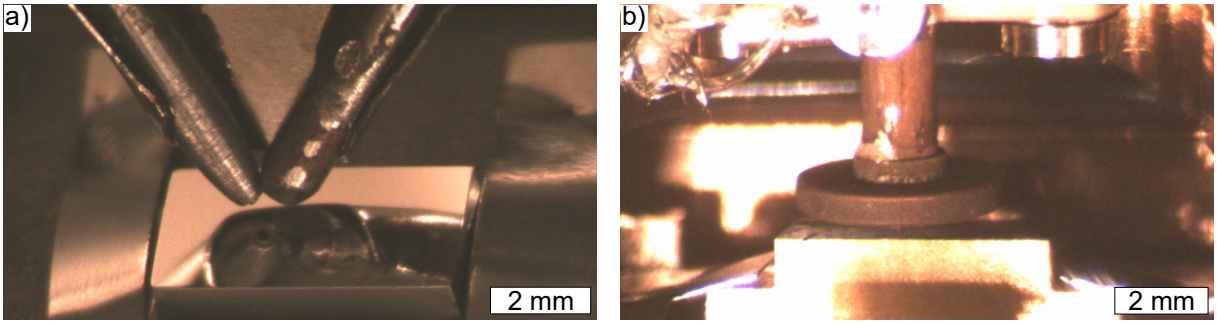

Figure 3.4: a) Picture of the PL setup inside the preparation chamber. Two optical fibers are positioned above a sample, one fiber guides the light for excitation towards the sample, the other fiber collects the PL response. b) Picture of the tunneling junction inside the STM which is also used for PL measurements. The tip carrier disc is positioned above the sample. Either an empty carrier disc or a mirror tip is used.

excitation pulse and the PL response (Fig. 3.5 a)). The pulse generator sends a trigger signal to the laser diode driver and to the time to digital converter. The latter acts as a reference start signal to calculate the time difference. The laser diode driver controls the laser diode which emits an excitation pulse after receiving the trigger signal. Several laser pulses require several trigger pulses. The light pulses are guided towards the sample which in turn responds with the PL signal that is detected by the SPAD. The SPAD then sends out an electric signal to the time to digital converter which creates a time stamp for each signal received from the SPAD on one input or the reference signal on the other input. The TCSPC experiment consists of many measurement periods (Fig. 3.5 b)). In the most simple picture, a single light pulse (blue) is sent towards an individual molecule that emits a photon (orange) after a certain time. In the case of the spontaneous emission of a photon, the time difference between excitation and response will be exponentially distributed. Repeating this process of excitation and detection many times leads to a histogram that describes the statistics of detecting a photon within a time interval after excitation. The spontaneous emission of light from an excited molecule is described by an exponential decay (see section 2.3). The thus obtained decay constant defines the observed lifetime which is a property that strongly varies depending on the local chemical and physical environment.

In this work, PL was always measured on more than one molecule. If several decay processes from different initial states contribute to the PL response, a multiexponential decay is observed in the TCSPC measurement. This is for example the case, when there are different species of light emitting molecules, different environments or orientations of one species. In Eu^{3+} the main emission bands originate from the $^5D_0 \rightarrow {}^7F_J$ transition. This does, however, not mean that the ligands transfer their energy directly to the $^5D_0$ state. A filling effect is observed when the decay of the $^5D_0$ state is tracked [112, 115, 128–130], which means the PL response is not most intense right after excitation, but increases with time before the exponential decay sets in. This energy transfer time is often called rise time. It will

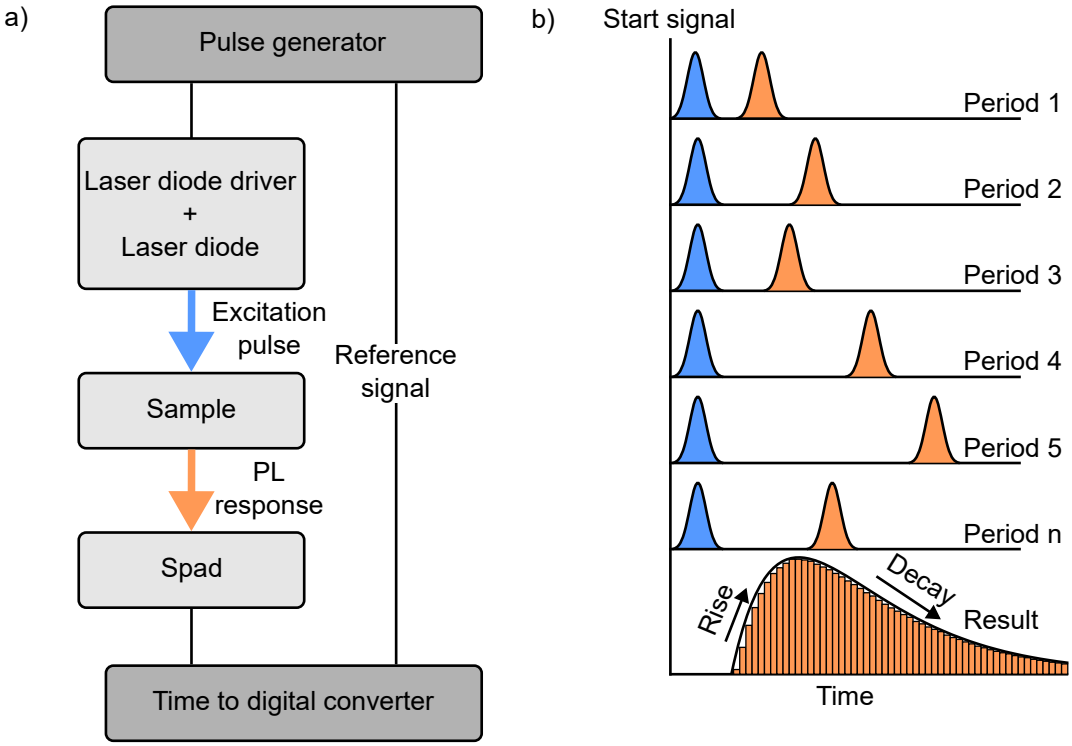

Figure 3.5: a) Wiring scheme of the TCSPC measurement. The pulse generator simultaneously sends a trigger signal to the laser diode driver and a reference signal to the time to digital converter. The laser diode sends out a light pulse for each trigger input. The light is guided to the sample for exciting PL. The PL response is then guided towards the SPAD. The SPAD sends an electrical pulse to the time to digital converter for each detected photon. The time difference between reference signal and detected photon is then calculated. b) For each period, the time difference between the excitation light and the PL response is measured. When the light emitting state is not directly excited by the excitation light, the histogram of the PL response first rises and then declines exponentially with time. After [127].

be shown in section 3.6.5 that the rise time of Eu^{3+} complexes does not correspond with energy transfer from the ligands to the Eu^{3+} but with the decay of the higher excited state $^5D_1$ of the Eu^{3+} ion itself. The energy is therefore not transferred from the ligands to the $^5D_0$ state directly.

3.2 Sample preparation

Investigating molecules with an STM requires depositing them on a substrate that is flat and clean at the atomic scale. In this thesis, the substrate for STM measurements consists of a single crystal of either Ag(111) or Au(111) purchased from MaTeck with a purity of 99.999 % polished to a roughness <0.01 µm with orientational accuracy $< 0.1°$. The procedure for cleaning the substrate and the different methods used for depositing molecules are described in the following paragraphs.

3.2.1 Substrate cleaning

Before depositing molecules on the substrate, it has to be cleaned which means molecules that were deposited before have to be removed via sputtering. In this case, sputtering refers to the process of bombarding the substrate with Ar^+ ions with an energy of 1.5 keV for 15-20 min which removes any molecules adsorbed to the surface as well as the upper most layers of the substrate itself. The bombardment with Ar^+ ions leaves craters on the surface. Annealing the substrate leads to a relaxation of the atoms into the crystal lattice, therefore creating flat terraces of several hundred nanometers. Annealing also enhances the diffusion of impurities from the bulk to the surface. For Ag(111) and Au(111) the annealing temperature is set to 600 °C for 5-10 min. Usually three repetitions of sputtering and annealing are sufficient to achieve a clean substrate.

3.2.2 Thermal sublimation of molecules

Thermal sublimation offers a finely controllable method for depositing molecules. The molecular material is filled into a crucible that is heated in UHV. A comercially available *Kentax 3-cell* evaporator is used for sublimation. The evaporator features three crucibles that can be heated independently or in combination. A shutter in front of the crucibles ensures precise control over the deposition time while a water cooling line prevents the neighboring crucibles from heating up. Enabling the precise control of the deposition was done as part of this thesis. For this reason, a quartz crystal microbalance was added to the manipulator head in the preparation chamber. The quartz crystal microbalance allows to monitor the deposition rate by measuring the shift of the eigenfrequency of an oscillating quartz crystal when material is deposited. While this is a commonly used technique, its implementation was not straight forward. Positioning the quartz crystal microbalance at the manipulator head allows to quickly change between depositing on the quartz crystal microbalance and depositing on the substrate. However, this position requires approximately 2 m of wiring which easily catches interference signals and increases the impedance. An even bigger problem are vibrations transmitted through the manipulator to the quartz crystal microbalance,

especially when the turbo molecular pump is running. For this reason, and also to avoid contaminating the preparation chamber with the evaporated material, the evaporator and the quartz crystal microbalance were moved to the load-lock which allows short wires and a sturdier mounting.

Even when utilizing a quartz crystal microbalance, finding the right temperature for subliming organic complexes is challenging. Below the sublimation temperature of the complexes, fragments and impurities will degas that show up as a signal in the quartz crystal microbalance which can lead to misinterpretations. At temperatures above the sublimation temperature, the complexes might start to decompose. Distinguishing these three regions is often not obvious. It was found that the quartz crystal microbalance indicates a deposition when the crucible is heating up, even when the shutter is closed. The shutter is a metal plate that does not seal the crucibles tightly but simply blocks the direct path of evaporating material. When the quartz crystal microbalance signal is not conclusive, increasing the temperature step-wise while monitoring the pressure can be helpful for finding the right sublimation temperature. When material starts to sublime, the pressure will usually increase at least one order of magnitude. For this thesis, it was essential to not only sublime molecules in a sub-monolayer coverage which is often sufficient for STM, but to deposit thin films of molecules onto the substrate with controlled thickness (see section 3.6.6). This was done by heating the crucible up to 10-20 °C less than the sublimation temperature first. When the shutter is closed, the deposition rate should be zero. This is often not the case for freshly filled crucibles that then require degassing for ∼10 h. When opening the shutter, there should be a significant change in the deposition rate. This change is usually already present below the sublimation temperature but with lower deposition rate. The deposition rate itself heavily depends on the history of the crucible. Newly filled crucibles should not only be degassed at temperatures below the sublimation temperature but also kept at sublimation temperature for some time before preparing a sample. The deposition works best, i.e. in the most controlled manner when the crucible has already been used many times for preparing a sample. There is a sweet spot after filling a crucible where the deposition rate is stable over a long period of time and for many sample preparations, even after exposure to atmosphere. After filling the crucible, the deposition rate is unstable and can be so high that no controlled deposition is possible. After sufficient degassing, controlled deposition is possible, but at some point the material in the crucible is exhausted. The deposition rate then decreases significantly.

A changing appearance of the material inside the crucible is often observed in betadiketonate based Eu^{3+} complexes. The molecules start as a white or yellow powder or crumbs. If the material is available as crumbs after synthesis is should be preferred for sublimation and not milled into a powder. Powder is more susceptible to absorb contamination from atmosphere and milling might damage the molecules. Upon heating the crucible the material starts to change its appearance. It starts to melt and forms a solid plug of brown to black color at the bottom of the crucible. The walls of the crucible are coated with yellow to brown residue. This residue also appears on the closed shutter after sufficient evaporation/degassing and is believed to consist of intact complexes. When the material is

exhausted, it leaves behind a dark coal like plug in the crucible with hardly any yellow or brown residue. This was not observed for trensal based complexes.

The sublimation of trensal based complexes proved even more difficult. For most complexes, it was not possible to obtain a conclusive signal in the quartz crystal microbalance. For this reason, vacuum spray deposition was mostly preferred.

3.2.3 Vacuum spray deposition

While sublimation allows to precisely control the deposition by adjusting the temperature of the crucible and the deposition time, it is not suitable for all molecules. Some molecules might decompose before sublimating. In this case, vacuum spray deposition might be used [131, 132]. For this method, the material is dissolved and the solution is sprayed onto the substrate. Spraying is done by placing the substrate underneath a pinhole opening in the load-lock. A second pumping stage ($\sim 10^{-2}$ mbar) between the pinhole opening and the load-lock reduces contamination by atmosphere. The solution is then placed onto the opening with a capillary. The vacuum spray deposition is usually followed by an annealing step to facilitate diffusion and reduce remains of the solvent.

3.2.4 Overview of Ln complexes and ligands

This section provides an overview of the ligands and Eu^{3+} complexes investigated in this thesis. The ligands as shown in Fig. 3.6 are:

- **bpy** [52, 91, 92, 105–110, 133]:
  2,2'-bipyridine
- **tta** [52, 92, 105–107, 133]:
  1-(2-Thenoyl)-3,3,3-trifluoroacetone
- **btfa** [52, 91, 108–110, 133]:
  1-Phenyl-3,3,3-trifluoro-2,4-pentanedione

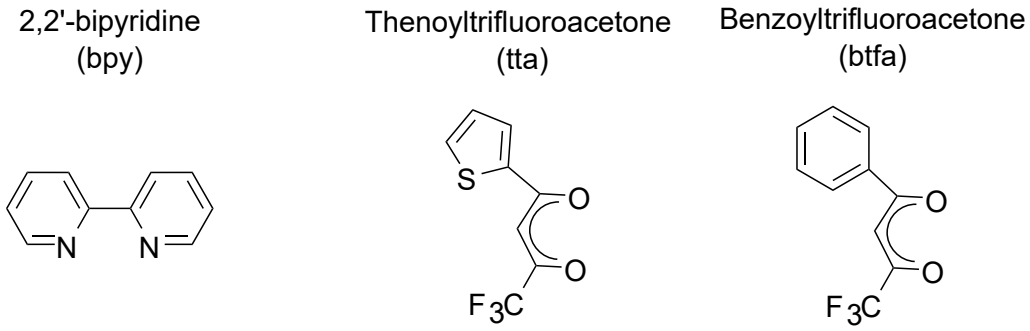

Figure 3.6: Structure drawings of antenna ligands.

The complexes as shown in Fig. 3.7 are:

- **[Eu(tta)$_3$(bpy)]** [92, 105, 133, 134]:
  Europium, (4,4-bipyridine-κN_1) tris[4,4,4-trifluoro-1-(2-thienyl)-1,3-butanedionato-κO_1,κO_3]-(ACI)

- **[Eu(btfa)$_3$(bpy)]** [91, 108, 109, 133]:
  Europium, (2,2-bipyridine-κN_1,κN_1) tris(4,4,4-trifluoro-1-phenyl-1,3-butanedionato-κO_1,κO_3)-, (SA-8-11221323)- (ACI)

- **[Eu(tta)$_3$(H$_2$O$_2$)]** [42, 95, 111, 112, 135]:
  Europium, diaqua tris[4,4,4-trifluoro-1-(2-thienyl)-1,3-butanedionato-κO_1,κO_3]-(ACI)

- **[Eu(trensal-Ph-SMe)]**:
  Europium, [[4,4,4-[nitrilotris[2,1-ethanediyl(nitrilo-κN)methylidyne]]tris[4-(methylthio)[1,1-biphenyl]-3-olato-κO]](3-)]-, (OC-6-22)- (ACI)

- **[Eu(trensal)]** [113, 136–139]:
  Europium, [[2,2,2-[(nitrilo-κN)tris[2,1-ethanediyl(nitrilo-κN)methylidyne]]tris[phenolato-κO]](3-)]-, (OCF-7-3-212121)- (9CI, ACI)

- **[Eu(trensal-O-Bn)]**:
  Europium, [[2,2,2-[(nitrilo-κN)tris[2,1-ethanediyl(nitrilo-κN)methylidyne]]tris[4-(benzyloxy)phenoxy-κO]]-, (OC-6-22)- (ACI)

- **[Eu(TACN)]**:
  Europium, (1,4,7-triazacyclononane-κ^3N) tris(-diketonato-κ^2O,O)-, (OC-9-33)- (ACI)

- **[Tb(TACN)]**:
  Terbium, (1,4,7-triazacyclononane-κ^3N) tris(-diketonato-κ^2O,O)-, (OC-9-33)- (ACI)

[Eu(tta)$_3$(bpy)] was synthesized by Dr. Julia Feye from the group of Prof. Peter W. Roesky at the Institute of Inorganic Chemistry (KIT). [Eu(btfa)$_3$(bpy)] and [Eu(tta)$_3$(H$_2$O)$_2$] were synthesized by Dr. Barbora Brachnakova and Dr. Senthil Kumar Kuppusamy from the group of Prof. Mario Ruben at the Institute of Nanotechnology (KIT). [Eu(trensal-Ph-SMe)], [Eu(trensal)], [Eu(trensal-O-Bn)], [Eu(TACN)] and [Tb(TACN)] were synthesized by Lisa Biener and Timo Neumann from the group of Prof. Michael Seitz at the Institute of Inorganic Chemistry (University of Tuebingen).

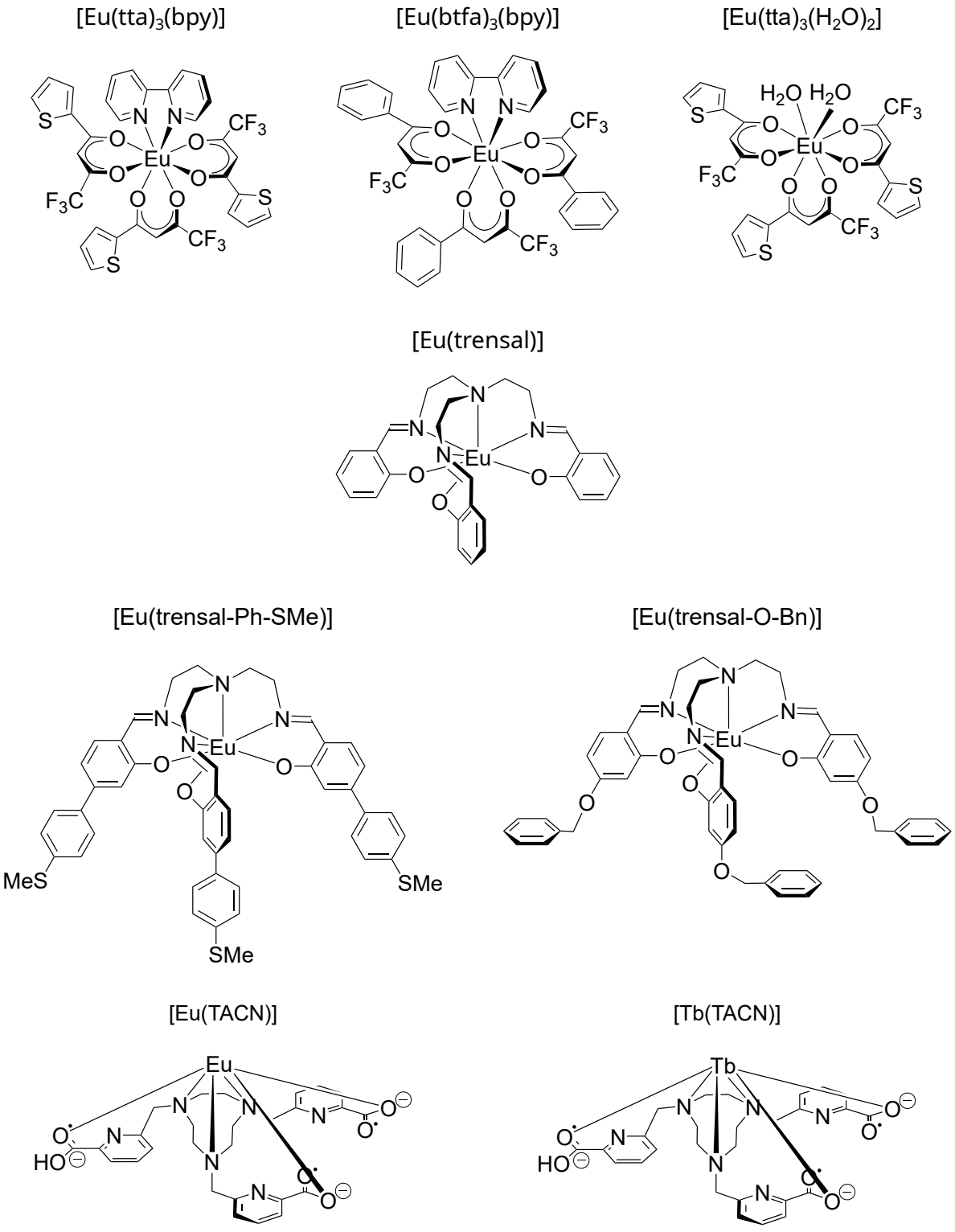

Figure 3.7: Structure drawings of Ln complexes used in this work.

3.3 STM topography of betadiketonate complexes

While STM topography offers the possibility to create an image of the adsorption of molecules on the surface of the substrate, identifying the molecules is still challenging. In the best case, the molecules have a distinct shape and adsorb on the substrate with a preferred orientation. Objects with the same shapes are then present in the STM image. A deviating shape is taken as an indication for a different orientation or a different type of molecule. A different type of molecule could be introduced by impurities or contamination already present in the material used for sublimation, or contamination within the vacuum chamber. Contamination can also arise when the sample is kept exposed in the chamber at low temperatures, e.g. in the precooling stage. Furthermore, molecules can dissociate when adsorbing on the metal surface [140] or due to the sample preparation method. Sublimation introduces energy into the material in the form of heat which can break bonds. Vacuum spray deposition requires to dissolve the material which not only introduces contamination from the solvent but the interaction with the solvent can also lead to dissociation. Both cases lead to fragments detaching from the molecule and potentially adsorbing on the substrate.

A comparison with literature of STM or AFM images of the same or similar molecules can be helpful to obtain information about what characteristic to expect. The approximate size of the molecules can be estimated from the molecular structure, however the actual size in STM can vary since it depends heavily on the exact adsorption and atomic forces and STM data also includes information about the density of states, not just the physical size.

$[Eu(btfa)_3(bpy)]$, $[Eu(tta)_3(bpy)]$ and $[Eu(tta)_3(H_2O)_2]$ were chosen as a starting point for experiments because they are well known in literature (see section 3.2.4). $[Eu(btfa)_3(bpy)]$ and $[Eu(tta)_3(bpy)]$ share the bpy ligand, while $[Eu(tta)_3(bpy)]$ and $[Eu(tta)_3(H_2O)_2]$ share the tta ligand. These similarities allow to compare their opto-electronic properties by determining the impact of different ligands. To investigate these properties, the sample preparation process had to be established first by checking the adsorption of the complexes on the substrate with STM topography.

Estimating the intactness and adsorption of $[Eu(btfa)_3(bpy)]$, $[Eu(tta)_3(bpy)]$ and $[Eu(tta)_3(H_2O)_2]$ with STM proved difficult. These complexes have C1 symmetry, with ligands of similar size and shape which makes it particularly difficult to obtain information from STM. STS can offer another point of reference for orientation and composition of the molecules. However, in practice performing STS on organic complexes is challenging, since they are usually not strongly adsorbed on the surface and can thus move when sweeping the bias at higher voltages which is necessary for spectroscopy measurements. The weak adsorption can also lead to molecules sticking to the tip which changes its density of states and therefore also the dI/dV curve. To successfully perform STS measurements, the dI/dV signal of the molecule has to be compared to the dI/dV signal on the clean substrate, going back and forth, in order to identify spectroscopic features intrinsic to the molecule. Therefore, STS did not prove a feasible way for reliably distinguishing molecules on the surface. When using only STM topography, reappearing shapes and patterns driven by self-assembly

processes might be considered to be formed by the same type of molecule oriented in a specific way. We found patterns formed by self-assembly for all three complexes that were attributed to the composition of their ligands [52]. However, in further experiments, these patterns turned out to be formed by the ligands alone.

Before the quartz crystal microbalance was implemented in the sample preparation set-up which allows to monitor the deposition rate while subliming material, the sublimation temperature of [Eu(tta)$_3$(bpy)] and [Eu(btfa)$_3$(bpy)] was estimated by step wise increasing the temperature until the pressure in the chamber increased significantly. Material was then deposited on a clean glass substrate for more than 30 min and the thus prepared sample checked for the typical Eu^{3+} PL spectrum. The growth and thickness of these samples was unknown but the thick layer of deposited material was visible by eye and therefore considered as bulk. The PL spectra proved that sublimation is a suitable method for preparing light sensitive samples. The PL spectra and lifetimes of these bulk samples will be shown in section 3.6.1. While this method of sample preparation was successful and could also be used to prepare samples for STM measurements, the interpretation of the STM data was challenging. [Eu(tta)$_3$(bpy)] and [Eu(btfa)$_3$(bpy)] samples prepared at 160 and 150 °C respectively, showed the self-assembly of small uniform molecules. After adding the quartz crystal microbalance and monitoring the deposition rate, the temperature for sublimation was increased to 185 °C. As it turned out, the molecular material requires purification by keeping the crucible at 150 °C for $\sim$ 10 h to get a reliable deposition rate and clean samples as will be shown in the next paragraphs. [Eu(tta)$_3$(H_2O)$_2$] was deposited using vacuum spray deposition due to an expected cleaving of the water ligands upon sublimation.

3.3.1 Sublimation of [Eu(tta)$_3$(bpy)] and [Eu(btfa)$_3$(bpy)] at temperatures $<$ 185 °C

[Eu(tta)$_3$(bpy)] was sublimed onto clean Au(111) at a crucible temperature of 160 °C for 3 min. In the STM topography of this sample, we observed a sub-monolayer coverage of molecules following the herringbone reconstruction (Fig. 3.8 a)). The molecules are homogeneously distributed on the surface with uniform shapes and sizes. The molecules tend to align in chains, roughly following the herringbone template (Fig. 3.8 b)). The periodicity of these chains was determined with a height profile to 0.65 nm (Fig. 3.8 c)). The molecules have a distinct shape of two lobes with a nodal plane in between which becomes apparent in STM images of single isolated molecules (Fig. 3.8 d)). Here, also the different orientations of these molecules are distinguishable. The apparent height of a single isolated molecule was determined and the cross-section fitted with a double gaussian (Fig. 3.8 e)). The thus determined center to center distance is 0.67 nm. These results were published in [52].

[Eu(btfa)$_3$(bpy)] was sublimed onto clean Au(111) at a crucible temperature of 150 °C for 3-5 min depending on the desired coverage. At a coverage close to 1 ML, the molecules start to form chains with short range order (Fig. 3.9 a)) similar to what we observed for the [Eu(tta)$_3$(bpy)] sample, but with a weaker template effect by the herringbone reconstruction.

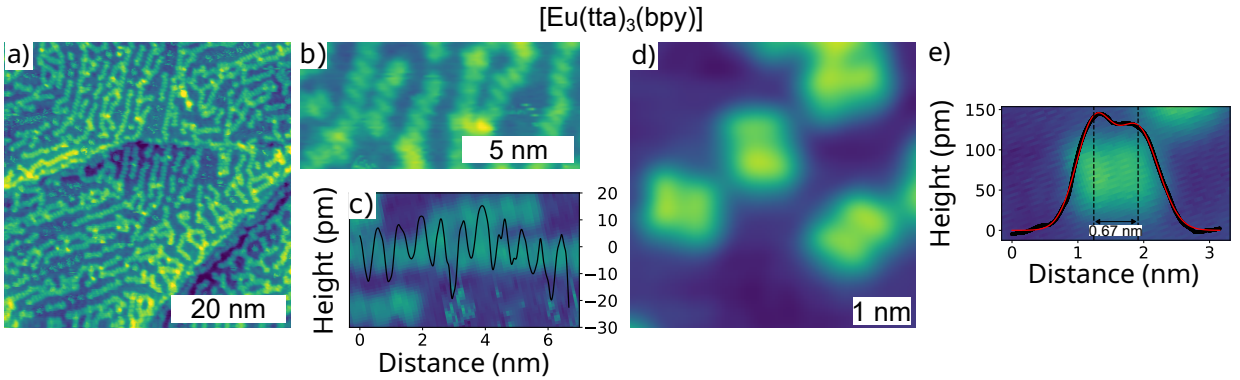

Figure 3.8: STM topography of the self-assembly of ligands and Eu^{3+} complexes on [Eu(tta)$_3$(bpy)] samples on Au(111) after sublimation at 160 °C. a) Ligands adsorbed on the Au(111) surface following the herringbone template at sub-monolayer coverage. (1.0 V, 4 pA). b) Close-up view of ligands forming chains with c) cross-section. (1.0 V, 4 pA). d) Close-up view of single ligand molecules with different orientations (1.0 V, 4 pA). e) Cross-section of a single molecule, fitted with a double gaussian and center to center distance. (1.0 V, 4 pA). Adapted from [52].

At a coverage above 1 ML, the molecules form a large scale lattice with bigger agglomerates on top of the lattice (Fig. 3.9 b)). The lattice directions as indicated by the red arrows, follow the $\langle 1\,1\,\bar{2}\rangle$ and $\langle \bar{1}\,2\,\bar{1}\rangle$ directions of the Au(111) surface. At the mirror axis of the Au(111) surface, a domain boundary was observed as indicated by the black circle. Since the packing of the molecules is less dense at the domain boundaries, the second layer of molecules preferably nucleates there. However, a domain might also stretch over the mirror axis, breaking the Au(111) symmetry, which indicates high mobility of the molecules and a strong inter molecular interaction. A close-up STM topography image of the lattice is shown in Fig. 3.9 c). The unit cell is represented by the unit cell vectors as indicated by the red arrows. The unit cell was determined to 1.2 nm^2 containing two molecules. On samples with low coverage, the motif of single molecules is apparent (Fig. 3.9 d)). Similar to [Eu(tta)$_3$(bpy)], it can be identified as two lobes with a nodal plane. At low coverage, these molecules nucleate at the elbows of the herringbone reconstruction with preferred orientation perpendicular to the mirror axis. The inset in Fig. 3.9 d) shows three single molecules with different orientations. The cross-section of a single molecule was fitted with a double gaussian and the center to center distance determined to 1.03 nm (Fig. 3.9 e)). These results were published in [52].

As shown in the previous paragraphs, elongated molecules consisting of two lobes with a dark nodal plane are present on the samples of [Eu(tta)$_3$(bpy)] and [Eu(btfa)$_3$(bpy)] sublimed at 160 and 150 °C, respectively. These molecules show the tendency to align into chains with short range order, and in the case of [Eu(btfa)$_3$(bpy)] to form a lattice with large scale order. However, on the sample of [Eu(btfa)$_3$(bpy)], with coverage above 1 ML, there are also larger agglomerates in the second layer. Bipyridine, a ligand moiety present in [Eu(tta)$_3$(bpy)] and [Eu(btfa)$_3$(bpy)], is known to form lattices with large scale order on

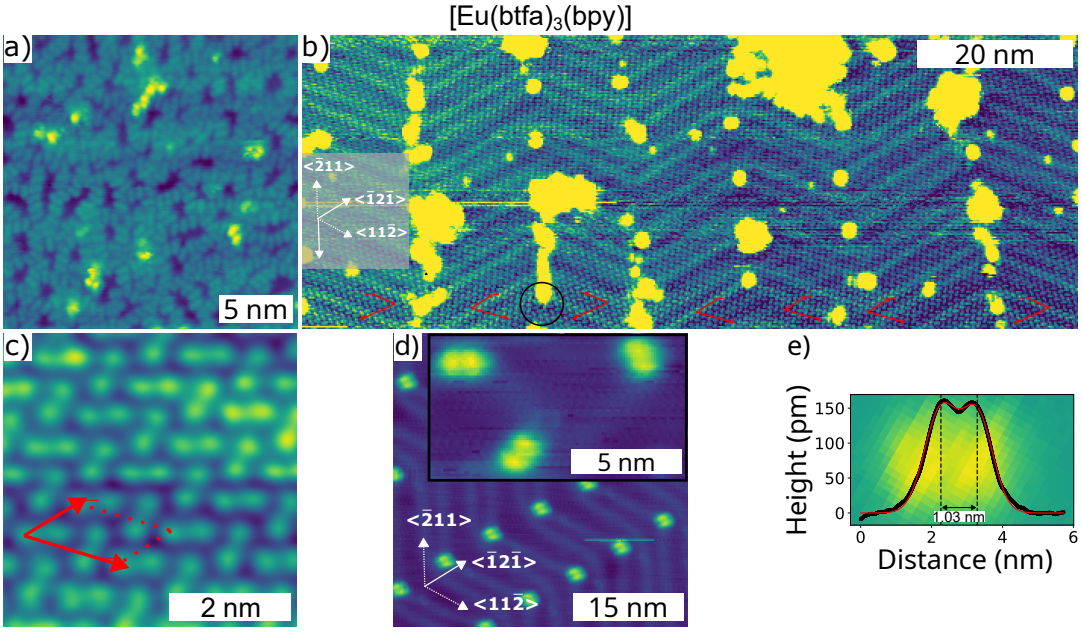

Figure 3.9: STM topography of the self-assembly of ligands and Eu^{3+} complexes on $[Eu(btfa)_3(bpy)]$ samples on Au(111) after sublimation at 150 °C. a) Ligands aligning in chains on Au(111) at sub ML coverage. (-0.4 V, 5 pA). b) Overview of near perfect lattice formation with large scale order on Au(111) at above ML coverage. Different domains are indicated by red arrows, the domain boundary is indicated by the black circle. (2.5 V, 5 pA). c) Close-up view of lattice formation on Au(111) with unit cell indicated by red arrows. The unit cell size is 1.2 nm^2 (-3.0 V, 100 pA). d) Molecules adsorbed at the herringbone elbows with inset showing molecules with different orientations. (-3.0 V, 1 pA). e) Cross-section of a single molecule with double gaussian fit and center to center distance. (-3.0 V, 100 pA). Adapted from [52].

metal substrates. While these lattices are similar in appearance to what I observed, they were reported to depend heavily on the sample preparation method. STM topography of bpy samples prepared in electrolyte solution on Au(111) shows a strong substrate potential dependence and voltage controlled phase transition [141, 142]. To further back up the assumption that most molecules on the substrate are not intact complexes but fragments, btfa molecules were sublimed onto clean Au(111) at a crucible temperature of 155 °C for 2.5 min. This resulted in a coverage of about 1 ML of evenly distributed molecules without distinguishable shape or orientation (Fig. 3.10).

It is reasonable to assume that the lattice observed on samples of $[Eu(btfa)_3(bpy)]$ and the chains with short scale order on samples of $[Eu(tta)_3(bpy)]$ are not formed by intact molecules but by fragmented ligands. This assumption is verified by the STM images of $[Eu(tta)_3(bpy)]$ and $[Eu(btfa)_3(bpy)]$ sublimed at an elevated temperature of 185 °C as will now be shown.

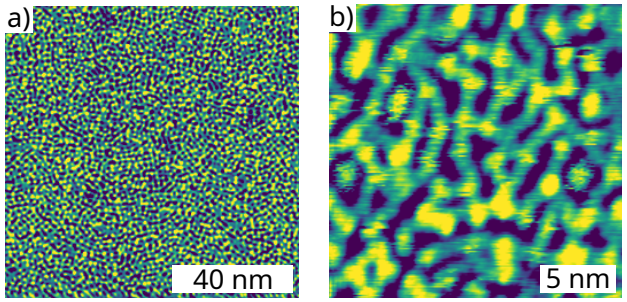

Figure 3.10: STM topography of btfa molecules on Ag(111) at coverage close to 1 ML. a) Large scale overview. (2.0 V, 10 pA). b) Close-up view. (2.0 V, 10 pA).

3.3.2 Sublimation of [Eu(tta)$_3$(bpy)] and [Eu(btfa)$_3$(bpy)] at 185 °C

[Eu(tta)$_3$(bpy)] was sublimed onto Au(111) at a an elevated crucible temperature of 185 °C for 10 s while cooling the substrate to -75 °C. In the STM image, there are big clusters of molecules on top of smaller unordered molecules (Fig. 3.11 a)). The apparent height of those clusters ranges between 5 Å and 10 Å. The sublimation of [Eu(tta)$_3$(bpy)] on Ag(111) at 185 °C for 10 s resulted in a coverage above 1 ML with a large scale lattice formation and bigger agglomerates on top (Fig. 3.11 b)). This self-assembly process has a similar characteristic to what was observed on samples of [Eu(btfa)$_3$(bpy)] after sublimation at 150 °C. A close-up STM topography image of the lattice is shown in Fig. 3.11 c). The unit cell as indicated by the unit cell vectors in red is similar to the unit cell of the lattice on the [Eu(btfa)$_3$(bpy)] sample sublimed at 150 °C. The former has a size of 1.15 nm^2 while the latter has a size of 1.2 nm^2 with two molecules per unit cell each. The different appearances of the lattices can be attributed to the different scan parameters and tip configurations.

The sublimation of [Eu(btfa)$_3$(bpy)] on Ag(111) at a crucible temperature of 185 °C for 1 min resulted in a homogeneous coverage close to 1 ML (Fig. 3.12 a)). In most areas, there is a short scale order of molecules aligning laterally. Furthermore, there are some domains of lattice formation. A close-up STM topography image of this lattice is shown in Fig. 3.12 b). The unit cell size is 3.73 nm^2 for one entity per unit cell and therefore bigger than the unit cells of [Eu(btfa)$_3$(bpy)] after sublimation at 150 °C and of [Eu(tta)$_3$(bpy)] after sublimation at 185 °C. It is difficult to determine whether the objects forming the lattice consist of single molecules or clusters but a direct comparison with the [Eu(btfa)$_3$(bpy)] sample sublimed at 150 °C (Fig. 3.9 c)) emphasizes the difference in shape and size.

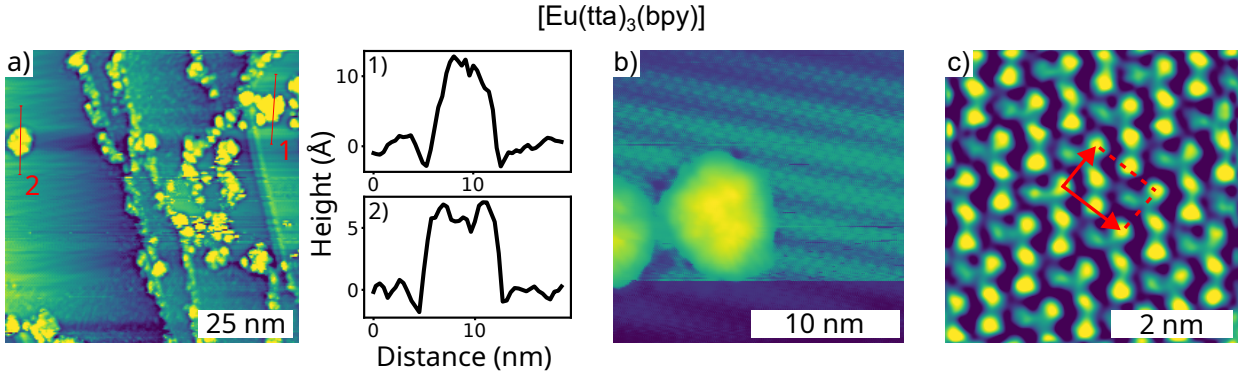

Figure 3.11: STM topography of $[Eu(tta)_3(bpy)]$ complexes and ligands on Au(111) and Ag(111) after sublimation at 185 °C. a) STM topography of larger clusters of molecules on the Au(111) surface and on top of unordered ligands after sublimation at 185 °C with cross-sections. (2.0 V, 10 pA). b) Overview of above ML amount of ligands forming a lattice on Ag(111) with agglomerates on top. (2.0 V, 10 pA). c) Close-up view of lattice formation on Ag(111) with unit cell indicated by red arrows. The unit cell size is 1.15 nm^2. (2.0 V, 1 pA).

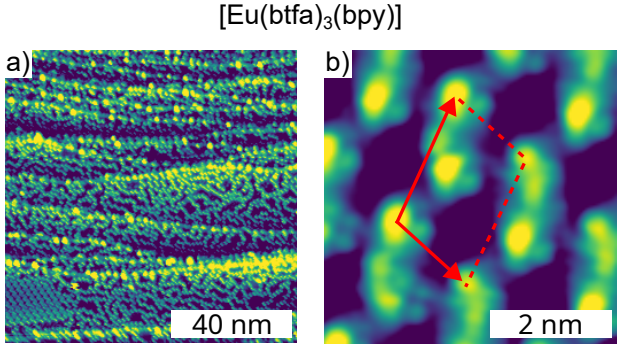

Figure 3.12: STM topography of $[Eu(btfa)_3(bpy)]$ complexes and ligands on Ag(111) after sublimation at 185 °C. a) Overview of ligands with coverage close to 1 ML with some lattice formation. (2.0 V, 10 pA). b) Close-up view of lattice formation with unit cell indicated by red arrows. The unit cell size is 3.73 nm^2. (2.0 V, 10 pA).

3.3.3 Sublimation of $[Eu(tta)_3(bpy)]$ and $[Eu(btfa)_3(bpy)]$ at 185 °C after purification

On the samples of $[Eu(btfa)_3(bpy)]$ and $[Eu(tta)_3(bpy)]$ sublimed at intermediate temperatures, small molecules showing strong self-assembly behavior are present, that can be identified as ligands, i.e. fragments of the Eu^{3+} complexes. On the samples sublimed at 185 °C, these ligands are still present. On the $[Eu(tta)_3(bpy)]$ samples with coverage above 1 ML they form a base layer, sometimes unordered, sometimes as a lattice, in both cases with larger agglomerates on top. On the $[Eu(btfa)_3(bpy)]$ sample with coverage close to 1 ML, they show short scale order and highly ordered domains. Adding the quartz crystal microbalance and monitoring the deposition rate revealed the importance of purifying the material in the crucible by keeping it at intermediate temperatures for several hours to get rid of any contaminations and fragments, as will be discussed in the next paragraph.

The base layer of ligands on the sample can be avoided, when the material in the crucible is kept at 150 °C for $\sim$ 10 h. While subliming at this intermediate temperature was also successfully used for preparing samples that showed a strong Eu^{3+} PL signal (see section 3.6.1) which proves the presence of Eu^{3+} complexes in the film, there are mostly ligands sublimed as is evident from the STM topography images. Subliming the ligands against the shutter of the evaporator purifies the material which allows to prepare cleaner samples when the sublimation temperature of the complexes is chosen higher around 185 °C. Fig. 3.13 a) shows a sample of $[Eu(tta)_3(bpy)]$ prepared after keeping the crucible at 150 °C for about 10 h to get rid of fragments of the complexes. $[Eu(tta)_3(bpy)]$ was then sublimed at 185 °C for 10 s onto Ag(111) at room temperature. There is no base layer of ligands and the molecules are distributed in flat islands with a height of $\sim$ 3 Å. Subliming $[Eu(tta)_3(bpy)]$ onto Au(111) at 185 °C for 15 s after the crucible was kept at 150 °C for $\sim$ 10 h results in smaller molecules evenly distributed on the surface (Fig. 3.13 b)). Their apparent height as shown in the close-up view with cross-sections (Fig. 3.13 c)) is slightly larger than the apparent height of the single ligand molecules.

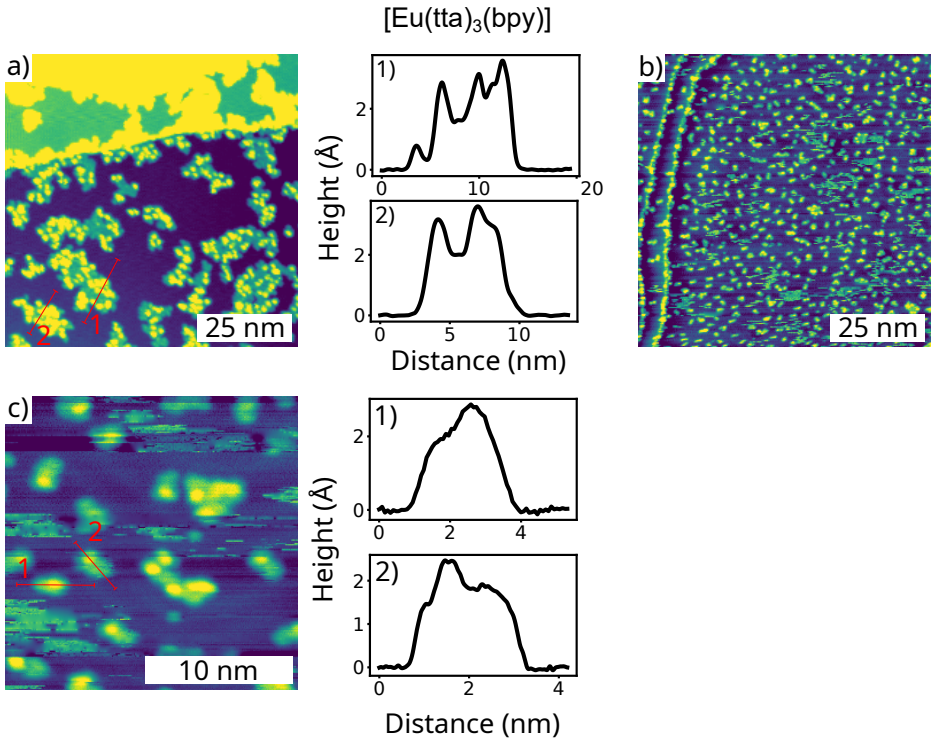

Figure 3.13: STM topography of $[Eu(tta)_3(bpy)]$ complexes and ligands on Au(111) and Ag(111) after sublimation at 185 °C and degassing the crucible at 150 °C for ∼ 10 h. a) Molecules on Ag(111) at submonolayer coverage with cross-sections. (2.0 V, 10 pA). b) Molecules on Au(111) at submonolayer coverage. (2.0 V, 1 pA). c) Close-up view of molecules on Au(111) with cross-sections. (2.0 V, 1 pA).

3.3.4 Vacuum spray deposition of $[Eu(tta)_3(H_2O)_2]$

$[Eu(tta)_3(H_2O)_2]$ was deposited onto clean Au(111) via vacuum spray deposition from a dichloromethane solution with a concentration of 1 mg/ml with subsequent annealing to approximately 100 °C for 2 min in UHV conditions. Spray deposition was preferred over sublimation, because of the reported cleaving of H_2O groups in $[Dy(tta)_3(H_2O)_2]$ due to heating in UHV conditions [143]. The spray deposition leads to a sub monolayer coverage of molecules aligning in highly ordered islands, as well as unordered agglomerates of molecules (Fig. 3.14 a). The islands follow the herringbone reconstruction, preferably nucleating at the pinched elbows where the fcc domain is maximized, perpendicular to the mirror axis. The agglomerates nucleate at the bulged elbows of the herringbone reconstruction. The preferential nucleation of molecules on different domains of the herringbone reconstruction is well documented in literature [144–148]. The islands have an apparent height of 1.5 Å(Fig. 3.14 b). Since spray deposition leads to an inhomogeneous distribution of molecules on the sample, a different nucleation characteristic can be found on another spot on the sample (Fig. 3.14 c). Here, the molecules do not form islands and the template effect by the herringbone reconstruction is more pronounced. Some molecules

align in chains with short range order (Fig. 3.14 d) with a periodicity of 1.22 nm (Fig. 3.14 e). This is different to the periodicity of 0.65 nm of the molecular chains observed for [Eu(tta)$_3$(bpy)]. The cross-section of a single molecule was fitted with a double gaussian and the center to center distance thus determined to 0.49 nm (Fig. 3.14 f). The comparison with [Eu(btfa)$_3$(bpy)] and [Eu(tta)$_3$(bpy)] suggests that the highly ordered islands and the chains with short range order on the [Eu(tta)$_3$(H$_2$O)$_2$] sample consist of ligands while the bigger agglomerates might be composed of intact complexes. The differences in the center to center distances on single molecules between all three complexes and the difference in the periodicity of molecular chains on [Eu(tta)$_3$(bpy)] and [Eu(tta)$_3$(H$_2$O)$_2$] samples cannot be explained entirely. It can be speculated that the isolated molecule on the [Eu(tta)$_3$(bpy)] and [Eu(tta)$_3$(H$_2$O)$_2$] sample is a tta ligand, while on the [Eu(btfa)$_3$(bpy)] sample it might be a btfa or bpy ligand. This could explain the similar values of the center to center distance on the [Eu(tta)$_3$(bpy)] and [Eu(tta)$_3$(H$_2$O)$_2$] samples of 0.67 and 0.49 nm and the larger value of 1.03 nm on the [Eu(btfa)$_3$(bpy)] sample. However, all three ligands, tta, btfa and bpy are similar in size and the center to center distances were measured with different tunneling parameters. The difference in the periodicity of molecular chains on the [Eu(tta)$_3$(bpy)] and [Eu(tta)$_3$(H$_2$O)$_2$] samples might be due to different packing perhaps influenced by the different sample preparation procedures.

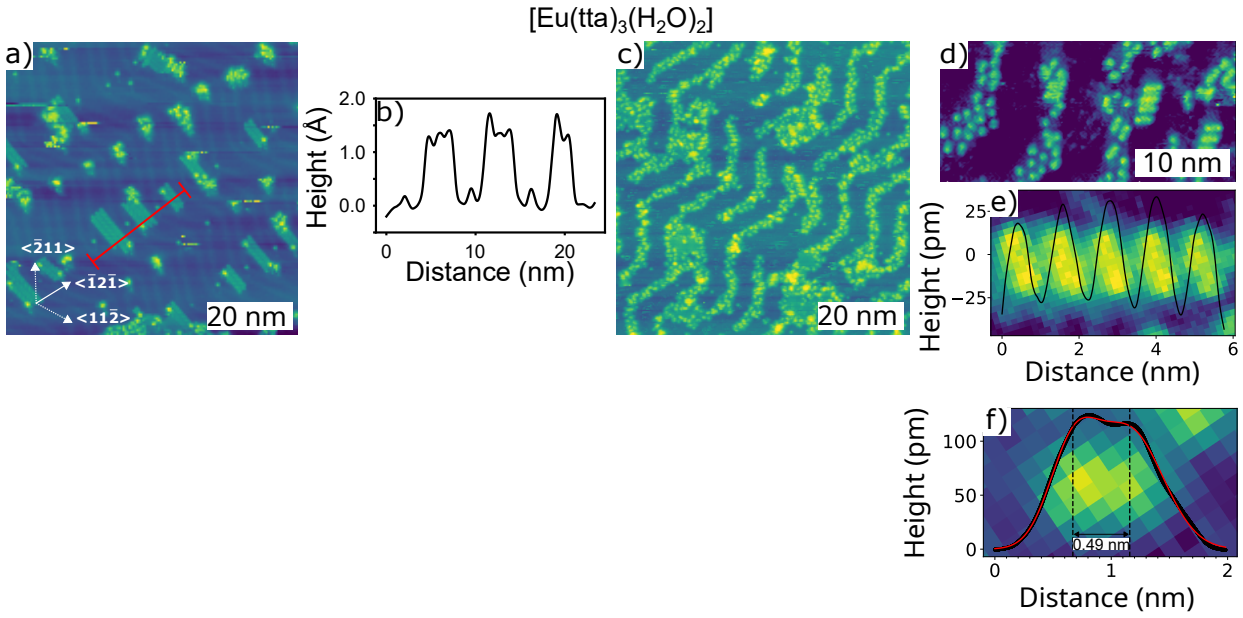

Figure 3.14: STM topography of the self-assembly of ligands and Eu^{3+} complexes on [Eu(tta)$_3$(H$_2$O)$_2$] samples. a) Molecules adsorbed on Au(111) at sub-monolayer coverage. Molecules form highly ordered islands and clusters. (-2.6 V, 2 pA). b) Cross-sections of 3 islands. c) Molecules following the herringbone reconstruction on a less ordered location on the sample. (1.0 V, 4 pA). d) Close-up view of molecules aligning in short chains. (2.0 V, 4 pA). e) Cross-section of a chain of molecules. (2.7 V, 4 pA). f) Cross-section across an individual molecule. (2.0 V, 4 pA.). Adapted from [52].

3.3.5 Summary and discussion

The STM data shown here demonstrate the delicateness of preparing clean Eu^{3+} samples. It is shown that fragments can easily be confused with intact complexes in STM images. While the origin of those fragments cannot be determined with certainty, they are believed to be present already in the molecular material before sublimation or arise from fragmentation by heating [143], which explains why extended degassing at intermediate temperatures results in cleaner samples and a conclusive quartz crystal microbalance signal. The comparison of $[Eu(tta)_3(bpy)]$ sublimed onto Au(111) and onto Ag(111) suggests that significant fragmentation might also arise from the interaction with the substrate [140]. It is not possible to determine those fragments with certainty. While the lattice formation observed on samples of $[Eu(tta)_3(bpy)]$ and $[Eu(btfa)_3(bpy)]$ is similar to the self-assembly reported for bipyridine, a ligand present in both complexes, chains of molecules with short range order were found on sample of $[Eu(tta)_3(bpy)]$, $[Eu(btfa)_3(bpy)]$ and $[Eu(tta)_3(H_2O)_2]$. $[Eu(tta)_3(H_2O)_2]$ lacks bipyridine but contains tta, a ligand it shares with $[Eu(tta)_3(bpy)]$ and which is similar in structure to btfa contained in $[Eu(btfa)_3(bpy)]$. This suggests the presence of not only fragmented bipyridine but also of tta and btfa ligands on the sample. These molecules might show similar self-assembly driven by the π-π interaction of their phenyl moieties.

To obtain clean samples without a majority of molecules being fragments, sufficient degassing at intermediate temperatures is necessary, as was shown by STM images of $[Eu(btfa)_3(bpy)]$ and $[Eu(tta)_3(bpy)]$ samples prepared by subliming the material at temperatures below 185 °C and at 185 °C without extended degassing, resulting in a high coverage of ligands on the sample exhibiting strong self-assembly. This base layer of ligands is no longer present, when the material was purified as demonstrated by the STM images of a $[Eu(tta)_3(bpy)]$ sample prepared at 185 °C after degassing the material inside the crucible.

A thorough control of the deposition process by monitoring the pressure, deposition rate and changes of the sublimed material, supplemented by comparison with literature is crucial to prepare clean samples with a controlled thickness. The sample preparation process as established in this work therefore allows investigating the opto-electronic properties of Ln complexes.

3.4 STM topography of platform complexes

All Eu^{3+} complexes based on betadiketonates in this thesis consist of individual ligands being attached to the metal ion in the center thus forming a mononuclear coordination complex. Since the orientation of the ligands with respect to the metal core and to one another is not fixed, there is a high freedom of movement. The complexes are therefore free to distort in different ways, introducing an element of randomness. Furthermore, the C1 symmetry of betadiketonate based Eu^{3+} complexes makes identifying their adsorption behavior with STM topography challenging. In comparison, when Ln ions are embedded in a platform scaffold such as the trensal chelator, [113, 136, 149] the complex is more rigid and has a distinct shape. Furthermore, the C3 symmetric trensal framework provides a controlled

symmetry for the Eu^{3+} center reducing line broadening. Next to [Eu(trensal)], variations with elongated tripodal platforms ([Eu(trensal-Ph-SMe)] and [Eu(trensal-O-Bn)]) were investigated. The technique of placing single molecule chromophores on tripodal scaffolds was successfully used to create self-decoupling complexes in the past [60]. The structural and opto-electronic properties of trensal based complexes differ from the properties of betadiketonate complexes which opens the possibility for an interesting comparison, which promises to deepen our current understanding. This comparison is supplemented by a platform Ln complex featuring Tb^{3+} as the metal center. For this reason, the characteristics of trensal based complexes in STM topography are shown in this section.

3.4.1 Sublimation of [Eu(trensal)]

[Eu(trensal)] turned out to be sublimable at 270 °C. The sublimation temperature was found by step-wise heating the crucible of the evaporator and monitoring the deposition rate with the quartz crystal microbalance. While this method is not entirely reliable for determining the right temperature for sublimation as discussed in section 3.2.2 and 3.3, it worked for Eu(trensal). The sublimation of Eu(trensal) complexes at 270 °C resulted in samples exhibiting a PL signal different to those of betadiketonate based complexes (see section 3.6.5). This is taken as an indication that sublimation at this temperature results at least in part in the deposition of itact complexes. Eu(trensal) was the only trensal based complex with a conclusive deposition rate in the quartz crystal microbalance.

Eu(trensal) was sublimed onto clean Au(111) at 270 °C for 10 s. This resulted in a sub monolayer coverage of homogeneously distributed molecules (Fig. 3.15 a)). The streaks in the STM topography image indicate highly mobile molecules moving across the surface even at 4.5 K. A close-up STM image is shown in Fig. 3.15 b) together with a cross-section. The structure of the molecule is shown in Fig, 3.15 c). While it is not possible to conclude the shape of intact [Eu(trensal)] complexes on the surface from these STM images, the complex is expected to adsorb with its C3 axis perpendicular to the surface [150] which would lead to a small apparent height. This is in agreement with the height of around 2 Å as determined with the cross-section.

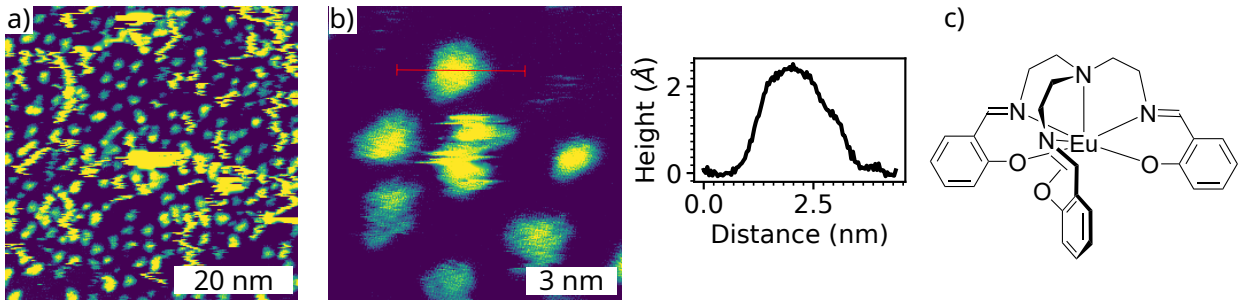

Figure 3.15: STM topography of [Eu(trensal) on Au(111). a) Overview of molecules on Au(111). (2.0 V, 1 pA). b) Close-up view of molecules with cross-section. (2.0 V, 1 pA). c) Molecular structure of [Eu(trensal)].

3.4.2 Sublimation of [Eu(trensal-O-Bn)]

[Eu(trensal-O-Bn)] is a promising candidate for a self-decoupling trensal based complex. The Eu^{3+} ion is positioned on a tripodal platform. The three feet of this platform consist of phenyl moieties that can potentially lay flat on the substrate surface. However, establishing a reliable and finely controllable deposition method for this complex was not possible within the scope of this thesis. For this reason, and due to the fact, that the PL signal of the trensal based complexes was quite low in comparison to the betadiketonate complexes, experiments focusing on the latter were favored.

[Eu(trensal-O-Bn)] was deposited on Ag(111) by sublimation at a crucible temperature of 300 °C. The temperature for sublimation was estimated to be slightly higher than for [Eu(trensal)]. The deposition rate monitored with the quartz crystal microbalance was not conclusive. Sublimation at 300 °C for 20 s resulted in a coverage close to 1 ML. The molecules cluster into larger agglomerates (Fig. 3.16 a)). It is not possible to determine the exact shape or orientation of the molecules on this sample (Fig. 3.16 b)). The molecular structure of the complex is shown in Fig. 3.16 c).

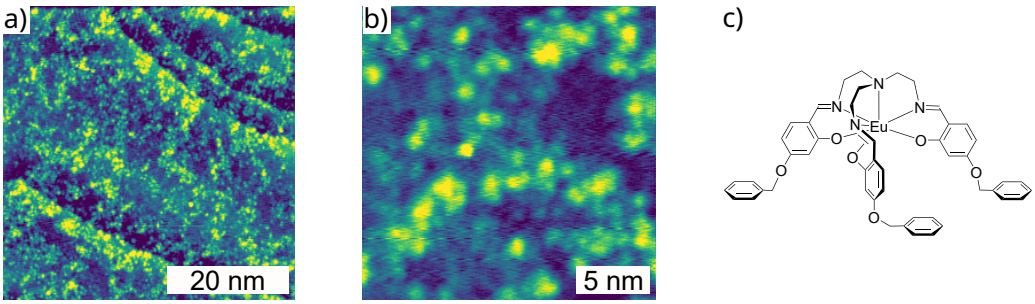

Figure 3.16: STM topography of [Eu(trensal-O-Bn)] on Ag(111). a) Overview of molecules at a coverage close to 1 ML adsorbed on the Ag(111) surface. (2.0 V, 10 pA). b) Close-up view of clusters of molecules. (2.0 V, 4 pA). c) Molecular structure of [Eu(trensal-O-Bn)].

3.4.3 Vacuum spray deposition of [Eu(trensal-Ph-SMe)]

[Eu(trensal-Ph-SMe)] is another variant of a Eu^{3+} complex featuring the trensal structure. The feet of the tripodal platform feature sulfur, which is expected to act as an anchor, increasing stability on the substrate.

[Eu(trensal-Ph-SMe)] was deposited onto clean Au(111) via vacuum spray deposition from a dichloromethane solution with a concentration of 1 mg/ml followed by annealing with 5 W (<200 °C) for 10 min. This resulted in a sub monolayer coverage as shown in Fig. 3.17 a). The surface is covered with flat islands of molecules as is apparent from the cross-section. Next to those islands, smaller aggregates are present. Some of those aggregates have a C3 symmetry which is expected from the structure of [Eu(trensal-Ph-SMe)] that is shown in Fig. 3.17 d). However, in the close-up STM topography images (Fig. 3.17 b)) there are two aggregates with three-fold symmetry but different chirality adsorbed on the surface. Furthermore, in the same image an aggregate consisting of three oblong shapes, laterally aligned can be seen. It is therefore reasonable that these aggregates consist of three oblong molecules that sometimes cluster into triangular shapes to maximize their interaction but that can also align laterally. A cross-section of a single aggregate (Fig. 3.17 c)) confirms that these are not intact complexes which would be expected to be taller. The apparent height of approximately 1.3 Å suggests that these aggregates consist of the legs of [Eu(trensal-Ph-SMe)] with the phenyl groups adsorbed flat on the surface.

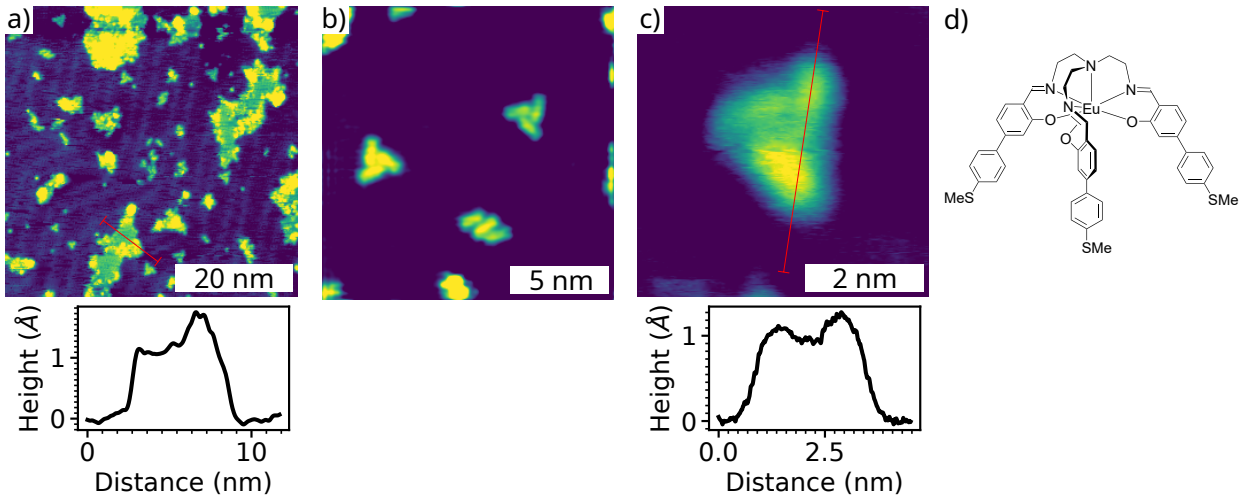

Figure 3.17: STM topography of [Eu(trensal-Ph-SMe)] on Au(111). a) Overview of islands and smaller molecules of [Eu(trensal-Ph-SMe)] with cross-section of an island. (2.0 V, 4 pA). b) Close-up view of two molecules with three fold symmetry but different chirality. (2.0 V, 4 pA). c) Close-up view of a single molecule with three fold symmetry and height profile. (2.0 V, 4 pA). d) Molecular structure of [Eu(trensal-Ph-SMe)].

3.4.4 Vacuum spray deposition of [Tb(Tacn)]

The [Tb(TACN)] complex is a representative of the TACN structure featuring Tb instead of Eu as the metal center. Similar to Eu^{3+}, the main transitions of Tb^{3+} are within the 4f shell, resulting in sharp and long-lived transitions [151].

[Tb(Tacn)] was deposited onto Au(111) by vacuum spray deposition from a solution of 1 mg/ml in highly purified water followed by annealing with 5.8 W ($\sim$ 250-300 °C). This resulted in a sub monolayer coverage. There are larger islands of molecules present on the sample as well as smaller agglomerates. The islands roughly follow the herringbone reconstruction of the Au(111) surface, while smaller agglomerates decorate the elbows (Fig. 3.18 a)). The apparent height of the islands is determined with two cross-sections to be in the range of 2.5-2.8 Å. It is evident from the shape of the cross-sections that the islands are not entirely flat. The reason for this becomes more apparent in the close-up image (Fig. 3.18 d)). Some areas of the islands appear higher which could be due to a second layer of molecules or taller molecules. The elbows of the herringbone reconstruction are decorated by smaller molecules some of which are identical in shape and size as shown in Fig. 3.18 e). While the appearance of these molecules is the same, their orientation is different which rules out an effect caused by the tip. Two close-up views of these molecules reveal the intra-molecular structure at different bias voltages. At a positive voltage of 2 V (Fig. 3.18 b)) the structure appears five fold symmetric, although 3 lobes are slightly brighter than the other two. At a negative bias voltage of -2 V (Fig. 3.18 c)) the molecule appears three fold symmetric with one lobe brighter than the other two. The apparent height of these individual molecules is

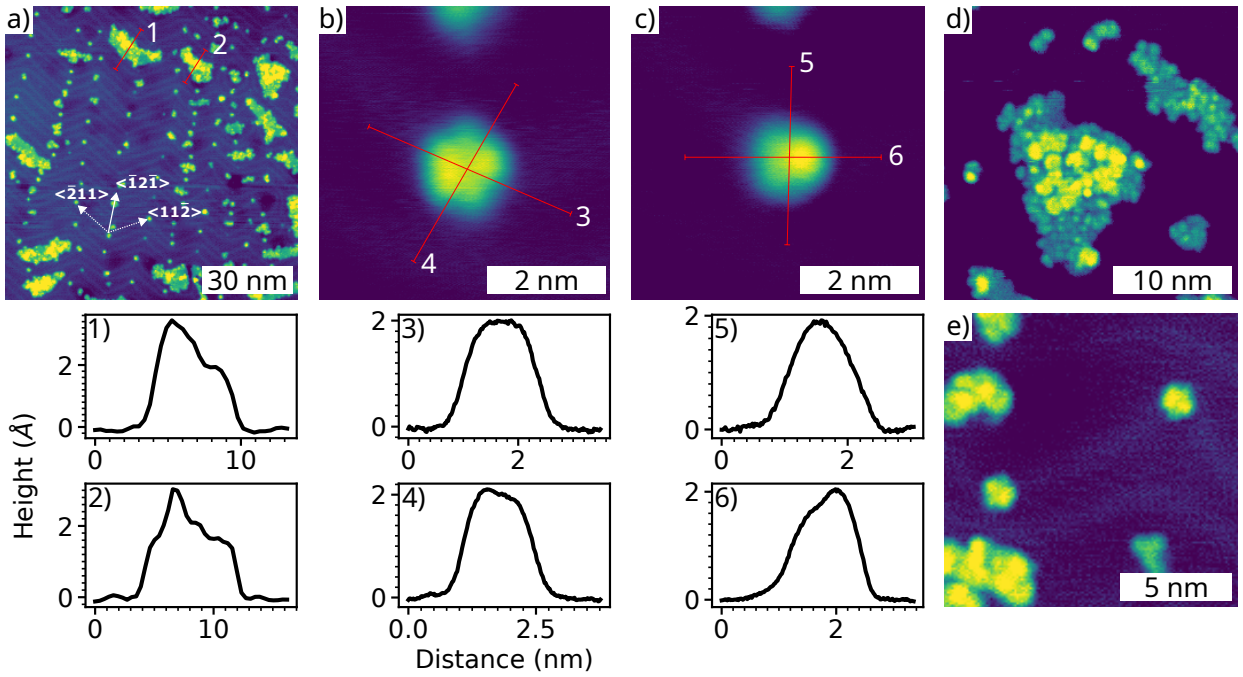

Figure 3.18: STM topography of [Tb(TACN)] on Au(111). a) Overview of molecules at a coverage below 1 ML with larger islands and smaller agglomerates following the herringbone reconstruction with cross-section of the islands. (2.0 V, 1 pA). b) Close-up view of a single molecule with cross-sections scanned at 2.0 V, 10 pA. c) Close-up view of a single molecule with cross-sections scanned at -2.0 V, 10 pA. d) Close-up view of an island. (2.0 V, 1 pA). e) Close-up view of two single molecules with same shape but different orientation. (2.0 V, 1 pA).

around 2.1 Å. It is reasonable to assume that these single molecules with uniform shape are intact [Tb(TACN)] complexes.

3.4.5 Summary and discussion

This section provided an overview of the sample preparation and STM topography of Ln platform complexes. As discussed, finding the right temperature for sublimation was not possible for all complexes, because the deposition rate as checked with the quartz crystal microbalance was not always conclusive. A more in depth study on the sublimation procedure including degassing is required to establish a reliable deposition method. For this reason, vacuum spray deposition was preferred for most complexes which is sufficient for preparing samples for STM topography.

STM topography images of [Eu(trensal)], [Eu(trensal-O-Bn)], [Eu(trensal-Ph-SMe)] and [Tb(Tacn)] were shown. Identifying intact complexes and drawing conclusions on their orientation is just as challenging as for betadiketonate complexes, despite the more characteristic shape of the trensal complexes.

3.5 Towards electro-luminescence

This thesis aims to elucidate the limitations of luminescence from Ln complexes adsorbed on a metal surface. The excitation of luminescence by tunneling electrons which is a form of EL, is the ultimate experiment, when working with single light sensitive molecules inside the tunneling junction. EL was tried with different Ln complexes both on the bare substrate and on insulating layers, but never showed conclusive signs of light emission from Ln complexes. A systematic EL study could therefore not be conducted in favor of PL experiments that allow to investigate different energy transfer mechanisms also relevant for EL. This section will provide an overview of the steps taken towards EL from Ln complexes.

3.5.1 Plasmon spectrum

STML from plasmons has been studied extensively with this STM set-up in the past [58, 59]. In the scope of this thesis, it was used to determine the quality of the mirror tips and verify the working principle of collecting light from the tunneling junction. Many factors can influence the light collection. Molecules adsorbed on the tip change its density of states which can quench luminescence from plasmons. Furthermore, a significant voltage drop can occur in a dirty tip, i.e. when many molecules are adsorbed on it. This voltage is then not available for plasmon excitation. However, even without contamination, tips have different light collection efficiencies due to imperfections in the manufacturing process. The mirror tip therefore needs to be checked with a microscope before installing in the STM. Typical problems are for example: a missing tip apex, a partially or fully detached parabolic mirror, or shavings of the material standing out further than the apex. Even when a tip is working nicely after installation, it will eventually break due to its fragility. It is therefore necessary to check the light collection of a tip regularly. This can be done by exciting plasmons on a clean substrate and evaluating the yield and shape of their spectrum. With a single electron process, the plasmon resonance can only be excited up to energies corresponding to the energy provided by the electrons. If both tip and sample are conducting, the cut off energy of the spectra corresponds to the applied bias voltage (see Fig. 3.19). Close to the absorption edge of Au, the cut off stops increasing with the bias voltage, because the light cannot escape the junction anymore.

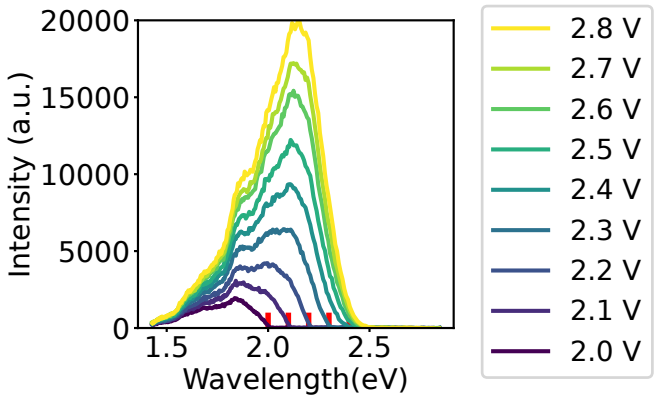

Figure 3.19: Plasmon spectra excited by tunneling electrons measured inside the STM cavity with a clean mirror tip on Au(111) at 4.5 K for different bias voltages. The dark background was subtracted. The red vertical lines indicate bias voltages in the range of 2.0 - 2.4 V. The emission edge at $\sim$ 500 nm corresponds to the onset of absorption in gold. Tunneling current: 130 pA.

3.5.2 NaCl islands as insulating layers

The interaction between light emitting molecules adsorbed on a surface and the substrate potentially reduces luminescence radiating into the far field due to plasmon excitation [47, 48], image charge oscillations [46] the excitation of electron-hole pairs [45], interband transitions and charge transfer [40]. Depositing molecules ontop of a thin dielectric material on the substrate reduces the latter while still allowing sufficient tunneling for STM. NaCl islands are commonly used as insulators on metal substrates [40, 61, 66–68, 152] and have e.g. been shown to reduce the work function of Ag(100) [153] and shifting the surface state of Au(111) [154]. However, decreasing the interaction of molecule and surface enhances the diffusion of the molecule making them more mobile and thus more unstable to scan with STM. While depositing molecules on a layer of NaCl is a well known method which is also comparably straight-forward, some care should be taken when checking the growth with STM. NaCL islands can most easily be distinguished from the bare substrate surface when the edge of an island is found. The cuboid shape of the NaCl lattice leads to rectangular edges that are otherwise not present on threefold symmetric Au(111). However, when no edge is found, it can be difficult to determine whether the coverage is too high or too low. In this case STS can give an indication, or, if atomic resolution can be achieved, the NaCl lattice can be distinguished from the Au(111) surface.

To grow NaCl islands on Au(111), NaCl is sublimed from a *Kentax 3 cell* evaporator at a temperature of around 570 °C for 4-8 min. The sample is kept at room temperature during sublimation and post-annealed afterward with 5 W ($<$ 200 °C) for approximately 10 min. Post annealing is required to grow flat islands of several ML and reduce defects. The Na^+ and the Cl^- ions form a FCC lattice with a distance between atoms of the same type of around 400 pm [155, 156]. NaCl islands of the size of several 100 nm with an apparent height of 3 ML are displayed in Fig. 3.20 a). The apparent height as determined by cross-section

measurements (Fig. 3.20 c) 1 and 3)) of the islands varies in STM topography depending on the scan parameters. On this sample the apparent height of the islands is around 400 pm at 1.0 V, 10 pA, which is in agreement with literature [154]. In some islands patches of NaCl can be missing (Fig. 3.20 c) 4). The herringbone reconstruction of the Au(111) surface is visible underneath 1 ML NaCl (Fig. 3.20 b)).

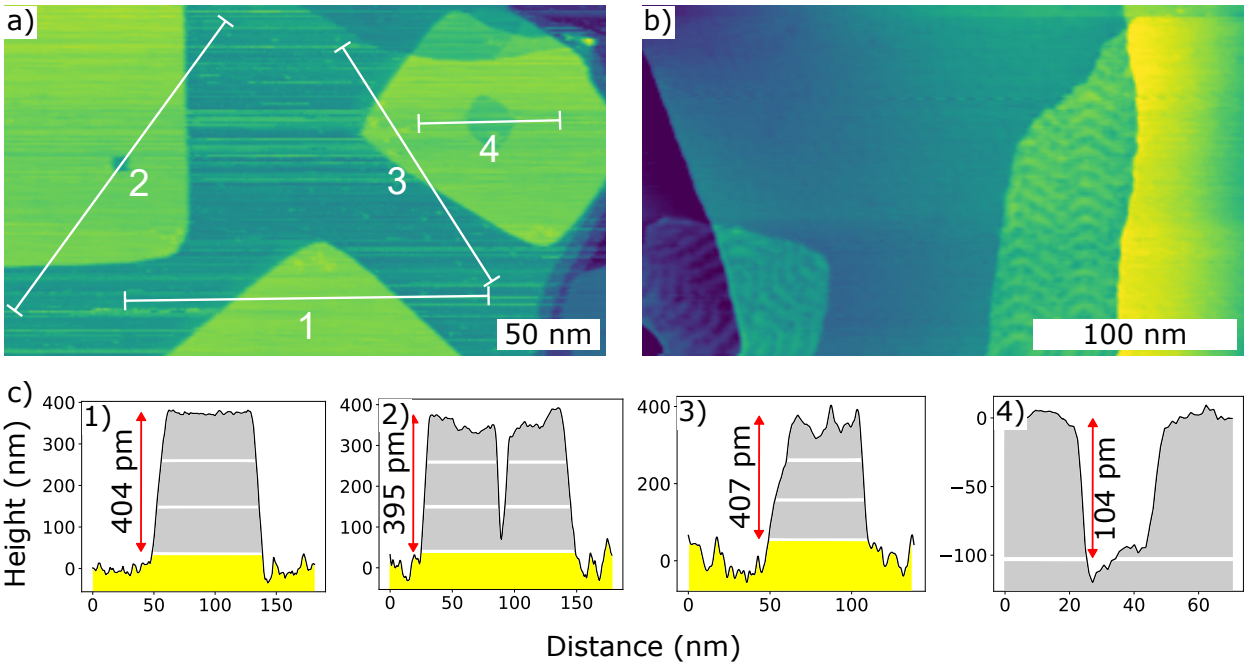

Figure 3.20: a) STM topography of Nacl islands on Au(111) with positions of cross-sections (1.0 V, 10 pA). b) STM topography of herringbone reconstruction underneath 1 ML NaCl islands. (1.0 V, 100 pA). c) Cross-sections of NaCl islands as indicated in a).

For depositing complexes on top of the NaCl islands, cooling the sample is advantageous for decreasing diffusion. Pumping liquid nitrogen through the manipulator stage via a capillary results in temperatures between -70 to -100 °C. In some cases, this was found not sufficient to prevent the complexes from diffusing off the NaCl islands. For this reason, several ML of complexes are deposited on a sacrifice sample, while the target sample with NaCl islands on it is kept at LN_2-temperatures in the pre-cooling stage that is attached to the LN_2 cryostat. The sacrifice sample is then positioned above the target sample with the manipulator and heated up to sublime the complexes. This method is referred to as indirect transfer. However, even with this method, molecules are not necessarily well adsorbed on the island nor the surface. Manipulation of the complexes while scanning is inevitable, especially when choosing a higher voltage and set-point.

Fig. 3.21 shows consecutive STM topography scans of the same spot on the sample. This sample was prepared using the indirect transfer method. $[Eu(tta)_3(bpy)]$ complexes were

sublimed onto the sacrifice sample at a crucible temperature of 160 °C for 30 min. The sacrifice sample was then heated shortly (<1 min) to 500 °C. In the first image (Fig. 3.21 a)) there are practically no molecules visible on the NaCl island nor on the Au(111) surface. During the scan process, the molecules are moved around on the sample but also interact with the tip. Molecules attaching and detaching from the tip change its electronic configuration thus influencing the STM image. In Fig. 3.21 b) the molecules start to appear. Streaks indicate highly mobile molecules being dragged along by the STM tip. On the NaCl islands some molecules can be distinguished. In Fig. 3.21 c) the shape of the molecules becomes less blurred indicating a more stable configuration. The empty appearing area below the island is due to a tip change. Eventually, (Fig. 3.21 d)) the molecules can be clearly distinguished. The stability of the STM image improved over time because the molecules were moved into more favorable positions by the scanning process both on the sample and on the tip.

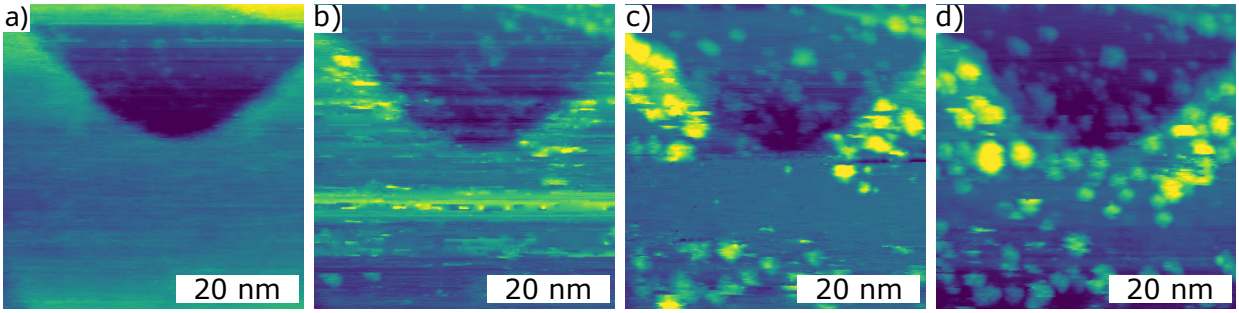

Figure 3.21: Consecutive STM topography scans of $[Eu(tta)_3(bpy)]$ molecules on Au(111) with a NaCl island. (STM parameters: a) 2 V, 5 pA, b) -d) 3 V, 5 pA). The molecules are moved into stable positions by the scan process.

Fig. 3.22 provides and overview of the characteristics of molecules adsorbed on NaCl islands. $[Eu(tta)_3(bpy)]$ complexes were deposited on NaCl islands on a Au(111) substrate. The complexes were sublimed directly on the sample at a crucible temperature of 185 °C for 10 s. The sample was cooled with LN_2 to -75 °C. This resulted in molecules adsorbed on the islands in a coverage below 1 ML (Fig. 3.22 a)). The molecules have no distinct shape and appear blurred on the islands indicating their high mobility. Fig. 3.22 b) shows $[Eu(tta)_3(bpy)]$ complexes sublimed onto NaCl islands on a Au(111) substrate using the indirect transfer method. The sacrifice sample was prepared by evaporating $[Eu(tta)_3(bpy)]$ complexes at 160 °C for 30 min. The molecules were transferred onto the target sample at LN_2 temperature by heating the sacrifice sample shortly to 500 °C. The molecules are well adsorbed on the NaCl island at the right hand side of the image. The molecules on the NaCl layer appear larger and higher than the molecules on the Au(111) surface in the STM topography. This effect becomes even more apparent in Fig. 3.22 c). Here, $[Eu(btfa)_3(bpy)]$ complexes were deposited onto NaCl islands on a Ag(111) substrate via indirect transfer. $[Eu(btfa)_3(bpy)]$ complexes were sublimed onto the sacrifice sample at a temperature of 155 °C for 30 min. Transferring the complexes onto the target sample resulted in a coverage below 1 ML. Individual molecules are adsorbed in a stable manner on the Ag(111) surface and on the NaCl island. The apparent height is determined with cross-section measurements. On the Ag(111) surface the molecules have an apparent height

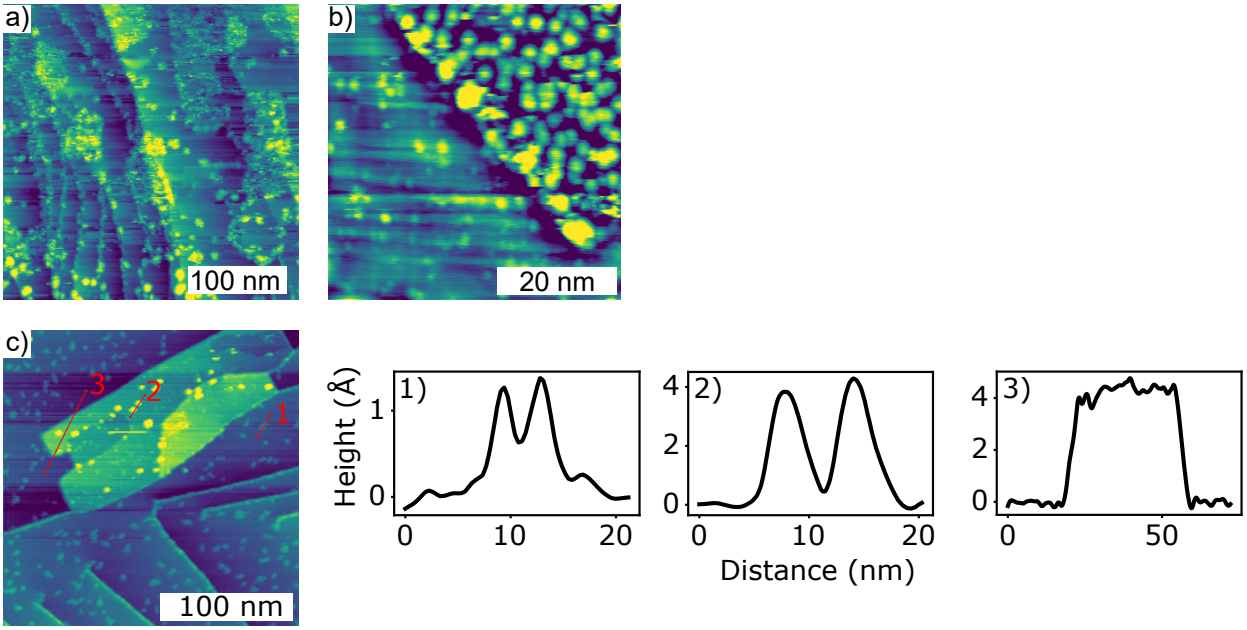

Figure 3.22: Overview of different characteristics of molecules adsorbed on NaCl islands. a) STM topography of $[Eu(tta)_3(bpy)]$ complexes deposited on NaCl islands on a Au(111) substrate via direct transfer. (2.0 V, 10 pA). b) STM topography of $[Eu(tta)_3(bpy)]$ complexes deposited on NaCl islands on a Au(111) substrate via indirect transfer. (3.7 V, 14 pA). c) STM topography of $[Eu(btfa)_3(bpy)]$ complexes deposited on NaCl islands on a Ag(111) substrate via indirect transfer with cross-sections. (1.63 V, 10 pA).

above 1 Å while it is approximately 4 Å on NaCl. This is due to the decoupling of molecular orbitals from the substrate by the NaCl layer. The height of the NaCl island is around 4 Å which translates to 3 ML [154].

3.5.3 Electro-luminescence

The lifetime of Eu^{3+} in powder form is in the range of several hundred µs which corresponds to a decay rate in the order of 1 kHz. In the STM junction the probability for the interaction between matter and light is increased by the Purcell effect by about a factor of 1000. Assuming a detection efficiency of 10 % this leads to photons being emitted at a frequency of 100 kHz. Incorporating the Eu^{3+} ion within a framework of ligands utilizing the antenna effect allows to separate the excitation from the decay process. This circumvents the possibility of destroying the excited state of Eu^{3+} by charge injection into Eu^{3+} and thus does not limit the injection rate of electrons to the decay rate of the emitting Eu^{3+} ion. These advantages over typical organic chromophores where excitation happens via the same two energy levels that are involved in the light emission increase the theoretical upper limit of the rate of radiative decay to the observed lifetime of Eu^{3+} multiplied by the Purcell factor and the detection efficiency ($\sim$ 100 kHz). These considerations highlight the importance of understanding the excitation mechanisms of Eu^{3+} complexes and the energy transfer from

the ligands as limiting factors for EL.

To excite molecules with tunneling electrons, the voltage has to be chosen higher than what is usually sufficient for STM to account for the excitation via inelastic tunneling. In the past, EL of light sensitive molecules was successfully measured with the same set-up [60–62] by applying a bias voltage of up to $\sim$ 3 V and a tunneling current of one to several hundred pA. An integration time of several seconds was then sufficient to obtain a distinct emission spectrum. However, with Eu complexes no distinct emission spectrum was observed even with integration times of several minutes. With low current set-points, the spectra consist mostly of noise while with high set-points, plasmon emission sets in.

EL was tried at least briefly on most prepared samples. $[Eu(tta)_3(bpy)]$ deposited on islands of NaCl ontop of the metal substrate was investigated in most detail. The NaCl layer was expected to decouple the complexes and decrease de-excitation via charge transfer. Furthermore, trensal based platform complexes such as [Eu(trensal)-Ph-SMe] and [Eu(trensal)-Bn-O] were expected to be promising for EL due to their potential to self-decouple from the substrate. However, no EL spectrum corresponded to the sharp emission expected from Eu^{3+} complexes. This section refrains from providing a systematic and thorough study, but provides an overview of the various EL experiments. The spectra shown here are normalized to their maximum peak height, smoothed and the background is subtracted. A mirror tip is used for light collection (see section 3.1.3, Fig. 3.3 set-up C).

$[Eu(tta)_3(bpy)]$ was sublimed for 10 s at a crucible temperature of 185 °C onto Au(111) with NaCl islands on top (Fig. 3.23) (for the sample preparation see section 3.2.2). EL was measured at three different locations as indicated by the red crosses labeled 1), 2) and 3). The tunneling parameters for EL were chosen to 3.0 V and 300 pA. The PL spectrum of a $[Eu(tta)_3(bpy)]$ powder sample is overlaid for comparison. Spectrum 1) is taken on a molecule on the clean Au(111) surface, spectrum 2) is taken on a molecule on top of a NaCl island and spectrum 3) is taken on clean Au(111). There is no significant difference between the three spectra. All three spectra have a main peak around 900 nm and do not correspond to the emission expected from Eu^{3+}. These spectra are unusual since the maximum of the plasmonic emission is usually around 600 nm.

[Eu(trensal)-Ph-SMe] was sublimed onto clean Ag(111) for 8 s with a crucible temperature of 200 °C. Ag(111) was preferred in later experiments over Au(111) due to the lower absorption of the excitation light at 375 nm. It should also be noted that the deposition rate as monitored with the quartz crystal microbalance was not conclusive for [Eu(trensal)-Ph-SMe]. The sample was sparsely covered with molecules and it is not possible to determine if these molecules are intact [Eu(trensal)-Ph-SMe] complexes. EL was measured on a single isolated molecule (Fig. 3.24 a)) and on the same molecule while scanning (Fig. 3.24 b)). The tunneling parameters for EL were 3.5 V and 100 pA. The EL spectra show the typical plasmonic emission at $\sim$ 600 nm. When comparing the plasmonic emission with the overlaid PL spectrum of a [Eu(trensal)-Ph-SMe] powder sample they do not correspond well.

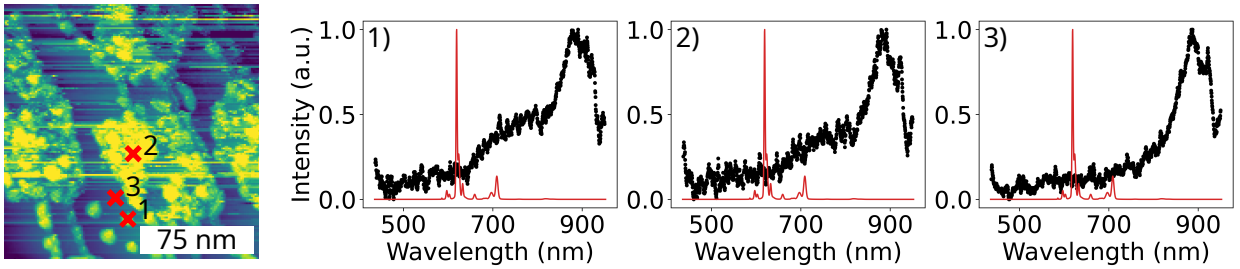

Figure 3.23: STM topography of $[Eu(tta)_3(bpy)]$ complexes sublimed onto a Au(111) substrate with NaCl islands and EL spectra taken on different locations indicated by 1), 2) and 3). PL spectrum of $[Eu(tta)_3(bpy)]$ overlaid in red for comparison. STM topography parameters: 2.0 V, 10 pA. Spectrum 1): molecule on Au(111). Spectrum 2): molecule on NaCl on Au(111) . Spectrum 3): clean Au(111). All spectra were taken with tunneling parameters: 3.0 V, 300 pA.

Furthermore, the spectrum of EL from Eu^{3+} is expected to have emission lines even sharper to PL emission due to the absent ensemble averaging [60].

[Eu(trensal)-Bn-O] was sublimed onto clean Ag(111) for 20 s at a crucible temperature of 300 °C. EL was measured while scanning a molecule with tunneling parameters of 3.5 V and 100 pA and with the STM tip positioned stationary above a molecule with tunneling parameters of 3.5 V and 1 pA. Overlaid in both EL spectra is the PL spectrum of a [Eu(trensal)-Bn-O] powder sample for comparison. Fig. 3.25 a) displays the EL spectrum obtained while scanning a small area as shown in the corresponding STM image. The spectrum consists of emission from plasmons. There is a slight dip in the EL spectrum where the PL emission has its main peak. This dip could arise from the Eu^{3+} complex not being directly excited but still coupling to the plasmon resonance, resulting in a Fano lineshape of the combined emission [157]. Fig. 3.25 b) shows the EL spectrum with the tip stationary at the position indicated by the red cross in the STM image. The spectrum is noisy with a main peak at 900 nm, not corresponding with the Eu^{3+} spectrum.

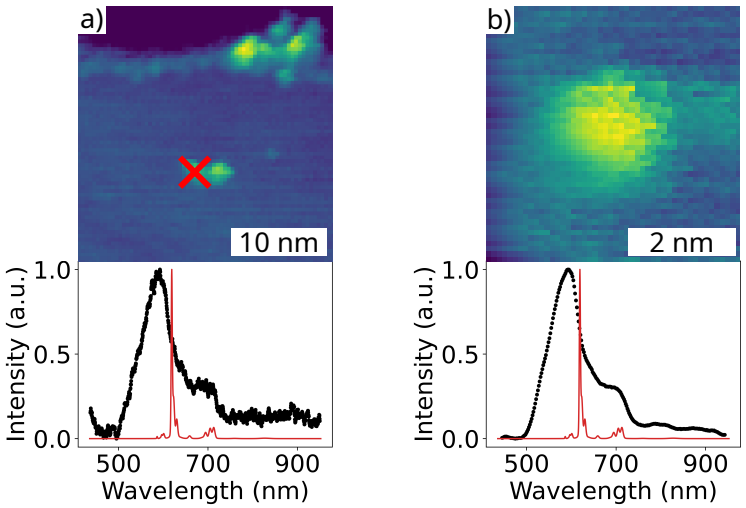

Figure 3.24: STM topography and EL spectra of [Eu(trensal)-Ph-SMe] on Ag(111). PL spectrum of [Eu(trensal)-Ph-SMe] overlaid in red for comparison. a) Molecule on Ag(111) with EL spectrum taken at position indicated by red cross. STM topography parameters: 2.0 V, 300 pA. EL tunneling parameters: 3.5 V, 100 pA. b) Close-up STM topography of the same molecule with EL spectrum taken while scanning (3.5 V, 100 pA).

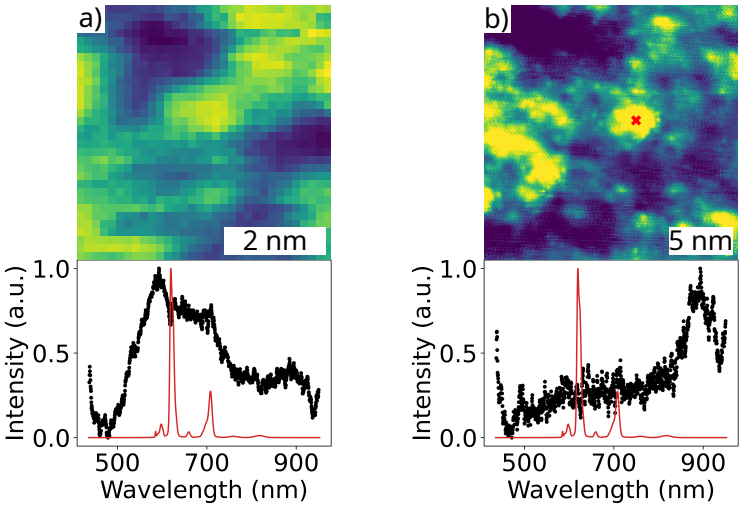

Figure 3.25: STM topography and EL spectra of [Eu(trensal)-Bn-O] on Ag(111). PL spectrum of [Eu(trensal)-Bn-O] overlaid in red for comparison. a) Molecules on Ag(111) with EL spectrum taken while scanning. (3.5 V, 100 pA). b) Molecules on Ag(111) with EL spectrum taken at position indicated by red cross. (3.5 V, 1 pA).

3.5.4 Summary and discussion

This section provided an overview of the steps taken towards EL from Eu^{3+} complexes. The characteristics of working with mirror tips were outlined, highlighting the usefulness of emission from plasmons for evaluating the mirror tip and the optical path. A method for depositing Eu^{3+} complexes on NaCl was established, continuing previous work [61, 62]. While the direct deposition method, which means subliming molecules directly on the substrate at low temperature is sufficient for depositing complexes on NaCl, the indirect method of depositing complexes on a sacrifice sample first results in cleaner samples with less mobility of the complexes.

EL measurements were shown as examples of the experiments tried to obtain luminescence from Eu^{3+} complexes after excitation by tunneling electrons. These examples include [Eu(tta)$_3$(bpy)] deposited on NaCl as a representative of the betadiketonate complexes and the trensal based complexes [Eu(trenal)-Ph-SMe] and [Eu(trensal)-Bn-O]. Different methods were tried, varying the tunneling parameters, and averaging the EL signal over the area of a molecule. However, the EL data shows only plasmonic emission, giving no conclusive indication of emission from Eu^{3+}.

3.6 Results on photophysical properties of Eu^{3+} complexes.

The main findings on the photophysical properties of Eu^{3+} complexes are presented in this section. First, PL spectra and lifetime measurements of [Eu(tta)$_3$(bpy)], [Eu(btfa)$_3$(bpy)] and [Eu(tta)$_3$(H$_2$O)$_2$] samples in powder, solution, drop-casted films and sublimed films on glass substrates demonstrate potential sample preparation methods also suitable for STM. The obtained data are complemented by JO analysis which allows to derive the radiative and non-radiative transition rates. Second, advancing from bulk samples on glass towards thin films ($\sim$ 20 nm) on metal substrates, the optical-setup for light collection from the tunnel junction was improved and the working principle of TCSPC with a single excitation light pulse of 30 ps verified. Tracking the decrease of the PL intensity under UV illumination gives an estimation on the photo-bleaching rate, demonstrating limitations in single molecule experiments. Having established TCSPC measurements inside the STM, thin films of [Eu(tta)$_3$(bpy)], [Eu(btfa)$_3$(bpy)] and [Eu(trensal)] on a metal substrate can be investigated. Choosing [Eu(trensal)] gives first indications about the differences between betadiketonate and trensal based complexes. Furthermore, a variety of TCSPC measurements of platform complexes and betadiketonate complexes in bulk and in a thin film are presented. Recording the TCPSC data at different wavelength ranges proofs that energy is not transferred from the ligands to the first electrically excited state $^5D_0$ of Eu^{3+} directly. Instead, $^5D_0$ is mostly populated by non-radiative transitions from decaying Eu^{3+} states with higher energy. Finally, thin films of [Eu(tta)$_3$(bpy)] with varying thicknesses on a metal substrate point out the modification of dipole emission in front of metal surfaces as the main mechanism reducing the luminescence of molecules adsorbed on metals.

3.6.1 PL spectra and lifetimes in bulk

Sublimation and drop-casting are common methods for depositing molecules on substrates. The process of sublimation can be tuned by temperature and time to provide a reproducible deposition of molecules. Impurities in the sublimable material can often be degassed resulting in cleaner samples than by drop-casting. However, since sublimation requires heating, it can lead to the decomposition of the organic complexes leading to fragments on the sample. Furthermore, finding the right temperature for sublimation can be challenging. On the other hand, drop-casting from solution leads to a more inhomogeneous distribution of molecules on the surface. Remaining solvent and impurities in the material usually lead to a less clean sample in comparison to sublimation. Furthermore, the solubility of the organic complexes and possible decomposition in solution has to be considered.

In order to verify that samples that are suitable for PL as well as STM measurements can be prepared, we deposited $[Eu(btfa)_3(bpy)]$, $[Eu(tta)_3(bpy)]$ and $[Eu(tta)_3(H_2O)_2]$ onto glass substrates by sublimation and drop-casting from ethanol solution. Since we focused on the principle of preparing samples for PL and STM measurements here, the thickness of the films were not checked, but they are estimated to be in the range between several hundred nm and one µm. The material can therefore be considered as bulk. The samples were checked for PL and the observed lifetime determined by TCSPC measurements. All measurements were done at atmosphere and room temperature. JO parameters were derived as described in section 2.7. These results were published in the article *"Photoluminescence and self-assembly of three different Eu complexes"* [52] in the *PCCP* Journal.

The PL spectra of the sublimed and drop-casted $[Eu(btfa)_3(bpy)]$, $[Eu(tta)_3(bpy)]$ and $[Eu(tta)_3(H_2O)_2]$ samples are displayed in figure 3.26 a) and b), respectively. The spectra show the expected emission bands, dominated by the transitions between the first excited state $^5D_0$ to the lower-energy $^7F_{J=0-6}$ levels. The spectra are normalized to the integral intensity of the magnetic dipole allowed transition $^5D_0 \rightarrow {}^7F_1$ [34]. The ratio of the hypersensitive induced ED transition $^5D_0 \rightarrow {}^7F_2$ and the MD allowed transition $^5D_0 \rightarrow {}^7F_1$ gives an indication on the local symmetry of the light emitting metal center following Laporte's rule (see section 2.6). The ratio of the integral intensity of the emission bands from $^5D_0 \rightarrow {}^7F_2$ and $^5D_0 \rightarrow {}^7F_1$ was determined for all six samples to be in the range of 15 to 19, which confirms the expected lack of inversion symmetry in the $[Eu(btfa)_3(bpy)]$, $[Eu(tta)_3(bpy)]$ and $[Eu(tta)_3(H_2O)_2]$ complexes.

The PL spectra of the sublimed and drop-casted films were supplemented by PL measurements taken from powder samples and powder dissolved in ethanol for all three complexes. For each spectrum, all ligand field peaks were fitted and the weighted average peak width calculated. This allows to compare the average peak width of the PL spectra for each sample. The result is shown in Fig. 3.26 c). The errorbars are given by the variance of the fit parameters. The error from repeated measurements is expected to be much larger. The spectra of the drop-casted films show the broadest peaks, which indicates inhomogeneous broadening probably due to remains of solvent in the film and film growth with low order. In ethanol solution, the average linewidth is between the drop-casted and sublimed films. The

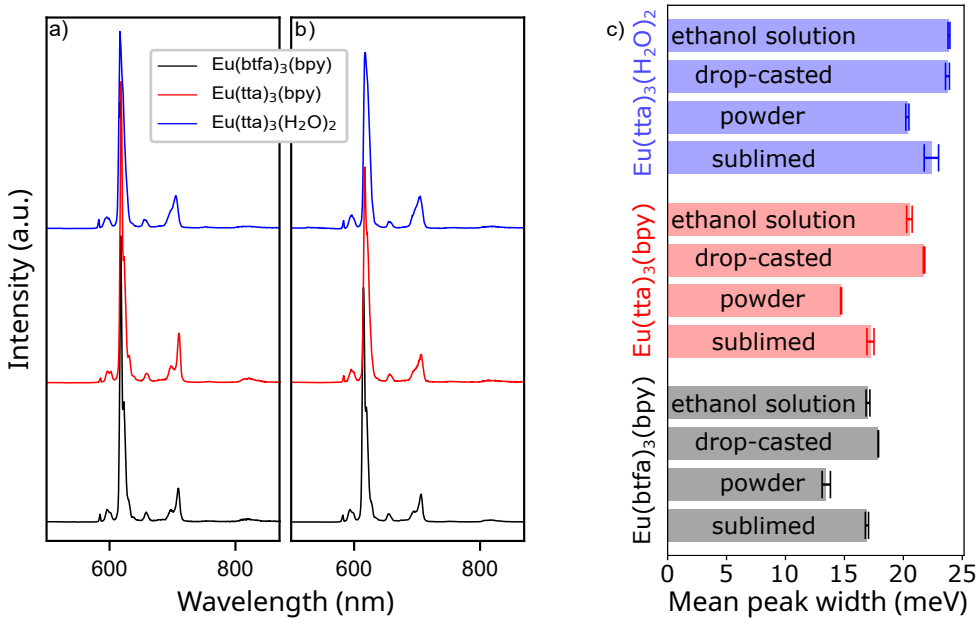

Figure 3.26: PL spectra of a) sublimed and b) drop-casted bulk $[Eu(tta)_3(H_2O)_2]$, $[Eu(tta)_3(bpy)]$ and $[Eu(btfa)_3(bpy)]$ on a glass substrate shifted for clarity after excitation with λ= 375 nm. c) Average linewidth of the PL spectra of $[Eu(tta)_3(bpy)]$, $[Eu(btfa)_3(bpy)]$ and $[Eu(tta)_3(H_2O)_2]$ in powder, in ethanol solution, as a sublimed film on glass and drop-casted on glass. Adapted from [52].

narrow peak width of sublimed films suggests a more well-defined local environment and film growth with higher order. The samples in powder form, exhibit the sharpest emission bands with the narrowest peaks due to micro crystallites within the powder. These crystallites offer a highly ordered environment to the light emitting molecule reducing peak broadening.

The observed lifetime τ_{obs} of the $[Eu(btfa)_3(bpy)]$, $[Eu(tta)_3(bpy)]$ and $[Eu(tta)_3(H_2O)_2]$ complexes in powder form, ethanol solution, sublimed and drop-casted films was determined (Fig. 3.27) by a single exponential fit, since it was expected to depend on the local environment of the light emitting molecule. The errors of the observed lifetimes is given by the variance of the fit parameters. The chemical [52, 158] and optical environment [52, 159] at distances approximating the wavelength of the emitted light are known to influence the observed lifetime. The TCSPC measurements were carried out in atmosphere at room temperature. The contribution of the emission from the $(^5D_0 \rightarrow {}^7F_1)$ transition to the total intensity of the PL spectrum and the observed lifetime allow to estimate the internal quantum yield and the radiative (A_{rad}) and non-radiative (A_{nonrad}) [34, 99, 100] decay rates (see section 2.7). The results are summarized in table 3.1.

In the powder samples (Fig. 3.27 a)), τ_{obs} is around 800 µs for $[Eu(btfa)_3(bpy)]$ and

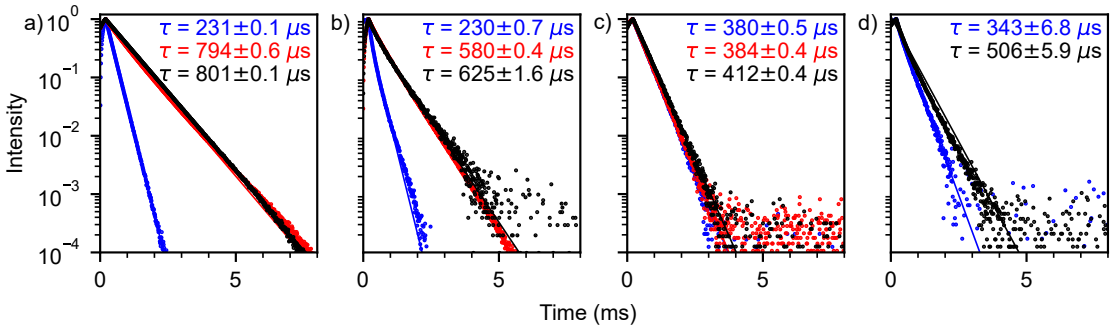

Figure 3.27: Observed lifetimes of $[Eu(tta)_3(H_2O)_2]$ (blue), $[Eu(tta)_3(bpy)]$ (red) and $[Eu(btfa)_3(bpy)]$ (black) in a) powder, b) sublimed film, c) ethanol solution, and d) drop-casted from ethanol solution on a glass substrate after excitation with λ= 375 nm. Adapted from [52].

$[Eu(tta)_3(bpy)]$. In comparison to that, τ_{obs} = 231 µs of $[Eu(tta)_3(H_2O)_2]$ is significantly shorter, which is in agreement with previous work [160]. This reduced lifetime is most likely attributed to vibrations in the OH-groups, opening additional pathways for non-radiative de-excitation [42–44]. This is supported by the comparably large rate of non-radiative decay as estimated from JO theory A_{nonrad} which is around 6 times higher for $[Eu(tta)_3(H_2O)_2]$ in comparison to $[Eu(btfa)_3(bpy)]$ and $[Eu(tta)_3(bpy)]$. In contrast, the rate for radiative decay A_{rad} is of comparable magnitude between 790 Hz and 1145 Hz for all three complexes in powder.

The observed lifetime in the sublimed films of $[Eu(btfa)_3(bpy)]$ and $[Eu(tta)_3(bpy)]$ (Fig. 3.27 b)) is slightly reduced in comparison to the powder samples, while τ_{obs} of the $[Eu(tta)_3(H_2O)_2]$ film is unchanged. This can be attributed to ambient humidity collecting in the film, thus increasing A_{nonrad}, while the non-radiative decay of the $[Eu(tta)_3(H_2O)_2]$ film is still dominated by the water ligands, so A_{nonrad} remains unchanged, which indicates that the water ligands are not cleaved off during sublimation. A_{rad} is higher in the $[Eu(btfa)_3(bpy)]$ and $[Eu(tta)_3(bpy)]$ films than in powder while it is smaller for $[Eu(tta)_3(H_2O)_2]$. It can be rationalized that the refractive index of the glass substrate leads to an increase in A_{rad} for the $[Eu(btfa)_3(bpy)]$ and $[Eu(tta)_3(bpy)]$ films while the enhanced interaction between molecules due to a denser packing in the film increases the quenching by the H_2O groups for $[Eu(tta)_3(H_2O)_2]$.

In the ethanol solution (Fig. 3.27 c)), a reduction of τ_{obs} can be observed for the $[Eu(tta)_3(bpy)]$ and $[Eu(btfa)_3(bpy)]$ samples in comparison to the sublimed films and the powder samples. The decay is now mediated by the solvent for these complexes as is evident from the increased A_{nonrad}. The higher harmonics of hydrogen bond vibrations are known to quench the lifetime [41–43]. For the JO analysis, the refractive index of the medium surrounding the Eu^{3+} complexes has to be considered which leads to a reduction of A_{rad}. For the samples in solid state a refractive index of 1.55 [34] was assumed, while 1.33 was used for the calculation of the complexes in ethanol solution. For the $[Eu(tta)_3(H_2O)_2]$ sample, τ_{obs} is slightly higher in solution than in powder and sublimed films, thus A_{nonrad} is smaller

Sample	Ω_2 (10^{-20} cm^2)	Ω_4 (10^{-20}cm^2)	Ω_6 (10^{-20}cm^2)	A_{rad} (s^{-1})	A_{nonrad} (s^{-1})	Φ_{int}
$[Eu(tta)_3(H_2O)_2]$ e	34.98	7.69	9.32	893.43	1738.15	0.34
$[Eu(tta)_3(H_2O)_2]$ d	17.64	8.24	10.95	747.57	2193.61	0.25
$[Eu(tta)_3(H_2O)_2]$ s	26.75	9.96	16.34	1067.0	3280.82	0.25
$[Eu(tta)_3(H_2O)_2]$ p	31.22	7.02	7.11	1145.25	3202.57	0.26
$[Eu(tta)_3(bpy)]$ e	33.26	7.38	9.26	852.53	1779.05	0.32
$[Eu(tta)_3(bpy)]$ d	24.3	8.61	23.74	973.26	-	-
$[Eu(tta)_3(bpy)]$ s	22.36	10.22	26.38	932.74	791.4	0.54
$[Eu(tta)_3(bpy)]$ p	17.27	7.12	11.02	715.12	550.71	0.56
$[Eu(btfa)_3(bpy)]$ e	26.31	6.09	9.29	692.61	1746.41	0.28
$[Eu(btfa)_3(bpy)]$ d	22.83	6.84	14.79	899.16	1061.62	0.46
$[Eu(btfa)_3(bpy)]$ s	25.63	7.67	19.23	1030.56	556.74	0.65
$[Eu(btfa)_3(bpy)]$ p	20.0	6.39	10.92	789.28	460.72	0.63

Table 3.1: Judd-Ofelt parameters, radiative (A_{rad}) and non-radiative (A_{nonrad}) decay rates and intrinsic quantum yield estimated from the intensity ratios following [34] and references therein and the experimentally observed lifetimes. Suffixes e, d, s, p denote ethanol solution, drop-casted, sublimed and powder samples respectively. From [52].

in solution than in powder and the sublimed film, while A_{rad} is slightly increased. This can be rationalized by the reduced vibronic coupling between complexes in solution, since the non-radiative decay by the water ligands is dominant over the quenching by the solvent.

In the films drop-casted from ethanol solution (Fig. 3.27 d)), τ_{obs} of $[Eu(tta)_3(H_2O)_2]$ is slightly smaller than in solution, while it is slightly increased for $[Eu(btfa)_3(bpy)]$. The drop-casted $[Eu(tta)_3(bpy)]$ sample could not be measured due to deterioration after being exposed to atmosphere for a prolonged time. τ_{obs} is higher in the drop-casted film than in solid state but slightly smaller than in solution for $[Eu(tta)_3(H_2O)_2]$ while the situation is reversed for $[Eu(btfa)_3(bpy)]$. It is plausible that ethanol is still present in the dried film that quenches τ_{obs} for $[Eu(btfa)_3(bpy)]$ while reducing the quenching by the water ligands in $[Eu(tta)_3(H_2O)_2]$. This is supported by the values of A_{rad} and A_{nonrad} being between the values for solution and sublimed films for both complexes.

For completeness, an overview of the emission spectra of $[Eu(tta)_3(H_2O)_2]$, $[Eu(tta)_3(bpy)]$, $[Eu(btfa)_3(bpy)]$, [Eu(TACN)], [Eu(trensal-Ph-Sme)], [Eu(trensal)] and [Eu(trensal-O-Bn)] powder samples measured at room temperature is provided in Fig. 3.28. The logarithmic y-scale reveals that all $^5D_0 \rightarrow {}^7F_{J=0-6}$ transitions can be detected. The spectra of [Eu(trensal)] and [Eu(TACN)] are shifted by 10 nm as a result of modifying the optical set-up which leads to the light entering the spectrometer at a slightly different angle. In the spectra of [Eu(TACN)] and $[Eu(tta)_3(H_2O)_2]$, emission from the $^5D_1$ state can easily be distinguished at 540 and 560 nm, and 530 and 550 nm, respectively.

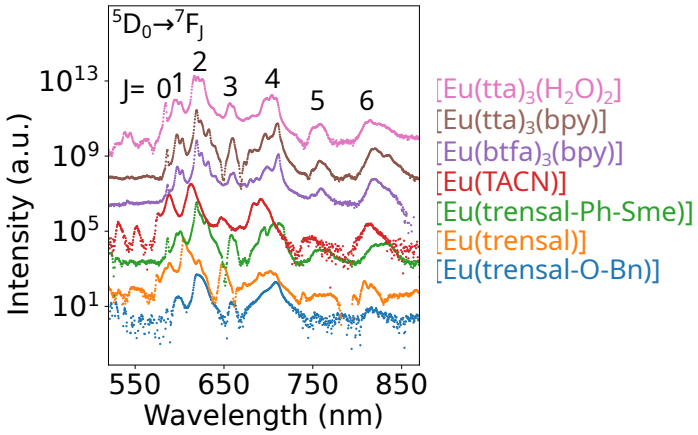

Figure 3.28: Overview of the PL spectra of various powder samples after excitation with $\lambda = 375$ nm on logarithmic y-scale. The background was subtracted and all spectra normalized to the integrated $^5D_0 \rightarrow {}^7F_1$ transition. Graphs shifted for clarity.

Summary and discussion

This section provided a proof of concept on potential sample preparation methods for PL experiments. [Eu(btfa)$_3$(bpy)], [Eu(tta)$_3$(bpy)] and [Eu(tta)$_3$(H$_2$O)$_2$] samples on glass substrates were prepared by sublimation and drop-casting from ethanol solution. It was shown that these preparation methods are suitable for PL experiments and result, at least partially, in the deposition of intact complexes. The differences among the sample preparation methods were quantified by calculating the average line width of the PL emission from sublimed and drop-casted samples. The data was supplemented by powder samples and molecules in solution. The results indicate the presence of micro-crystallites in the powder, while sublimed and drop-casted films offer a less well defined environment to the Eu^{3+} ion.

TCSPC measurements were carried out for all three complexes, in powder, solution and as drop-casted and sublimed films. The obtained data provide insight in the impact of the refractive index of the medium surrounding the Eu^{3+} ion, while also clearly demonstrating a reduction of the observed lifetime τ_{obs} mediated by vibronic relaxation. These findings were supplemented by JO analysis, which allows to estimate the radiative and non-radiative transition rates and the internal quantum yield. The comparison between [Eu(btfa)$_3$(bpy)] and [Eu(tta)$_3$(bpy)] that have similar structures and [Eu(tta)$_3$(H$_2$O)$_2$] that shows strong quenching due to OH-vibrations demonstrates the potential of PL and TCSPC measurements for pointing out quenching mechanisms due to structural differences. A comparison between samples prepared by different preparation methods allows to draw conclusions on the impact of film growth and the surrounding medium on the luminescence.

3.6.2 Influence of tip position on TCSPC

The PL decay of the bulk samples presented in the previous chapter used an array of light pulses for excitation to increase the PL intensity. While this is sufficient to obtain the observed lifetime, some measurements such as determining the rise time (see section 3.6.5) require excitation by a single short (30 ps) light pulse. The proof of concept of this method relying on a single excitation pulse is outlined in this section, showing applicability also for measurements inside the STM cavity and briefly discussing artifacts.

A thin film of [Eu(tta)$_3$(bpy)] was sublimed onto clean Ag(111) with a coverage of 22.5 molecules/nm^2. The sample was excited with light (λ=375 nm, 30 ps), and the decay of the PL signal of the main $^5D_0 \rightarrow {}^7F_2$ transition at 610 ± 10 nm tracked by TCSPC. The decay was measured inside the STM at 4.5 K using a mirror tip (see section 3.1.3, Fig. 3.3 set-up C) supplemented by one measurement in the preparation chamber at room temperature for comparison (see section 3.1.3, Fig. 3.3 set-up B). In the STM, the tip-sample distance was varied in the range of 5 - 300 nm. An additional measurement was done in tunneling contact (100 pA, 2 V). The decays are shown in Fig. 3.29. The background was subtracted. The graphs are normalized to the integral intensity of the $^5D_0 \rightarrow {}^7F_1$ MD transition and shifted for clarity. The decay data cannot be described by a single exponential function sufficiently, which indicates contributions to the PL signal from different species of molecules or molecules with different chemical or optical environments (see section 3.6.4). For this reason, the data was fitted with the sum of two exponential functions. The thus obtained τ_{obs} are included in the figure. The whole set of fit parameters is listed in table 3.2. τ_{obs} on the short scale is in the range of 120 - 200 µs, τ_{obs} on the long scale is between 560 - 690 µs. It is apparent that there is no systematic variation in either τ_{obs} when changing the tip-sample distance. There is also no significant difference between the measurement performed in the preparation chamber at room temperature and the measurement in the STM at 4.5 K. The modification of dipole emission in front of metal surfaces is expected to be the main determining factor for τ_{obs} (see section 2.4.2). This effect is independent of temperature which explains the similar values for measurements at 4.5 K and at room temperature. Furthermore, tunneling conditions do not influence the decay. This is expected since only a single molecule is involved in the electron transport by tunneling, while the PL signal consists of light from several molecules. It should also be noted that for thick films and dielectric substrates non-radiative processes are dominant, as can be seen when comparing radiative and non-radiative transition rates as derived from JO-theory (see section 3.6.1, table 3.1).

The time constant for the population of the $^5D_0$ level (rise time), was measured as part of this thesis (see section 3.6.5). This requires investigating the decay of the PL signal within the first few µs. For this reason, the switch-on effect in TCSPC measurements will be treated here. While an in depth investigation is beyond the scope of this thesis, a brief discussion will show the characteristics of the optical set-up. 30 ps light pulses with $\lambda = 375$ nm were sent into the STM onto a clean Ag(111) reference sample at 4.5 K. The response signal was tracked with TCSPC for wavelengths in the range of 450 ± 10 - 670 ± 10 nm.

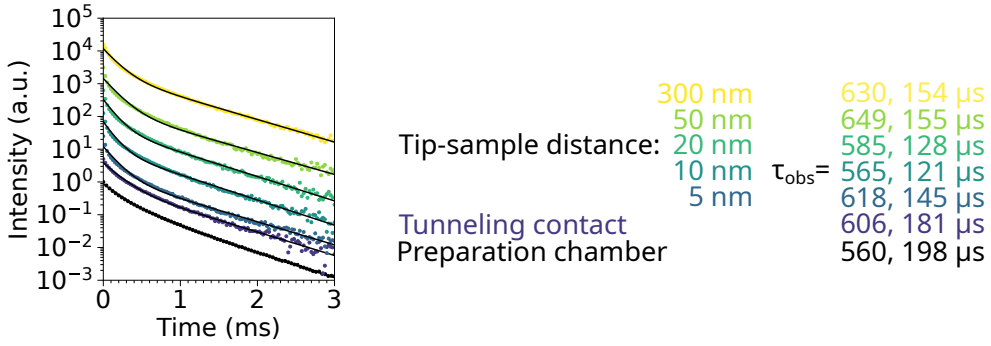

Figure 3.29: Decay of a 22.5 molecules/nm^2 thin film of [Eu(tta)$_3$(bpy)] on Ag(111) measured with the PL set-up inside the preparation chamber at room temperature and with the PL set-up inside the STM at 4.5 K at different tip-sample distances. The intensity of the $^5D_0 \rightarrow {}^7F_2$ was tracked at 610 ± 10 nm using TCSPC. The excitation light is excluded and the background subtracted. τ_{obs} was obtained by fitting the sum of two exponential functions. Graphs shifted for clarity.

The measurement at 610 ± 10 nm was done first and repeated after all other measurements to rule out any effects that might arise from bleaching or instabilities in the light source. The decaying signals are displayed in Fig. 3.30. The dark count background was subtracted. It is apparent that several features are present within the first 200 ns. While a systematic study is unnecessary for the measurements done in this work, the features are expected to arise from reflections mostly at the interfaces of the optical fibers, as well as afterpulsing in the SPADs [161]. The decaying background stems from autofluorescence in the optical fibers. At least the first few hundred ns are therefore excluded in TCSPC measurements.

Tip-sample distance (nm)	$\tau_{obs,1}$ (µs)	$\sigma^2(\tau_{obs,1})$ (µs)	$\tau_{obs,2}$ (µs)	$\sigma^2(\tau_{obs,2})$ (µs)	A_1	$\sigma^2(A_1)$	A_2	$\sigma^2(A_2)$
300	630	6	154	5	0.1233	0.0039	0.625	0.028
50	649	13	155	9	0.0551	0.0036	0.408	0.033
20	585	9	128	8	0.0717	0.0037	0.45	0.04
10	565	8	121	8	0.078	0.004	0.47	0.05
5	618	11	145	9	0.0621	0.0039	0.421	0.037
Tunneling	606	20	181	21	0.161	0.019	0.61	0.08
Prep chamber	560	3	198	5	0.254	0.006	0.630	0.015

Table 3.2: Observed lifetimes τ_{obs}, $[\tau_{obs}]$=µs and amplitudes A of a thin ([Eu(tta)$_3$(bpy)]) film on Ag(111) with a coverage of 22.5 molecules/nm^2 measured in the STM at 4.5 K at different tip-sample distances between $\sim 300 - 5$ nm as well as in tunneling condition and using the PL set-up in the preparation chamber (see section 3.1.3, Fig. 3.3, set-up A) as derived by fitting the sum of two exponential functions. The variance of the fit parameters is given by σ^2. PL excitation via light with $\lambda = 375$ nm, 30 ps. The $^5D_0 \rightarrow {}^7F_2$ decay at 610 ± 10 nm was tracked.

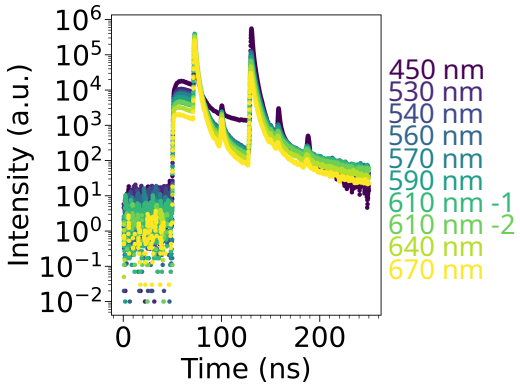

Figure 3.30: Reflections and artifacts in TCSPC measurements within the first 200 ns. TCPSC was measured on a clean Ag(111) reference sample in the STM at 4.5 K after sending in light pulses with λ=375 nm, 30 ps. The response was collected at different wavelengths in the range of 450 ± 10 - 670 ± 10 nm. The measurement at 610 ± 10 nm was done first and repeated at the end to rule out effects arising from bleaching or instabilities in the light source. The dark count background was subtracted.

Summary and discussion

In this section TCSPC measurements on a thin film of [Eu(tta)$_3$(bpy)] with a coverage of 22.5 molecules/nm^2 on a Ag(111) substrate were presented. The measurements were carried out at 4.5 K using the PL set-up inside the STM with a mirror tip. The tip-sample distance was varied from 5 to 300 nm. Additionally, the luminescence decay of the same sample at room temperature was measured using the optical set-up inside the preparation chamber without mirror tip. No systematic variation in the derived decay constants τ_{obs} with tip-sample distance was found, nor is there a significant difference between the measurements with mirror tip at 4.5 K and without mirror tip at room temperature. The absence of a reduction of τ_{obs} for decays inside the STM cavity is due to the fact that the cavity enhancement is very weak for large distances and that only a small fraction of the molecules are located inside the cavity. The modification of dipole emission in front of metal surfaces, which is temperature independent, is expected to be the main factor influencing the lifetime, since no difference between the measurement at room temperature and at 4.5 K was found.

It was furthermore demonstrated, that the first 200 ns of TCSPC data obtained by a single excitation pulse contain several spikes in intensity across the entire wavelength range. These are attributed to to a complex combination of autofluorescence, propagation delays in the optical fibers and reflections at the interfaces of optical fibers and afterpulsing of the SPADS. For this reason, the first 200 ns after excitation are omitted in TCSPC measurements.

3.6.3 Decrease of luminescence intensity under UV illumination

The bleaching of Eu^{3+} complexes by exposure to UV light is well known. While there are studies on complexes in solution [162], embedded in host matrices [163–166] or single crystals [167], often only qualitative conclusions are drawn. This thesis aims towards enabling PL studies on electrically contacted single molecules. For this reason, the photo-degradation process of a thin [Eu(tta)$_3$(bpy)] film on Ag(111) at 4.5 K with a coverage of 22.5 molecules/nm^2 was quantified. These results were published in [168]. The sample was prepared by subliming [Eu(tta)$_3$(bpy)] at a crucible temperature of 185 °C for 14 min after degassing at 150 °C for several hours. The sample was then exposed to UV light ($\lambda = 375$ nm) for excitation and the PL response measured repeatedly with PL set-up B (see section 3.1.3, Fig. 3.3). The thus recorded spectra were integrated to obtain the intensity of all emission bands over time. This is shown in Fig. 3.31 a) (black dots). Also displayed is the integrated intensity of the main $^5D_0 \rightarrow {}^7F_2$ transition (yellow dots). Both data sets were fitted with a single exponential to estimate the photo-bleaching lifetime. The photo-bleaching lifetimes are around $7 \cdot 10^3$ and $6 \cdot 10^3$ s for the overall emission and for the main emission, respectively. This corresponds to approximately 10^5 photons emitted by each Eu^{3+} complex until the PL intensity drops to $1/e$. The photo-bleaching probability is therefore of the order of 10^{-5} which is comparable to the photo-bleaching probabilities of organic dyes in water and at room temperature (10^{-3} - 10^{-7}) [169]. For a single molecule, this would correspond to a bleaching probability of $1 - 1/e = 66$ % after 10^5 photons, which is insufficient for performing PL on single molecules over an extended period of time.

The position of the main $^5D_0 \rightarrow {}^7F_2$ emission band was determined for each spectrum taken (Fig. 3.31 b)). There is no significant change over time within the margin of error. Furthermore, the integrated intensity at different wavelength ranges is shown in Fig. 3.31 c). There is no increase in intensity at any wavelength range, which would be taken as an indication for a fragmentation of the complex or reduction from Eu^{3+} to Eu^{2+} [170].

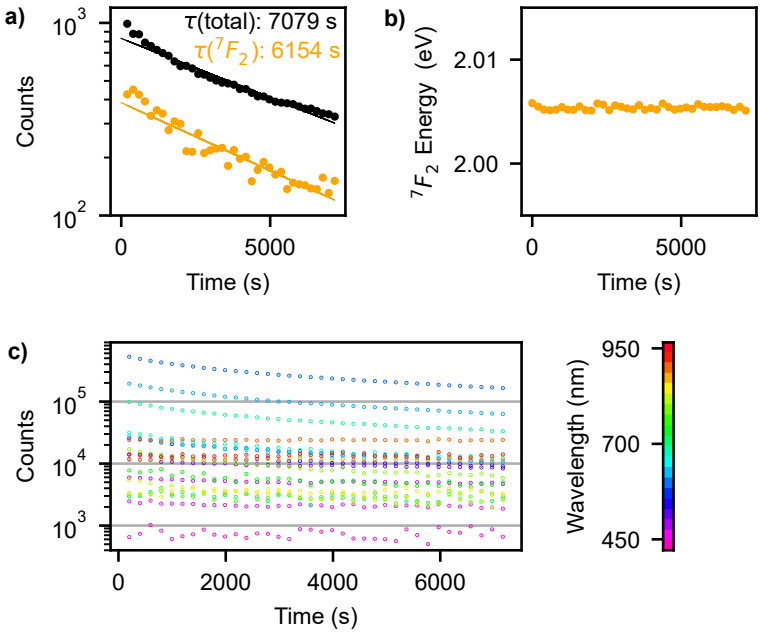

Figure 3.31: Decrease of the PL intensity of a $[Eu(tta)_3(bpy)]$ film on Ag(111) at 4.5 K with 22.5 molecules/nm^2 coverage under illumination with UV light ($\lambda = 375$ nm). a) Decrease in PL intensity over time for all emission bands integrated (black dots) and for the main emission band $^5D_0 \rightarrow {}^7F_2$ (yellow dots). The data was fitted with a single exponential, the according decay constants are included. b) Peak position of the main $^5D_0 \rightarrow {}^7F_2$ emission band over time. c) Decrease in PL intensity tracked at several wavelengths intervals ranging between 450 and 950 nm. From [168].

Summary and discussion

The decrease of the luminescence intensity under UV illumination due to photo-bleaching was investigated in this section. This was done by repeatedly measuring the PL of a $[Eu(tta)_3(bpy)]$ film on Ag(111) with a coverage of 22.5 molecules/nm^2 at 4.5 K. The PL spectra decline over time for all wavelengths without an increase at a specific range which would indicate a fragmentation of the complex or reduction of Eu^{3+}. The decrease in intensity was quantified by integrating the PL spectra to obtain the PL intensity over time. This allowed to estimate the photo-bleaching probability to 10^{-5} which is considered insufficient for performing extended experiments on single molecules.

3.6.4 PL spectra and lifetimes in thin films

In section 3.6.1 it was shown that the Eu^{3+} complexes [Eu(btfa)$_3$(bpy)], [Eu(tta)$_3$(bpy)] and [Eu(tta)$_3$(H_2O)$_2$] can be sublimed to prepare samples suitable for PL measurements. However, the sublimed films had unknown but very large thicknesses and were considered bulk. After a reliable method for depositing a controlled amount of molecules on the substrate had been established (see section 3.2.2 and 3.3), thin films could be prepared. [Eu(btfa)$_3$(bpy)], [Eu(tta)$_3$(bpy)] and [Eu(trensal)] were sublimed on glass and Ag(111). The comparison between dielectric and metallic substrates gives a first indication on the energy transfer to the metal. This will be discussed in greater detail in section 3.6.6. The trensal based complex [Eu(trensal)] was chosen to compare against the betadiketonate based complexes [Eu(btfa)$_3$(bpy)] and [Eu(tta)$_3$(bpy)]. These results were published in [168].

[Eu(btfa)$_3$(bpy)], [Eu(tta)$_3$(bpy)] and [Eu(trensal)] samples with a coverage of 22.5 molecules/nm^2 were prepared by sublimation on clean Ag(111) and on clean glass substrates. [Eu(btfa)$_3$(bpy)] and [Eu(tta)$_3$(bpy)] were sublimed at 185 °C, after degassing at 150 °C for several hours. [Eu(trensal)] was sublimed at 280 °C. PL was measured on the thin film samples on glass at room temperature using the set-up in the preparation chamber, the films on Ag(111) were measured inside the STM at 4.5 K (see section 3.1.3, Fig. 3.3, set-ups A and C). UV light with $\lambda = 375$ nm was used for excitation. The data sets of thin films are supplemented by PL spectra of powder samples for comparison. The auto-fluorescence background was subtracted and the spectra normalized to the integrated emission from the $^5D_0 \rightarrow {}^7F_1$ transition [126]. The graphs are shifted for clarity (Fig. 3.32 a)-c)). The PL spectra show the well known emission bands of Eu^{3+} for the $^5D_0 \rightarrow {}^7F_{J=0-4}$ transitions. For these samples, four different mechanisms affecting the emission spectra have to be considered. These are: chemical changes [158] or differences in the molecular arrangement influencing the ligand-field splitting [34]; the impact of the optical environment of the molecule; and the interaction between the complex and the metal surface. The optical environment is considered isotropic in powder, while the vacuum-glass interface creates a discontinuity in the refractive index, and the Ag(111) substrate is highly reflective [159, 171]. The matter-light interaction of complex and metal substrate can lead to the coupling of the dipole transition of the complex with surface plasmons [48]. Furthermore, hybridization of the 4f states and the conduction electrons of the metal substrate can increase charge transfer from complex to substrate thus providing a strong de-excitation channel and quenching luminescence.

It is apparent that for films on Ag(111) (Fig. 3.32 a)-c)) the ratio of emission from the induced ED transitions and the emission from the MD transition is lowest for all samples. This can be explained by the optical set-up mainly detecting light emitted perpendicular to the substrate plane. Due to the differences of the electric and magnetic field components in front of metal surfaces (see section 2.4.2), the set-up preferably detects emission from MD transitions in comparison to induced ED transitions. Normalizing the spectra to the $^5D_0 \rightarrow {}^7F_1$ MD transition leads to a relative decrease of the induced ED transitions in films on Ag(111). The modification of luminescence due to the presence of the metal surface will be discussed in more detail in section 3.6.6. The $^5D_0 \rightarrow {}^7F_0$ transition is strictly forbidden

according to JO theory. However, the selection rules can be relaxed by J mixing induced by the ligand field. Emission from $^5D_0 \rightarrow {}^7F_0$ at around 585 nm can be distinguished in the sublimed samples of [Eu(tta)$_3$(bpy)] and [Eu(btfa)$_3$(bpy)] on glass. In the powder samples this emission band is nearly absent, especially for [Eu(btfa)$_3$(bpy)]. This indicates a modification of the ligand field upon sublimation, possibly by a deformation due to a different inter molecular arrangement. The molecular material used for sublimation contains microcrystallites, providing a well defined environment for the light emitting center of the complex. In films, no crystallization is expected. Fragmentation of the complexes, e.g. by cleaving of the ligands is also possible, either by sublimation itself [143] or by the interaction with the substrate [140], as has already been discussed in the analysis of the STM topography data (see section 3.3). The modification of the surrounding order in [Eu(btfa)$_3$(bpy)] is supported by the individual ligand field levels of the $^5D_0 \rightarrow {}^7F_2$ ($\sim$ 610 nm) and $^5D_0 \rightarrow {}^7F_4$ ($\sim$ 700 nm) bands being sharper in the powder sample in comparison to the thin films. Sharper ligand field levels can be explained by a more well defined environment provided by the crystalline powder samples of [Eu(btfa)$_3$(bpy)]. On the samples investigated here, the ligand field levels of the [Eu(tta)$_3$(bpy)] film on glass are sharper than the levels of the [Eu(btfa)$_3$(bpy)] film on glass. Due to the similar molecular structures of [Eu(btfa)$_3$(bpy)] and [Eu(tta)$_3$(bpy)], this difference is not expected to be systematic. This observation can be explained by the fact that the [Eu(tta)$_3$(bpy)] material was used more often for sublimation and does therefore contain less contamination, due to more thorough degassing. For [Eu(trensal)], the PL spectra of two powder samples and two thin films with the same coverage on glass are included to provide an estimation of reproducibility. The spectra of the powder samples are shifted with respect to the other spectra by 10 nm. This is a result of a modified optical set-up that results in the light entering the spectrometer at a different angle. The ratio of emission from the $^5D_0 \rightarrow {}^7F_2$ transition to the $^5D_0 \rightarrow {}^7F_1$ transition is about twice as high on one thin film on glass, while it is about 20 % higher on the other film in comparison to the powder samples. Furthermore, emission from the $^5D_0 \rightarrow {}^7F_3$ transition is clearly increased in relation to the $^5D_0 \rightarrow {}^7F_1$ emission band. This is the case for both [Eu(trensal)] samples on glass. The most plausible explanation is an increased radiative rate, caused by a relaxation of selection rules for [Eu(trensal)] films on glass due to a reduction in the coordination environment upon sublimation [172]. This is supported by the fact that [Eu(trensal)] has C3 symmetry, while [Eu(btfa)$_3$(bpy)] and [Eu(tta)$_3$(bpy)] are C1 symmetric. The crystalline powder samples provide a local coordination environment with high symmetry for [Eu(trensal)] which is greatly reduced upon sublimation. This reduction in symmetry is less pronounced for the betadiketonate complexes that already have a low symmetry in powder. Furthermore, the emission of [Eu(trensal)] does not show significant line broadening upon sublimation, as for example observed for [Eu(btfa)$_3$(bpy)]. This is attributed to the more rigid structure of [Eu(trensal)] being less prone to damage upon sublimation, which results in fewer different molecular species on the sample, and thus a more ordered film.

In addition to the PL spectra, the decay of the main $^5D_0 \rightarrow {}^7F_2$ emission band was tracked by TCSPC measurements with a 610 $\pm$ 10 nm band-pass filter. This allows to compare the dynamics of the light emitting excited states of the three different complexes. The samples were excited with UV light of $\lambda = 375$ nm with prolonged illumination time (0.1 to 0.5 ms) if

not stated otherwise. The decays for the three different samples in powder form and as thin films with coverage of 22.5 molecules/nm^2 on glass and on Ag(111) are shown in Fig. 3.32 d)-f). The powder samples were measured at room temperature and atmosphere, the films on glass were measured using the set-up in the preparation chamber at room temperature (see section 3.1.3, Fig. 3.3 set-up A), the films on Ag(111) were measured at 4.5 K using set-up C) (see section 3.1.3, Fig. 3.3). The decay of the PL intensity cannot be sufficiently described by a single exponential decay, except for the [Eu(trensal)] film samples on glass and the [Eu(btfa)$_3$(bpy)] powder sample. This deviation from a single exponential decay indicates similarly dominant de-excitation mechanisms on different timescales. These can be induced by different environments of the light emitting metal center for example caused by the distance to the substrate or different species of molecules. The fits are represented by the dashed graphs. The fit parameters are listed in table 3.3.

When comparing the PL decay dynamics of the three complexes in powder, τ_{obs} is about a factor of two smaller for [Eu(trensal)] ($\sim$ 400 µs) in comparison to [Eu(btfa)$_3$(bpy)] and [Eu(tta)$_3$(bpy)] ($\sim$ 800 µs). This trend of reduced lifetimes in [Eu(trensal)] is also present in the thin film samples. This is in agreement with previous work [52, 113]. For [Eu(btfa)$_3$(bpy)] and [Eu(tta)$_3$(bpy)], τ_{obs} is shorter in the thin film samples than in powder which is in agreement with my previous findings [52] and literature [159]. The reduction in lifetime is mostly attributed to an increased non-radiative transition rate caused by inhomogeneities and contamination in the films, as well as an increased radiative transition rate due to a less ordered environment. The large τ_{obs} of [Eu(tta)$_3$(bpy)] on Ag(111) might be a result of exciting with a single excitation pulse on this sample and shows the impact of the exact experimental details. For [Eu(trensal)] τ_{obs} is greatly reduced on the thin film samples on glass. When considering the increased ratio of induced ED vs. MD transitions in the PL spectra of these samples, this most likely arises from an increased radiative transition rate. JO analysis was refrained from since it is based on the principle that light from emitting dipoles is collected with equal probability, which is not considered valid for thin films on substrates.

The difference in the decay dynamics between [Eu(trensal)] and the two betadiketonate based complexes is taken as another indication that the sublimation process has a higher impact on the intactness of [Eu(btfa)$_3$(bpy)] and [Eu(tta)$_3$(bpy)] in comparison to [Eu(trensal)]. However next to symmetry and integrity of the complexes, there are additional factors that need to be considered. The presence of hydroxyl groups on the glass surface can lead to additional quenching of luminescence via phonons. Furthermore, the increased refractive index of the glass substrate and the discontinuity at the glass vacuum interface modifies the photonic density of states therefore increasing the radiative decay rate. Finally, for films on the metal surface, the modification of the dipole emission by the metal substrate provides a de-excitation pathway that reduces the lifetime as will be shown in section 3.6.6. The unlikely hybridization of the 4f orbitals of Eu^{3+} with the conduction electrons of the metal surface, or charge transport by tunneling 4f electrons would lead to significant de-excitation on a timescale much shorter than PL lifetimes. This would drastically reduce the PL signal of films sublimed on metal by orders of magnitude, which was not observed. However, the

Sample	τ_1	$\sigma^2(\tau_1)$	τ_2	$\sigma^2(\tau_2)$	A_1	$\sigma^2(A_1)$	A_2	$\sigma^2(A_2)$
[Eu(btfa)$_3$bpy] p	800.0	0.8			1.0120	0.0015		
[Eu(btfa)$_3$bpy] g	200	6	46.7	2.2	0.267	0.016	0.875	0.032
[Eu(btfa)$_3$bpy] m	137	8	24.0	2.1	0.221	0.021	0.95	0.07
[Eu(tta)$_3$bpy] p	906.0	3.2	403	39	0.940	0.009	0.06	0.01
[Eu(tta)$_3$bpy] g	173	9	54.1	3.3	0.349	0.037	0.753	0.032
[Eu(tta)$_3$bpy] m	444.002	0.012	49.062	0.037	0.81589	0.00003	0.16320	0.00008
[Eu(trensal)] p1	350	18	78.2	2.4	0.170	0.013	0.855	0.016
[Eu(trensal)] p2	421	27	107	6	0.270	0.029	0.847	0.029
[Eu(trensal)] g1	68.0	1.7			1.50	0.10		
[Eu(trensal)] g2	57	6			1.30	0.13		
[Eu(trensal)] m	184	5	28.4	1.8	0.292	0.013	0.81	0.04

Table 3.3: Fit results for the observed lifetimes (τ, [τ]=µs), amplitudes A and their variance σ^2 of [Eu(btfa)$_3$(bpy)], [Eu(tta)$_3$(bpy)] and [Eu(trensal)] powder samples (p) and thin films on metal (m) and glass substrates with a coverage of 22.5 molecules/nm^2 (g). The emission of the $^5D_0 \rightarrow {}^7F_2$ transition was tracked with a 610 ± 10 bandpass filter. The decay data was fitted with a single, or double exponential function.

films have a conductance sufficient for tunneling as is shown by the relatively stable STM topography in Fig. 3.32 f).

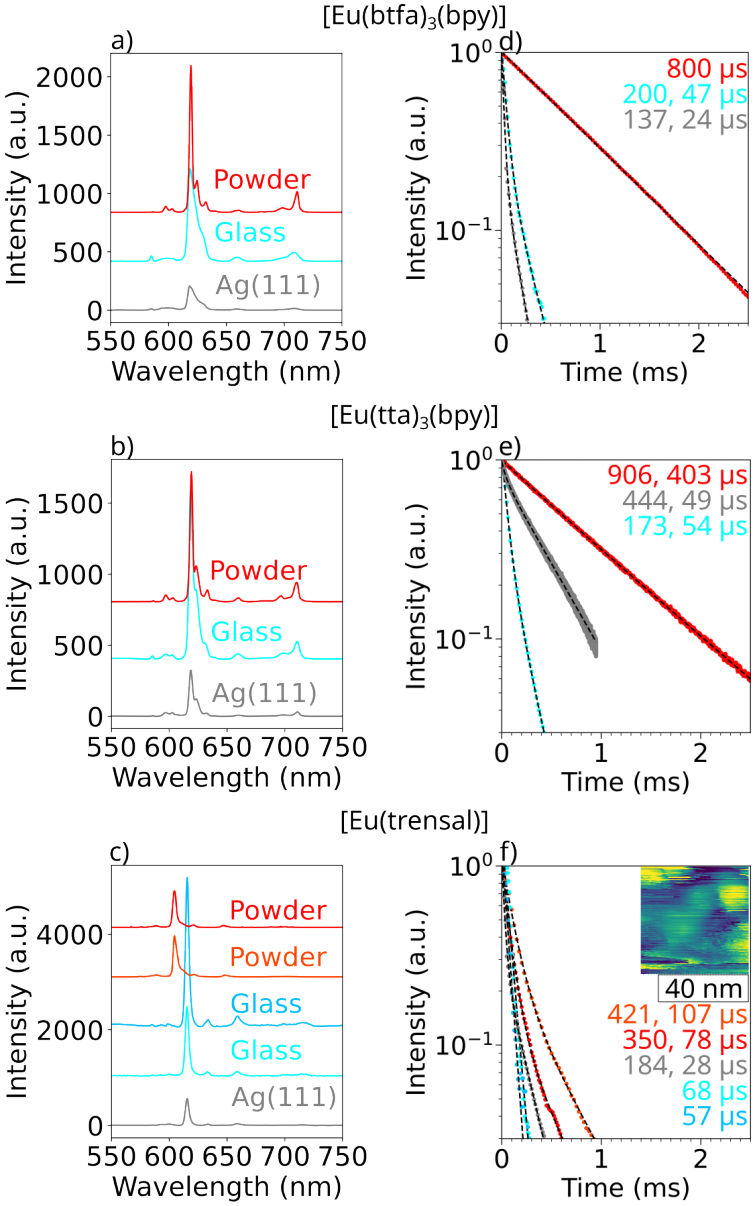

Figure 3.32: PL spectra and lifetimes of [Eu(btfa)$_3$(bpy)], [Eu(tta)$_3$(bpy)] and [Eu(trensal)] in powder and in films with $\sim$ 22.5 molecules/nm^2 coverage on Ag(111) and on glass. For excitation UV light (λ = 375 nm) was used. a)-c) PL spectra recorded at room temperature. The autofluorescence background was subtracted and the spectra normalized to the $^5D_0 \rightarrow {}^7F_1$ transition. Graphs shifted for clarity. d)-f) Decay of the PL intensity of the main $^5D_0 \rightarrow {}^7F_2$ emission band as obtained from TCSPC measurements using a 610 $\pm$ 10 nm band-pass filter. The decays were fitted with the sum of two exponential functions, the thus determined τ_{obs} are included. The colors correspond to the different samples: powder: red, orange; film on glass at room temperature: cyan, blue; film on Ag(111) at 4.5 K: gray. An STM topography image of a [Eu(trensal)] film with 22.5 molecules/nm^2 is included in f), indicating relatively stable conductivity. (STM parameters: -10.0 V, 1 pA). From [168].

Summary and discussion

This section focused on PL and TCSPC measurements of the betadiketonate complexes [Eu(btfa)$_3$(bpy)] and [Eu(tta)$_3$(bpy)] and the trensal complex [Eu(trensal)]. The measurements were performed on thin films of these complexes with a coverage of 22.5 molecules/nm^2 on glass and Ag(111) substrates, supplemented by measurements of powder samples. The structural difference between betadiketonate and trensal based complexes is reflected in the emission spectra. It was concluded that [Eu(trensal)] is more susceptible to changes in the local coordination environment upon sublimation, while also being less prone to fragmentation in comparison to the betadiketonate complexes. Furthermore, the unique properties of dipole emission in front of metallic surfaces were discussed.

TCSPC measurements were carried out on the three different complexes in powder and as sublimed films on glass and Ag(111). It was shown that the decay of the PL signal often has to be described by the sum of two exponential functions which indicates emission from molecules with different environments. The TCSPC data complements the conclusions drawn from the PL spectra, also indicating that [Eu(trensal)] is more prone to structural changes upon sublimation.

3.6.5 Accessing the $^5D_1 \rightarrow {}^5D_0$ transition

Many publications focus on the main transitions of Eu^{3+} from the first excited $^5D_0$ state to the $^7F_0$ ground levels. However, transitions from the higher excited state $^5D_1$ can also be observed, although they are weaker and some bands are close to the emission bands of $^5D_0$ (see table 2.3). Observing emission from $^5D_1$ in Eu^{3+} complexes means that either the Eu^{3+} ion is directly excited or the ligands do not transfer their energy directly to the $^5D_0$ state. A direct excitation of the Eu^{3+} ion is unlikely due to the shielding of the 4f orbital. The non-radiative $^5D_1 \rightarrow {}^5D_0$ transition is not directly accessible, but emission from $^5D_0 \rightarrow {}^7F_J$ and $^5D_1 \rightarrow {}^7F_J$ can be compared. Due to the improvements of the optical set-up that were done as part of this thesis, samples of Eu^{3+} complexes can now be excited with a single, short light pulse and the PL response collected. This reveals an initial increase in intensity from the emission of the $^5D_0$ state that is caused by the non-radiative $^5D_1 \rightarrow {}^5D_0$ transition.

TCSPC measurements were carried out on powder samples of [Eu(tta)$_3$(bpy)], [Eu(tta)$_3$(H$_2$O)$_2$], [Eu(trensal-Ph-SMe)], [Eu(TACN)] at room temperature as well as on a film of [Eu(tta)$_3$(bpy)] sublimed on Ag(111) with a coverage of 22.5 molecules/nm^2 (Fig. 3.33 and 3.34), measured at 4.5 K with set-up B (see section 3.1.3, Fig. 3.3). The samples were excited with a single pulse of light (λ = 375 nm, 30 ps). Bandpass filters of 540±10, 560±10 and 610±10 nm were positioned in front of the SPAD to track the decay of the $^5D_1 \rightarrow {}^7F_{1,2}$ and $^5D_0 \rightarrow {}^7F_2$ transitions. The $^5D_1 \rightarrow {}^7F_{1,2}$ transitions were chosen because their emission can easily be separated from the $^5D_0 \rightarrow {}^7F_2$ emission bands. The observed lifetime of a transition is intrinsic to the initial state (see section 2.3), i.e. tracking the $^5D_1 \rightarrow {}^7F_1$ and $^5D_1 \rightarrow {}^7F_2$ decay should lead to the same τ_{obs}. For each measurement, the background was subtracted and the first few hundred ns excluded, since they contain mostly autofluorescence of the excitation light.

Emission from the $^5D_0 \rightarrow {}^7F_2$ transition is strong in the samples of [Eu(tta)$_3$(bpy)] and [Eu(tta)$_3$(H$_2$O)$_2$]. From the data represented on the long time scale (Fig. 3.33 a)), it is apparent that the intensity of the [Eu(tta)$_3$(bpy)] sample rises at first and then declines, while the intensity of the $^5D_1 \rightarrow {}^7F_{1,2}$ transitions declines much faster. The rise in emission from $^5D_1$ is not observed since in happens on the nanosecond time scale [115, 129, 130]. While emission at this time scale can be resolved by the SPAD (see section 3.1.3), it is overshadowed by reflections of the excitation light and afterpulsing (see section 3.6.2). The initial rise of the $^5D_0 \rightarrow {}^7F_2$ emission is more apparent when zooming in at the first few microseconds (Fig. 3.33 b)). The decay of the PL intensity from both initial states $^5D_0$ and $^5D_1$ of the [Eu(tta)$_3$(H$_2$O)$_2$] samples is comparable to [Eu(tta)$_3$(bpy)] (Fig. 3.33 c and d)). [Eu(trensal-Ph-SMe)] shows a different characteristic (Fig. 3.34 a)). The intensity of the emission from the $^5D_0 \rightarrow {}^7F_2$ decreases faster than as observed in the samples of [Eu(tta)$_3$(bpy)] and [Eu(tta)$_3$(H$_2$O)$_2$]. From Fig. 3.34 b), it becomes apparent that the intensity from the $^5D_0 \rightarrow {}^7F_2$ transition declines on a similar timescale as the emission from $^5D_1 \rightarrow {}^7F_1$ and $^5D_1 \rightarrow {}^7F_2$ and lacks the initial increase. In [Eu(TACN)] (Fig. 3.34 c) and d)), the overall PL signal is even lower than in the [Eu(trensal-Ph-SMe)] sample but the initial increase in the intensity from the $^5D_0 \rightarrow {}^7F_2$ transition is present. Furthermore in comparison to the betadiketonate samples, the intensity of the decaying signal of the $^5D_0 \rightarrow {}^7F_2$ transition is closer to the signal from the $^5D_1 \rightarrow {}^7F_{1,2}$ transitions in the [Eu(trensal)] sample as can be seen for $t \rightarrow 0$. This indicates a higher ratio of $^5D_1/^5D_0$ emission, which is confirmed by the PL spectra (see section 3.6.1, Fig. 3.28). In the thin film of [Eu(tta)$_3$(bpy)] on Ag(111), the initially increasing intensity of the $^5D_0 \rightarrow {}^7F_2$ emission is also present (Fig. 3.34 e) and f)). Comparing the emission of the different samples on the short time scale reveals that the decay of the $^5D_1 \rightarrow {}^7F_1$ and $^5D_1 \rightarrow {}^7F_2$ is not always sufficiently described by a single exponential function.

To analyze the data quantitatively, it was fitted with a sum of exponential functions in the form of $\sum_i A_i exp(x/\tau_i)$. Where A_i describe the amplitudes and τ_i the decay constants which are synonymous to the observed lifetimes. Depending on the characteristics of the data either a single exponential function or the sum of two to four functions was fitted. The initial increase in intensity in the emission from the $^5D_0 \rightarrow {}^7F_2$ transition can be described by a negative amplitude which is then denoted as A_{rise} with a corresponding decay constant τ_{rise}. The fit parameters are listed in tables 3.4, 3.5, 3.6 and 3.7. The variances of the fit parameters are rounded to the first or second non-zero digit. The fit parameters are rounded according to their variance.

While the exact value of τ_{rise} (table 3.4) strongly depends on the experimental details, the order of magnitude is in agreement with literature [112, 115, 128, 129]. For all samples, τ_{rise} is slightly higher than the decay constants $\tau_{i,{}^5D_1}$ of the $^5D_1$ state except for the thin film of [Eu(tta)$_3$(bpy)] where the $^5D_1$ decays cannot be described by a single exponential function. There τ_{rise} is larger than the first decay constant and smaller than the second. τ_{rise} being larger than $\tau_{i,{}^5D_1}$ indicates that energy is transferred to the $^5D_0$ state at a rate lower than the

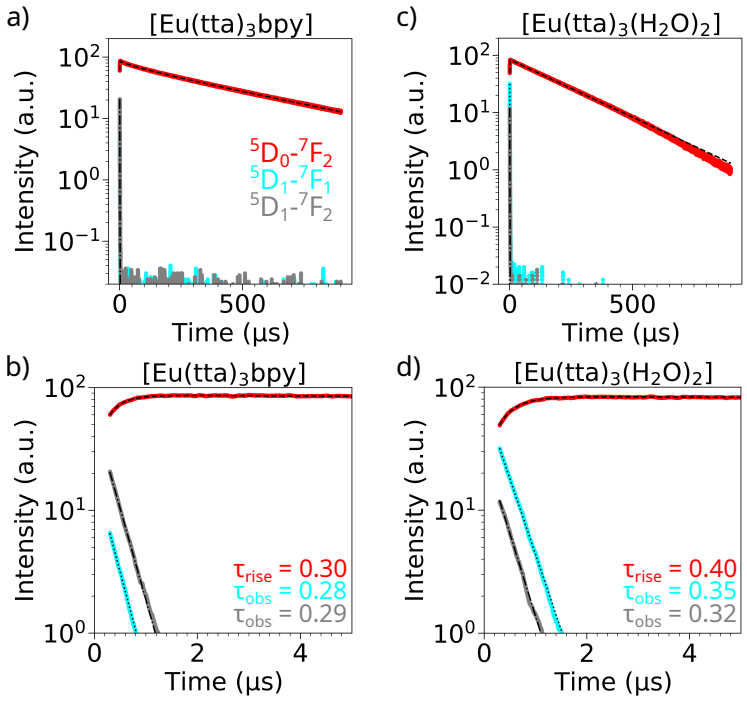

Figure 3.33: Rise time and decay of the PL intensity of the $^5D_1 \rightarrow {}^7F_1$ (cyan), $^5D_1 \rightarrow {}^7F_2$ (gray) and $^5D_0 \rightarrow {}^7F_2$ (red) transitions in different powder samples at room temperature at long and short time scales. The data was fitted with exponential functions (dashed lines).

decay rate of the $^5D_1$ state. This is a strong indication that the $^5D_0$ state is mostly populated by the $^5D_1 \rightarrow {}^5D_0$ transition. In the powder samples of [Eu(tta)$_3$(bpy)], [Eu(tta)$_3$(H$_2$O)$_2$] and [Eu(TACN)] the emission from both $^5D_1$ transitions decays with nearly identical time constants, as expected. In the powder sample of [Eu(trensal-Ph-SMe)] and the thin film of sublimed [Eu(tta)$_3$(bpy)] the $^5D_1$ decays cannot be described by single exponential functions (see section 2.5). While the same decay constants for both transitions starting from $^5D_1$ are still expected when several de-excitation processes are involved, the fitting process is more ambiguous. However, even for these samples the decay constants of both $^5D_1$ transitions match pairwise with only minor deviations. The losses of the energy transfer pathways within the Eu^{3+} ion can be estimated by the ratio of $\tau_{i,{}^5D_1}$ and τ_{rise}. τ_{rise} being significantly larger than $\tau_{i,{}^5D_1}$ would indicate that $\tau_{i,{}^5D_1}$ is dominated by transitions that are not leading to the population of the $^5D_0$ state. This ratio is in the range of 85 - 95 % for all three powder samples that allowed to determine τ_{rise}. Assuming EL follows the same excitation pathway the method of estimating these losses might give an indication which complexes are most promising which is especially useful since EL measurements can be tedious and time consuming. In fact, [Eu(tta)$_3$(bpy)] and [Eu(tta)$_3$(H$_2$O)$_2$], that are known to exhibit a strong PL signal, both have a τ_{rise} of less than half a microsecond, which is very close to the decay time of their $^5D_1$ state. The luminescence dynamics of the betadiketonate complexes are in contrast to the platform complexes [Eu(TACN)] and [Eu(trensal-Ph-Sme)]. [Eu(trensal-Ph-Sme)] does not show any observable rise time. For the sample of [Eu(TACN)], τ_{rise} and

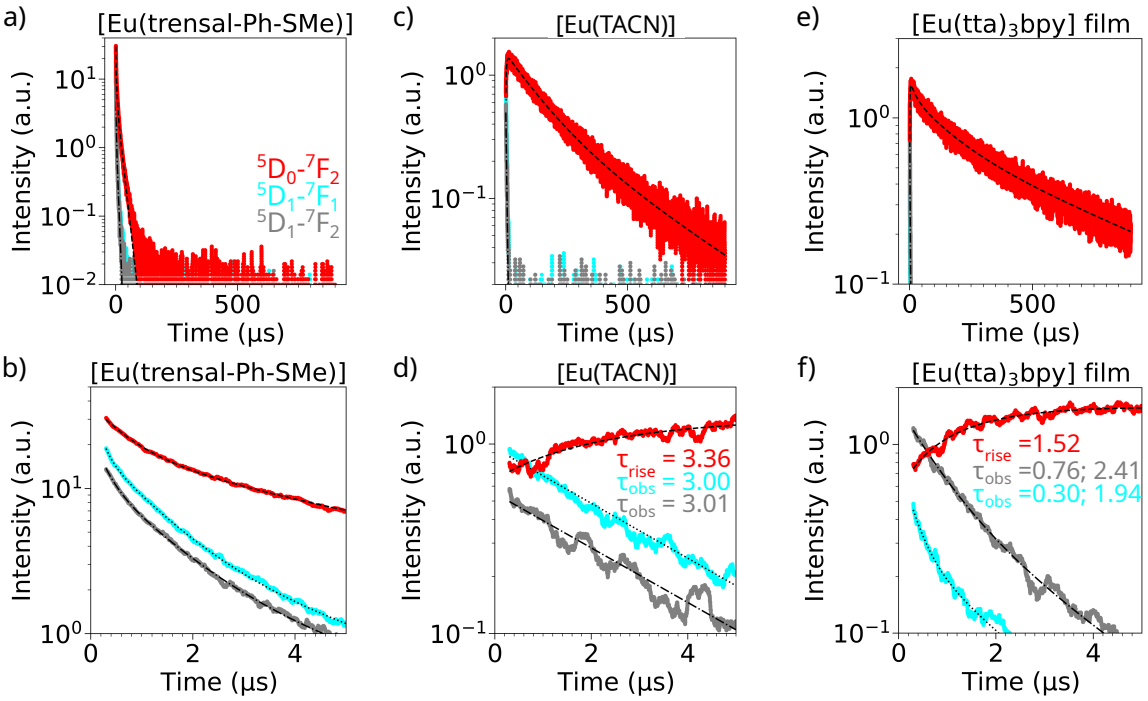

Figure 3.34: Rise time and decay of the PL intensity of the $^5D_1 \rightarrow {}^7F_1$ (cyan), $^5D_1 \rightarrow {}^7F_2$ (gray) and $^5D_0 \rightarrow {}^7F_2$ (red) transitions in powder samples of [Eu(trensal-Ph-SMe)] and [Eu(TACN)] at room temperature and a 21 nm thick film of [Eu(tta)$_3$(bpy)] sublimed on Ag(111) at room temperature at long and short time scales. The data was fitted with exponential functions (dashed lines).

$\tau_{i,^5D_1}$ are about ten times higher than for [Eu(tta)$_3$(bpy)] and [Eu(tta)$_3$(H$_2$O)$_2$]. This implies a less efficient $^5D_1 \rightarrow {}^5D_0$ transition pathway, ultimately leading to a higher $^5D_1/^5D_0$ emission ratio.

For all samples, the $^5D_0$ is characterized by up to three decay constants on different time scales, roughly in the ranges of ten, hundred and several hundred µs for most samples. [Eu(tta)$_3$(H$_2$O)$_2$] deviates by having one dominant decay at 215 µs. This might arise from the inherent quenching by OH-vibrations. It should be noted that the dominant decay in the [Eu(tta)$_3$(H$_2$O)$_2$] sample is in agreement with what we reported earlier [52], while the powder sample and the sublimed film of [Eu(tta)$_3$(bpy)] differ. The smaller decay constant in the powder sample is most likely due to the shorter measurement window, while the higher decay constant in the thin film might be caused by performing the measurement in vacuum and at 4.5 K.

The PL intensity of a transition is not only impacted by τ_{rad} but also depends on the intensity of the excitation signal, the sensitization efficiency, the losses on the pathway leading to the population of the emitting state and the detection efficiency. The amount of complexes contributing to the PL signal can be derived by the amplitudes A_i of the exponential

Sample	Transition	τ_{rise} (µs)	τ_1 (µs)	τ_2 (µs)	τ_3 (µs)
[Eu(tta)$_3$bpy]	$^5D_1 \rightarrow {}^7F_1$		0.27536		
[Eu(tta)$_3$bpy]	$^5D_1 \rightarrow {}^7F_2$		0.292086		
[Eu(tta)$_3$bpy]	$^5D_0 \rightarrow {}^7F_2$	0.30135	21.98	137.14	532.23
[Eu(TACN)]	$^5D_1 \rightarrow {}^7F_1$		2.9961		
[Eu(TACN)]	$^5D_1 \rightarrow {}^7F_2$		3.0147		
[Eu(TACN)]	$^5D_0 \rightarrow {}^7F_2$	3.356	125.35	336.70	
[Eu(tta)$_3$bpy] film	$^5D_1 \rightarrow {}^7F_1$		0.300	1.939	
[Eu(tta)$_3$bpy] film	$^5D_1 \rightarrow {}^7F_2$		0.758	2.407	
[Eu(tta)$_3$bpy] film	$^5D_0 \rightarrow {}^7F_2$	1.5157	23.36	153.4	687.4
[Eu(trensal-Ph-SMe)]	$^5D_1 \rightarrow {}^7F_1$		0.15663	1.0380	4.2510
[Eu(trensal-Ph-SMe)]	$^5D_1 \rightarrow {}^7F_2$		0.2445	1.1784	4.946
[Eu(trensal-Ph-SMe)]	$^5D_0 \rightarrow {}^7F_2$		0.6475	3.4573	13.91
[Eu(tta)$_3$(H_2O)$_2$]	$^5D_1 \rightarrow {}^7F_1$		0.352951		
[Eu(tta)$_3$(H_2O)$_2$]	$^5D_1 \rightarrow {}^7F_2$		0.32331		
[Eu(tta)$_3$(H_2O)$_2$]	$^5D_0 \rightarrow {}^7F_2$	0.39975	0.008	215.7579	

Table 3.4: Decay times (τ, [τ]=µs) for the $^5D_1 \rightarrow {}^7F_1$, $^5D_1 \rightarrow {}^7F_2$ and $^5D_0 \rightarrow {}^7F_2$ transitions as obtained by fitting a single or a sum of exponential functions for powder samples and in a film of 22.5 molecules/nm^2 thickness on Ag(111) at 4.5 K. τ_{rise} is the rise time of the initial increase in the intensity of the $^5D_0 \rightarrow {}^7F_2$ transition.

Sample	Transition	$\sigma^2(\tau_{\text{rise}})$	$\sigma^2(\tau_1)$	$\sigma^2(\tau_2)$	$\sigma^2(\tau_3)$
[Eu(tta)$_3$bpy]	$^5D_1 \rightarrow {}^7F_1$		0.00004		
[Eu(tta)$_3$bpy]	$^5D_1 \rightarrow {}^7F_2$		0.000027		
[Eu(tta)$_3$bpy]	$^5D_0 \rightarrow {}^7F_2$	0.00026	0.035	0.12	0.05
[Eu(TACN)]	$^5D_1 \rightarrow {}^7F_1$		0.0018		
[Eu(TACN)]	$^5D_1 \rightarrow {}^7F_2$		0.0032		
[Eu(TACN)]	$^5D_0 \rightarrow {}^7F_2$	0.004	0.22	1.01	
[Eu(tta)$_3$bpy] film	$^5D_1 \rightarrow {}^7F_1$		0.007	0.023	
[Eu(tta)$_3$bpy] film	$^5D_1 \rightarrow {}^7F_2$		0.006	0.023	
[Eu(tta)$_3$bpy] film	$^5D_0 \rightarrow {}^7F_2$	0.0034	0.10	0.5	1.4
[Eu(trensal-Ph-SMe)]	$^5D_1 \rightarrow {}^7F_1$		0.00033	0.0006	0.0038
[Eu(trensal-Ph-SMe)]	$^5D_1 \rightarrow {}^7F_2$		0.0004	0.0010	0.006
[Eu(trensal-Ph-SMe)]	$^5D_0 \rightarrow {}^7F_2$		0.0004	0.0024	0.007
[Eu(tta)$_3$(H_2O)$_2$]	$^5D_1 \rightarrow {}^7F_1$		0.000025		
[Eu(tta)$_3$(H_2O)$_2$]	$^5D_1 \rightarrow {}^7F_2$		0.00005		
[Eu(tta)$_3$(H_2O)$_2$]	$^5D_0 \rightarrow {}^7F_2$	0.00027	$< 10^{-16}$	0.0027	

Table 3.5: Variance of the decay times ($\sigma^2(\tau)$), [$\sigma(\tau)$]=µs) for the $^5D_1 \rightarrow {}^7F_1$, $^5D_1 \rightarrow {}^7F_2$ and $^5D_0 \rightarrow {}^7F_2$ transitions as obtained by fitting a single or a sum of exponential functions for powder samples and in a film of 22.5 molecules/nm^2 thickness on Ag(111) at 4.5 K. τ_{rise} is the rise time of the initial increase in the intensity of the $^5D_0 \rightarrow {}^7F_2$ transition.

Sample	Transition	A_{rise}	A_1	A_2	A_3
[Eu(tta)$_3$bpy]	$^5D_1 \rightarrow {}^7F_1$		19.36		
[Eu(tta)$_3$bpy]	$^5D_1 \rightarrow {}^7F_2$		57.27		
[Eu(tta)$_3$bpy]	$^5D_0 \rightarrow {}^7F_2$	−73.81	4.586	12.94	69.58
[Eu(TACN)]	$^5D_1 \rightarrow {}^7F_1$		0.94882		
[Eu(TACN)]	$^5D_1 \rightarrow {}^7F_2$		0.54928		
[Eu(TACN)]	$^5D_0 \rightarrow {}^7F_2$	−0.8518	1.0078	0.4903	
[Eu(tta)$_3$bpy] film	$^5D_1 \rightarrow {}^7F_1$		0.554	0.287	
[Eu(tta)$_3$bpy] film	$^5D_1 \rightarrow {}^7F_2$		1.038	0.553	
[Eu(tta)$_3$bpy] film	$^5D_0 \rightarrow {}^7F_2$	−1.1470	0.3123	0.6163	0.7602
[Eu(trensal-Ph-SMe)]	$^5D_1 \rightarrow {}^7F_1$		23.01	16.398	3.371
[Eu(trensal-Ph-SMe)]	$^5D_1 \rightarrow {}^7F_2$		11.836	10.922	1.936
[Eu(trensal-Ph-SMe)]	$^5D_0 \rightarrow {}^7F_2$		19.06	13.63	5.499
[Eu(tta)$_3$(H$_2$O)$_2$]	$^5D_1 \rightarrow {}^7F_1$		74.545		
[Eu(tta)$_3$(H$_2$O)$_2$]	$^5D_1 \rightarrow {}^7F_2$		30.436		
[Eu(tta)$_3$(H$_2$O)$_2$]	$^5D_0 \rightarrow {}^7F_2$	−74.78	0.74	84.537	

Table 3.6: Amplitudes (A) for the $^5D_1 \rightarrow {}^7F_1$, $^5D_1 \rightarrow {}^7F_2$ and $^5D_0 \rightarrow {}^7F_2$ transitions as obtained by fitting a single or a sum of exponential functions for powder samples and in a film of 22.5 molecules/nm^2 thickness on Ag(111) at 4.5 K. A_{rise} is the amplitude of the initial increase in the intensity of the $^5D_0 \rightarrow {}^7F_2$ transition.

Sample	Transition	$\sigma^2(A_{\text{rise}})$	$\sigma^2(A_1)$	$\sigma^2(A_2)$	$\sigma^2(A_3)$
[Eu(tta)$_3$bpy]	$^5D_1 \rightarrow {}^7F_1$		0.005		
[Eu(tta)$_3$bpy]	$^5D_1 \rightarrow {}^7F_2$		0.008		
[Eu(tta)$_3$bpy]	$^5D_0 \rightarrow {}^7F_2$	0.09	0.004	0.006	0.009
[Eu(TACN)]	$^5D_1 \rightarrow {}^7F_1$		0.00037		
[Eu(TACN)]	$^5D_1 \rightarrow {}^7F_2$		0.00037		
[Eu(TACN)]	$^5D_0 \rightarrow {}^7F_2$	0.0008	0.0028	0.0029	
[Eu(tta)$_3$bpy] film	$^5D_1 \rightarrow {}^7F_1$		0.011	0.004	
[Eu(tta)$_3$bpy] film	$^5D_1 \rightarrow {}^7F_2$		0.008	0.009	
[Eu(tta)$_3$bpy] film	$^5D_0 \rightarrow {}^7F_2$	0.0016	0.0007	0.0012	0.0019
[Eu(trensal-Ph-SMe)]	$^5D_1 \rightarrow {}^7F_1$		0.08	0.005	0.005
[Eu(trensal-Ph-SMe)]	$^5D_1 \rightarrow {}^7F_2$		0.017	0.006	0.004
[Eu(trensal-Ph-SMe)]	$^5D_0 \rightarrow {}^7F_2$		0.006	0.005	0.005
[Eu(tta)$_3$(H$_2$O)$_2$]	$^5D_1 \rightarrow {}^7F_1$		0.007		
[Eu(tta)$_3$(H$_2$O)$_2$]	$^5D_1 \rightarrow {}^7F_2$		0.007		
[Eu(tta)$_3$(H$_2$O)$_2$]	$^5D_0 \rightarrow {}^7F_2$	0.06	1.5^{-15}	0.0007	

Table 3.7: Variance of the amplitudes ($\sigma^2(A)$) for the $^5D_1 \rightarrow {}^7F_1$, $^5D_1 \rightarrow {}^7F_2$ and $^5D_0 \rightarrow {}^7F_2$ transitions as obtained by fitting a single or a sum of exponential functions for powder samples and in a film of 22.5 molecules/nm^2 thickness on Ag(111) at 4.5 K. A_{rise} is the amplitude of the initial increase in the intensity of the $^5D_0 \rightarrow {}^7F_2$ transition.

functions describing the decay over time. These amplitudes and their variance are listed in tables 3.6 and 3.7.

For each sample, the amplitude of each decay process was divided by the sum of all amplitudes, excluding A_{rise}. These ratios were then plotted with the corresponding decay constant (Fig. 3.35) displaying the contributions of the different decay channels to the overall PL decay. For the powder samples of $[Eu(tta)_3(bpy)]$ and $[Eu(tta)_3(H_2O)_2]$ (Fig. 3.35 a) and b)) that show a strong PL intensity, most of the signal stems from decays with long τ_{obs} in the range of several hundred µs. The $[Eu(tta)_3(bpy)]$ sample has some minor contributions of faster decay processes while $[Eu(tta)_3(H_2O)_2]$ is completely dominated by the decay at 216 µs. This is in contrast to the powder samples of [Eu(trensal-Ph-SMe)] and [Eu(TACN)] (Fig. 3.35 c) and d)). Here, most of the PL signal consists of decays with short decay constants and contributions from larger τ_{obs} are only minor. The thin film of sublimed $[Eu(tta)_3(bpy)]$ shows larger contributions from faster decay processes than the powder sample of $[Eu(tta)_3(bpy)]$ which is expected due to the additional de-excitation pathways provided by the substrate and a higher radiative transition rate upon sublimation (see section 3.6.4).

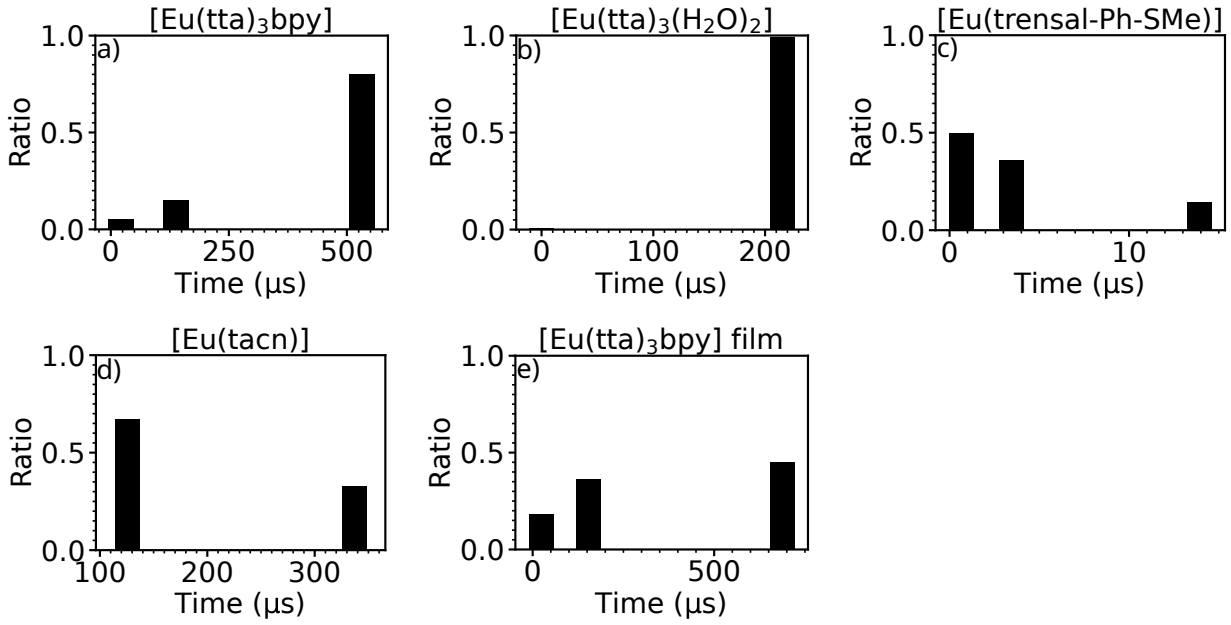

Figure 3.35: Relative proportion of the decay constants for different samples. The decay of the $^5D_0 \rightarrow {}^7F_2$ transition was fitted with a sum of exponential functions. For each exponential function the ratio of its amplitude to the sum of all amplitudes excluding the initial rise is plotted against the corresponding decay time.

Summary and discussion

In this section, TCSPC measurements of betadiketonate and platform complexes in powder were presented. Investigating the PL decay at 540 ± 10, 560 ± 10 and 610 ± 10 nm allowed

to determine the luminescence dynamics of the first and second electronic states of Eu^{3+}, $^5D_0$ and $^5D_1$. While the $^5D_1$ state decays immediately after excitation within the resolution given by the SPADs, the PL intensity of the $^5D_0$ state increases at first for many samples as a result of the competing processes of the $^5D_1 \rightarrow {}^5D_0$ transition and the $^5D_0$ decay. Fitting this initial rise in the PL signal and the following decay allows to quantify the dynamics of energy transfer within the Eu^{3+} ion. This confirmed that the energy is transferred from the ligands contained in the Eu^{3+} complex to higher excited states first, which then populate the $^5D_0$ state by vibronic relaxation.

It was furthermore demonstrated that information on processes on different timescales contributing to the de-excitation can be obtained by fitting a sum of exponential functions to the PL decay. This allows to deconvolve the contributions of these different processes.

3.6.6 Photophysical properties of [Eu(tta)3(bpy)] on metal as a function of film thickness

Quite some effort was put in enabling the controlled deposition of complexes on substrates via sublimation as detailed in section 3.2.2 and 3.3. This allows to grow films with precise thicknesses on metal substrates which is fundamental to investigate the energy transfer from the molecule to the metal as will be discussed in this section. These results were published in [168].

Samples of $[Eu(tta)_3(bpy)]$ films with different thicknesses were prepared by sublimation on Ag(111). $[Eu(tta)_3(bpy)]$ was chosen due to its strong PL emission and controlled sublimation characteristic. The $[Eu(tta)_3(bpy)]$ material was available as crumbs which is found to sublime in a more stable manner in comparison to powder. The material was degassed in the crucible at 150 °C for at least 10 h. The samples were prepared by sublimation at a crucible temperature of 185 °C with sublimation times between $\sim$ 1.5 and 10.25 min to obtain films with a coverage ranging between 3 and 15 molecules/nm^2, as callibrated with the quartz crystal micro balance. The film thickness can then be approximated when the density of the sublimed material and the area of the quartz crystal are known. Assuming a density of 1.7 g·cm^{-3} for $[Eu(tta)_3(bpy)]$ [173], this corresponds to film thicknesses in the range of 2.8 to 14.1 nm. The deposition rate was carefully callibrated each time to ensure a precise film thickness. At a crucible temperature of 185 °C, the deposition rate as monitored with the quartz crystal microbalance was around zero before opening the shutter and rose steadily after opening the shutter, as expected.

PL was measured on each sample (Fig. 3.36 a)) using set-up B (see section 3.1.3, Fig. 3.3). For excitation, a 375 nm light source was used. The autofluorescence background was subtracted and the spectra normalized to the $^5D_0 \rightarrow {}^7F_1$ transition. It is apparent that the ratio of the emission from induced ED transitions and the emission from the MD transition decreases with decreasing film thickness. This can be explained by the difference in electric and magnetic dipole transitions as discussed in section 2.4.2. For the modes of an electromagnetic field with wavevector normal to a metal surface, the electric field has a node

while the magnetic field has a maximum at the surface. For this reason, the optical set-up which detects light mostly perpendicular to the surface, favors light from magnetic dipole transitions. PL spectra from Eu^{3+} complexes are usually normalized to the MD allowed $^5D_0 \rightarrow {}^7F_1$ transition, since it is comparably insensitive to environmental changes (see section 2.6). However, the presence of the metal surface changes the radiation patterns of ED and MD emissions differently, leading to a relative decrease of the induced ED transitions. For this reason JO analysis is not valid for Eu^{3+} complexes on metal substrate. In the thickest film with 14.1 nm, the most intense emission stems from the $^5D_0 \rightarrow {}^7F_2$ transition around 610 nm, as expected for Eu^{3+}. However, in the thinnest film of 2.8 nm, the intensity of the $^5D_0 \rightarrow {}^7F_2$ transition is even smaller than the $^5D_0 \rightarrow {}^7F_1$ MD transition at ~ 590 nm.

TCSPC was measured on each sample at 4.5 K using the same set-up. A single 30 ps light pulse with $\lambda = 375$ nm was used for excitation. The PL decay was fitted with a single exponential to obtain a single average lifetime for each film thickness (Fig. 3.36 b)). The lifetimes drastically decrease with decreasing film thickness. Fitting the thickness dependent lifetimes $\tau(d)$ with a power law according to $\tau(d) = c \cdot d^m$ where d denotes the film thickness in nm, c the offset on the y-axis and m the potential growth, results in $\tau(d) = (62 \pm 37\,\text{ns}) \cdot \{d\}^{2.88\pm0.31}$. $\{d\}$ indicates the value of d without dimension. The observed decay rate therefore scales according to $\gamma_{\text{obs}} \propto d^{-2.88\pm0.31}$. This cubic dependence is in good agreement with the energy transfer rate of a dipole to a metal surface [46, 49, 80, 82, 83] (see section 2.4.2, Eq. 2.19).

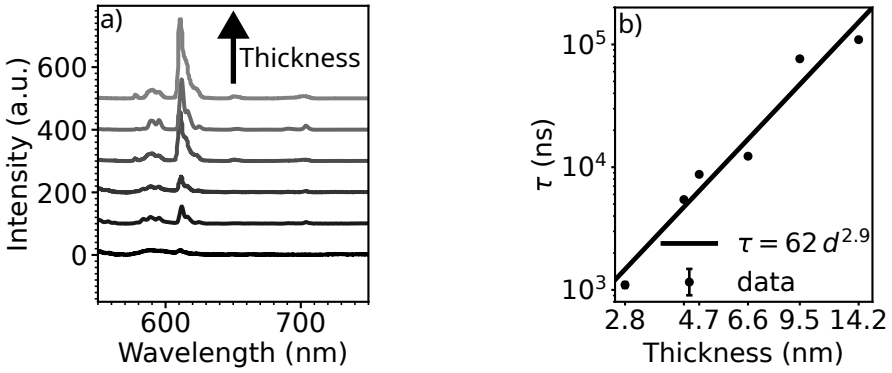

Figure 3.36: PL spectra and lifetimes of $[Eu(tta)_3(bpy)]$ films with different thicknesses on Ag(111) at 4.5 K. a) PL spectra of $[Eu(tta)_3(bpy)]$ films with thicknesses in the range of 2.8 to 14.1 nm. The autofluorescence background of the PL signal was subtracted and all spectra normalized to the $^5D_0 \rightarrow {}^7F_1$ transition. Spectra shifted for clarity. (Excitation with $\lambda = 375$ nm). b) Observed lifetime obtained by fitting a single exponential to the PL decay at 610 ± 10 nm of the samples with different thicknesses. For the TCSPC measurements, the samples were excited with a single 30 ps pulse, $\lambda = 375$ nm. Adapted from [168].

Eq. 2.19 allows to compare the experimental decay data to the decay predicted for films

on metal, using the values obtained from JO theory for $[Eu(tta)_3(bpy)]$ in powder (see section 2.7, table 3.1) for $\gamma_{nonrad} = 550$ Hz and $\gamma_{rad} = 750$ Hz. The JO parameters for the powder sample were preferred over the parameters from the sublimed film since the latter are expected to be more sensible to the experimental procedure. The model was built by assuming the first layer of Eu^{3+} ions has a distance to the metal surface of 0.5 nm, which is roughly half the size of one complex. The distance then increases in increments of 0.1 nm until the film thickness minus 0.5 nm is reached. For each distance increment, the total decay rate γ_{obs} is calculated according to eq. 2.19 and the exponential decays for every increment summed up to obtain the total decay. A global factor accounts for the excitation and detection efficiency which corresponds to an offset on the logarithmic scale. Since the actual film growth is unknown, the model was evaluated for perfect 2D and 3D film growth. Perfect 2D film growth means, that the film is completely flat. For a perfect 3D growth, the film thickness follows a cumulative distribution function. The result is shown in Fig. 3.37. The experimental data is shown in red, the model for 2D and 3D film growth is indicated by the dashed black and blue graphs, respectively. The left and right columns show the same results on a short and a long timescale, respectively. The experimental data is well between the limits given by 2D and 3D growth. This does not indicate any major additional de-excitation channel, e.g. by charge transfer from the complex to the metal substrate.

Fitting the decay data for the samples allows to estimate the contribution of emitters at different distances. The data was fitted with a sum of exponential functions, each function corresponding to an emitter-metal distance increment starting at 0 going up to 20 nm in steps of 2 nm. Each exponential decay is described by a decay rate γ_{obs}, using Eq. 2.19. The resulting distance distribution is shown in Fig. 3.38. It should be pointed out that the film thickness derived with this method corresponds well with the expected thickness as calibrated with the quartz crystal microbalance during the sublimation process.

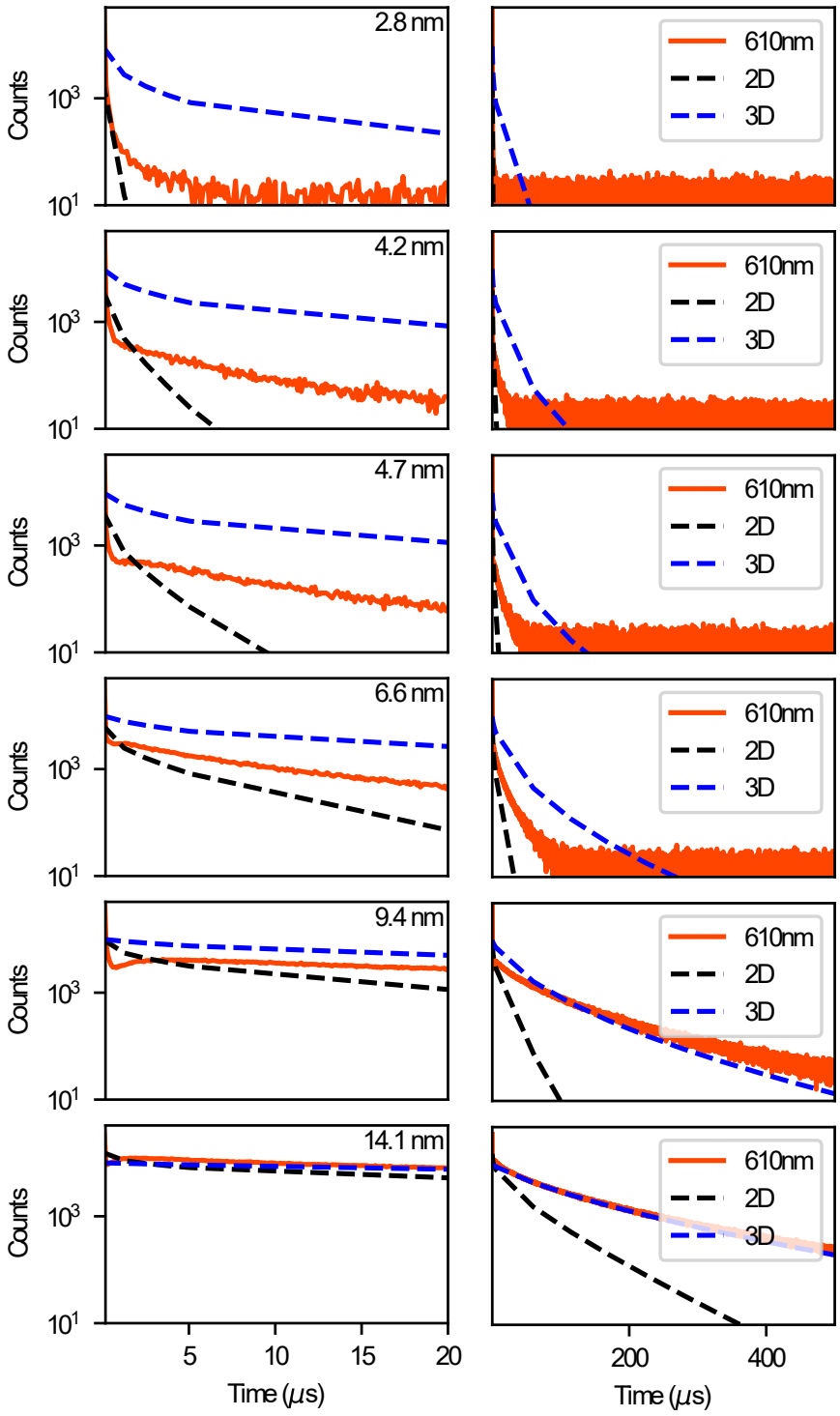

Figure 3.37: TCPSC measurement of $[Eu(tta)_3(bpy)]$ films with thicknesses between 2.8 to 14.1 nm on Ag(111) at 4.5 K. Left and right columns show the same data on short/large time scale, respectively. Red: TCSPC data, dashed black/blue line: expected distance dependent decay from dipole radiation dissipating into the metal for a perfect 2D/3D film growth, respectively. The data was recorded using a 610 ± 10 nm band-pass filter. The samples were excited with a single pulse of 30 ps, $\lambda = 375$ nm. Adapted from [168].

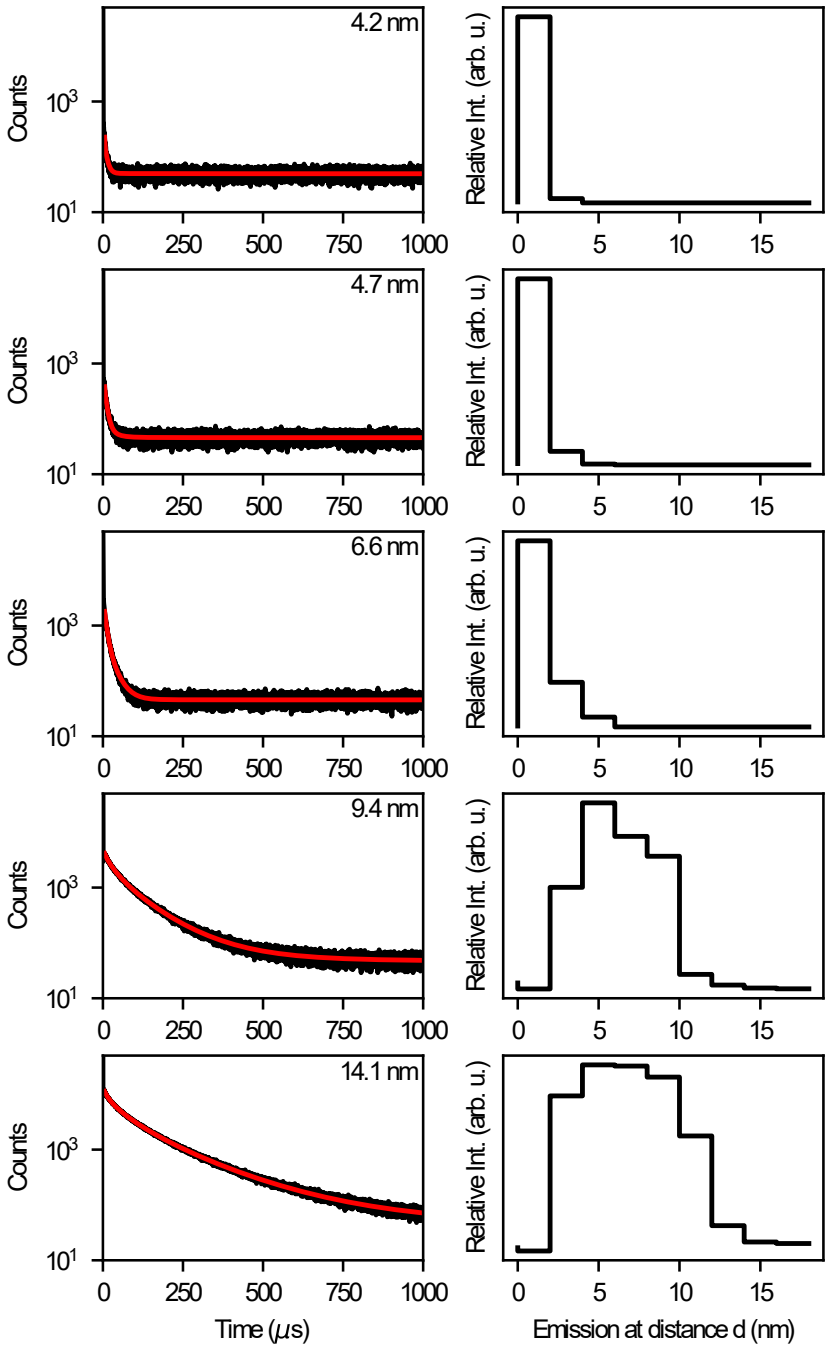

Figure 3.38: Fitted TCPSC data of $[Eu(tta)_3(bpy)]$ films with thicknesses between 4.7 and 14.1 nm on Ag(111) at 4.5 K. Left column: TCSPC data (black) with multi-exponential fits (red). Right columns: contribution to the PL signal of layers at different distances to the metal substrate as obtained from the fits. Adapted from [168].

Summary and discussion

The impact of a metal substrate on the luminescence of molecules was discussed in this section. PL and TCSPC was measured on thin film samples of $[Eu(tta)_3(bpy)]$ on Ag(111) with decreasing thicknesses down to 2.8 nm. The PL data shows a changing ratio of the induced ED and MD emission bands with film thickness. This was attributed to the different characteristics of the electric and magnetic modes of the electromagnetic field in proximity to a metal surface. The observed lifetime derived from TCSPC experiments show a cubic dependence on the film thickness. This is taken as a strong indication for the reduction in lifetime due to energy transfer to the metal as is known from literature. This is further supported by comparing my data to the according model. The experimental data is well between the limits given by perfect 2D and 3D film growths. The energy transfer to the metal surface is therefore considered the main mechanism reducing luminescence in the far field, while quenching due to efficient electron transport from molecule to the substrate is not necessary to describe the observed decays. Finally, deconvoluting the PL decay by fitting a sum of exponential functions reveals the contributions to the emission from molecules at different distances to the substrate. This confirms the preciseness of the sample preparation via sublimation in regard to film thickness.

4 Graphene nanoribbons

This chapter discusses the most significant findings during my 1.5 years of research at the University of Bayreuth. While some of the observations require more thorough investigations for a fundamental understanding, they continue the promising work done by the group of Prof. Enders connecting to the previous findings and extending current understanding.

Semiconductors are at the basis for most of our modern electronic devices. The most prominent use is the formation of a transistor. A device first thought of by J. E. Lilienfeld in 1925 that is able to control circuits electrically which in turn allows them to be organized in logical gates. Traditionally, silicon is used in semiconducting devices due to its electronic properties and suitable bandgap. However, the desire to downsize electronic devices, reduce production costs and opening up new application areas advances the research of semiconductors and pushes silicon devices to their limits. In recent years, many graphene based devices were reported [174], including field effect transistors [2, 3], as well as devices with applications in quantum electronics [21–23], spintronics [12, 24, 25] and optoelectronics [26–28].

Graphene consists of sp^2 hybridized carbon atoms [174] arranged in a two-dimensional, hexagonal lattice with a lattice constant of 246 pm [175]. Up until 2004 the fabrication of such a two-dimensional sheet was considered to be impossible - or at least very difficult, since it was regarded thermodynamically unstable. However, K. S. Novoselov et al. managed to fabricate two-dimensional graphene sheets as well as a field effect transistor made out of several layers of graphene by cleaving a highly ordered pyrolitic graphite (HOPG) crystal [4]. HOPG consists of many stacked layers of graphene that are bound via valence force, which is much weaker than the covalent bonds within the individual sheets. This allows to subsequently separate graphene sheets by the simple use of adhesive tape.

The electrons in the $2p_x$ and $2p_y$ orbitals form σ bonds, while the $2p_z$ orbitals form π bonds, leading to delocalized electrons in the π and π^* bands. The electrons in these bands form an electron gas, which makes graphene a highly conducting material. Looking at the dispersion in the Brillouin zone (Fig. 4.1), the semi metallic character is apparent. The conduction band and valence band touch only at the K and K' points, forming a Dirac cone. This implies that graphene is a zero bandgap semiconductor. Since the dispersion relation is linear in proximity to Dirac cones, the electrons can be treated as mass-less fermions [176], resulting in an exceptionally high charge carrier mobility.

A graphene sheet can be considered an extended π-electron system which allows the electrons to move freely along the plane of the sheet as an electron gas. When one dimension of the sheet is sufficiently reduced, the movement of the electron is confined in this direction

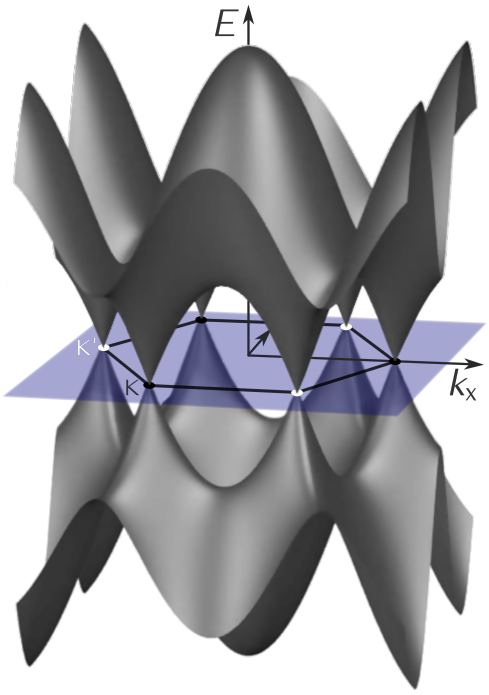

Figure 4.1: Dispersion of graphene in the 2d Brillouin zone. Valence band (VB) hosting electrons and conduction band (CB) hosting holes touch at the K and K' points thus forming dirac cones. From [177].

which leads to discrete energetic niveaus analogous to the quantum mechanical model of an electron confined in a potential well. The energetic separation between the first niveau above the Fermi energy (LUMO) and the last fully occupied niveau closest to the Fermi energy (HOMO) defines the bandgap. A strip of graphene with finite width in one direction is called a graphene nano ribbon (GNR). The width of GNRs is usually in the range of 4 to several 10 atoms. In reality, GNRs consist of a network of carbon atoms with significant confinement in at least one direction. They can therefore be considered as molecules. The bandgap of these molecules is inverse proportional to their width [8–10]. Several methods have been developed to tune this bandgap, making it suitable for electronic applications. These methods include modifying the width [8–11] and edge structure [12, 13] of the GNR, inducing porosity [17–20], or doping [15, 16].

4.1 Synthesis

While the first attempts to obtain GNRs relied on lithography for masking graphene with nanowires before edging [6] or unzipping carbon nano tubes [5], the bottom-up-approach developed by J. Cai et al. [7] allows to synthesize GNRs out of molecular building blocks called monomers. This opens the possibility to deposit monomers on a substrate and induce the synthesis by heating. There are different methods of depositing monomers onto the substrate as will be discussed in section 4.3.2. The synthesis of GNRs using the bottom-up-approach is depicted in Fig. 4.2. The idea behind this approach is to follow the Ullmann

reaction [178] by using monomers with two or more halogen atoms that can act as linkers. When energy is supplied to the monomers, usually in the form of heat ($\sim$ 200 °C), the halogen bonds break first. The so formed radicals allow the monomers to undergo polymerization. At this stage, the polymer consists of phenyl moieties attached to a backbone. The phenyl moieties are subject to interactions with their neighbors as well as interaction with the substrate. A second annealing step at a higher temperature ($\sim$ 400 °C) induces cyclodehydrogenation. This refers to the hydrogen-carbon bonds breaking, which leads to the formation of new bonds between the phenyl moieties, thus extending the delocalized π-electron system. These newly formed bonds force the phenyl rings to lie flat on the substrate, planarizing the molecule. Usually, the molecule is only referred to as a GNR after the cyclodehydrogenation and planarization step.

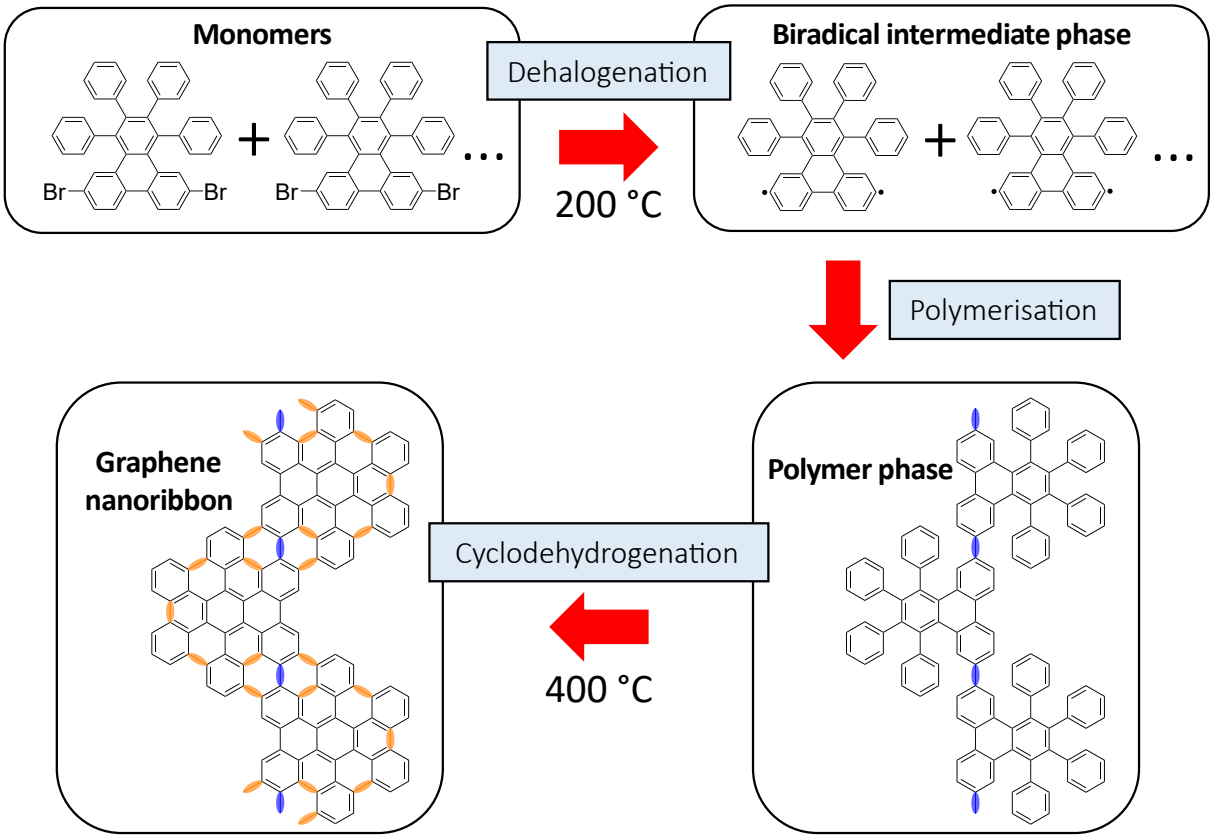

Figure 4.2: Synthesis scheme of the bottom-up-approach exemplary shown for chevron precursors with a 90° bonding angle (C90-precursors). Polymerization by dehalogenation and planarization by cyclodehydration are induced by heat. The bonds forming the polymer backbone after polymerization are highlighted in blue. The bonds planarizing the phenyl rings after cyclodehydrogenation are highlighted in orange.

4.2 Bandgap engineering

Modifying the bandgap of a material is crucial for its application in electronic devices. The bandgap of GNRs can be modified by changing the width of the ribbon [8–11], its edge structure [12–14], inducing porosity [17–20] or doping [15, 16]. The edge structure refers to the structure of the longer side of the ribbon. Some common shapes include chevron GNRs (C-GNRs), armchair GNRs (A-GNRs), and zigzag GNRs (z-GNRs). Fig. 4.3 illustrates how these GNR shapes relate to the hexagonal structure of the graphene lattice.

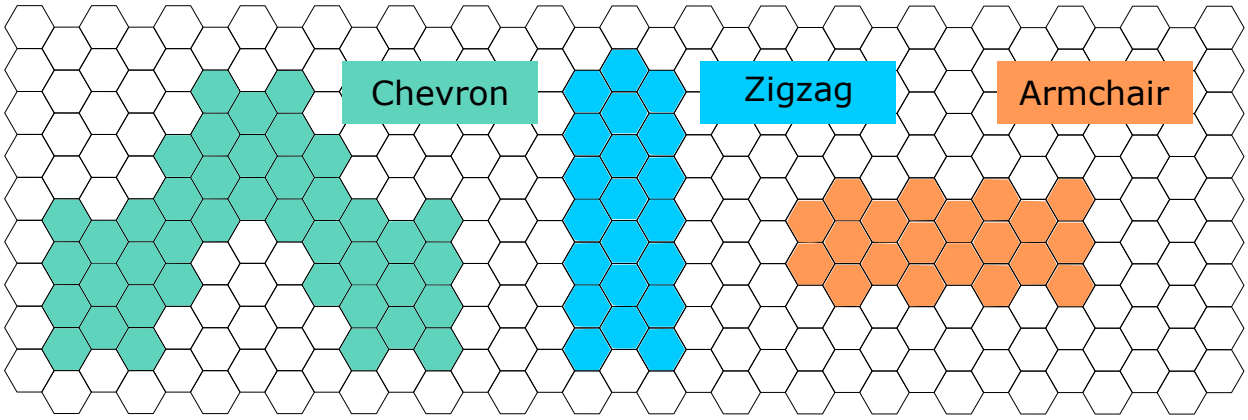

Figure 4.3: Illustration of different edge structures of GNRs relating to the graphene structure: chevron GNR (C-GNR), zigzag GNR (z-GNR) and armchair GNR (A-GNR).

The bandgap of A-GNRs is generally considered decreasing with its increasing width, until it disappears when transitioning to graphene sheets [8–11]. A-GNRs can be divided into three subgroups according to their width: 3n, 3n+1 and 3n+2. The integer n refers to the amount of C-C dimers across the width of the GNR. A-GNRs with a width of 3n and 3n+1 exhibit a bandgap while the group of 3n+2 have metallic character [179]. The size of the bandgap increases according to 3n+1 > 3n > 3n+2 [8, 11].

When projecting the 2d dispersion of A-GNRs onto the 1d Brillouin zone, the K and K' point are projected onto the Γ point which causes the Dirac cones at K and K' to meet at the center of the Brillouin zone [179, 180]. Depending on the momentum, A-GNRs can therefore be metallic or semiconducting. For Z-GNRs the edge runs along a different direction, which causes the K and K' points to be projected onto different points within the 1d Brillouin zone that are connected by a flat band at the Fermi level [179, 180]. For this reason, Z-GNRs are usually considered metallic. The flat band connecting the K and K' points causes localized edge-states exhibiting magnetic moments which makes Z-GNRs interesting for spintronic applications [12, 24, 25].

Porous GNRs can be synthesized by utilizing monomers with a halogen bonding angle of 30° instead of 90° [18–20, 33]. Since their bandgap is dominated by the porosity and not

the width, extended porous graphene sheets with a non zero bandgap might be possible. The importance of the halogen bonding angle is depicted in Fig. 4.4 showing how C-GNRs are formed by C90-precursors while fusing C30-precursors results in porous GNRs.

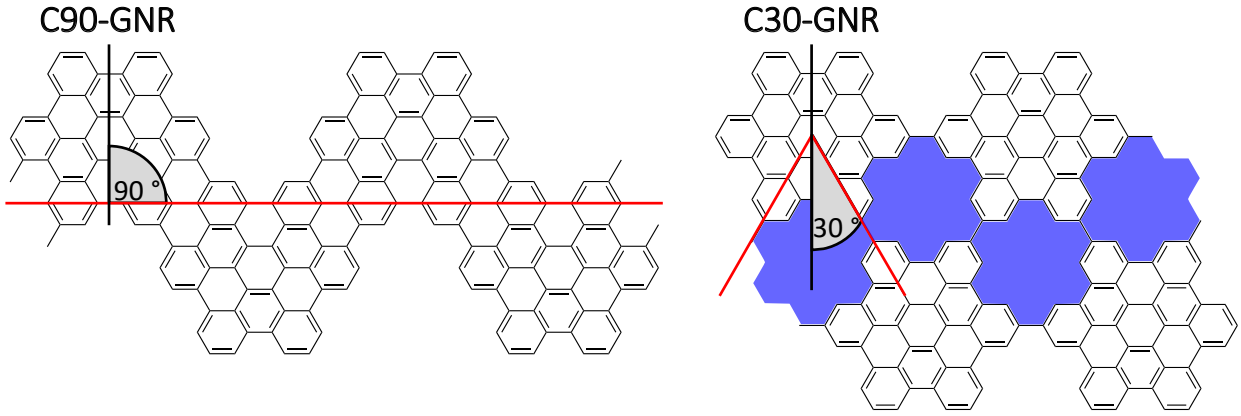

Figure 4.4: Illustration of the importance of the halogen bonding angle for the structure and porosity of the GNR. C90-precursors have a 90° halogen bonding angle, resulting in solid chevrons. C30-precursors feature a 30° halogen bonding angle, resulting in porous GNRs. The bonding angle refers to the angle between the bond formed by dehalogenation to the symmetry axis of the monomer.

4.3 Experimental set-up

In the following section, the experimental details for the work in the group of Prof. Axel Enders at the University of Bayreuth will be described, outlining the experimental set-up, sample preparation procedures and molecular material.

4.3.1 UHV set-up

The UHV set-up used for the experiments at the group of Prof. Axel Enders from the University of Bayreuth has already been discussed in great detail [33] and will only be described briefly here.

The UHV set-up consists of a load-lock chamber, a preparation chamber and an STM chamber separated by gate-valves. Initially, the instrument consisting of the STM chamber and the load-lock was bought from *Scienta Omicron* in 2007. It was later extended by the preparation chamber when the group of Prof. Axel Enders was still located at the University of Nebraska-Lincoln. The set-up was then disassembled and shipped to the University of Bayreuth by Dr. Christoph Dobner in 2019 who refurbished the set-up during his work as a PhD student. I then took over the set-up in 2022 only making minor modifications.

The load-lock attached to the preparation chamber is used to transfer samples into the UHV system and for preparing samples via direct contact transfer (DCT) (see section 4.3.2).

The load-lock is pumped by a rotary pump and a turbo-molecular pump. The preparation chamber is either pumped via a rotary pump and a turbo-molecular pump or via an ion getter pump. Additional TSP flashes help to decrease the pressure. The pressure in the preparation chamber is in the range of $10^{-8} - 10^{-9}$ mbar. A sputter gun (*Prevac, IS 40C1*) is attached to the preparation chamber for cleaning the sample via sputtering with Ar^+ ions. A manipulator attached to the preparation chamber allows to move the sample in the UHV system. Attached to the manipulator is a sample stage, equipped with a filament that allows heating the sample via electron bombardment. The STM chamber and the STM head are still mostly as purchased. A LN_2 bath cryostate is positioned on top of the STM-chamber. The STM head can be attached to the cryostate for good thermal contact or suspended by springs to reduce noise while measuring. The chamber is pumped via an ion getter pump and TSP flashes.

4.3.2 Sample preparation

Preparing a sample for STM measurements requires cleaning the substrate first and depositing molecules on top of it afterwards. For depositing molecules two methods were used, direct contact transfer (DCT) and electro-spray deposition (ESD). The cleaning process and the deposition methods are described in the following sections.

Substrate cleaning

As substrates, commercially purchased metal single crystals are used. Three cycles of sputtering and annealing in UHV conditions are usually sufficient for achieving a clean and flat surface. Sputtering is done by bombarding the surface with Ar^+ ions accelerated by 2.0 kV by the sputter gun. This is followed by annealing the sample to approximately 650 °C.

Direct contact transfer deposition

A very common method to deposit molecules on a substrate is sublimation. However, this requires knowing the sublimation temperature and thermal stability of the molecules. For this reason DCT [18, 29, 30, 33], also referred to as direct contact printing or stamping may be preferred. DCT is done by first spreading the powder of the molecules on a clean flat surface with a spatula. A stamp consisting of a *Kimtech precision wipe* attached to a metal holder is then tapped into the powder. The stamp is then attached to the transfer rod in the load-lock. After pumping the load-lock, and transferring the sample into it, the stamp is gently pushed against the edge of the substrate, applying some of the powder on the surface. Fig. 4.5 shows a substrate before and after depositing molecules on the edge. After stamping, the sample is transferred into the preparation chamber. The sample is heated gradually to temperatures around 450 K until the powder completely melts. Depositing the material at the edge of the substrate has two advantages: On the one hand, it minimizes damage to the crystal by the physical contact. On the other hand, it creates a reservoir of molecules on one side of the sample. Upon annealing, the molecules diffuse over the surface, creating a gradient of the coverage. This allows to investigate different coverages on the same sample. Furthermore, if stochiometric mixes of two molecular powders are applied,

the difference in diffusivity across different molecules may create a gradient in the ratio of these different molecules. This was exploited for creating heterostructures in the past [29, 33].

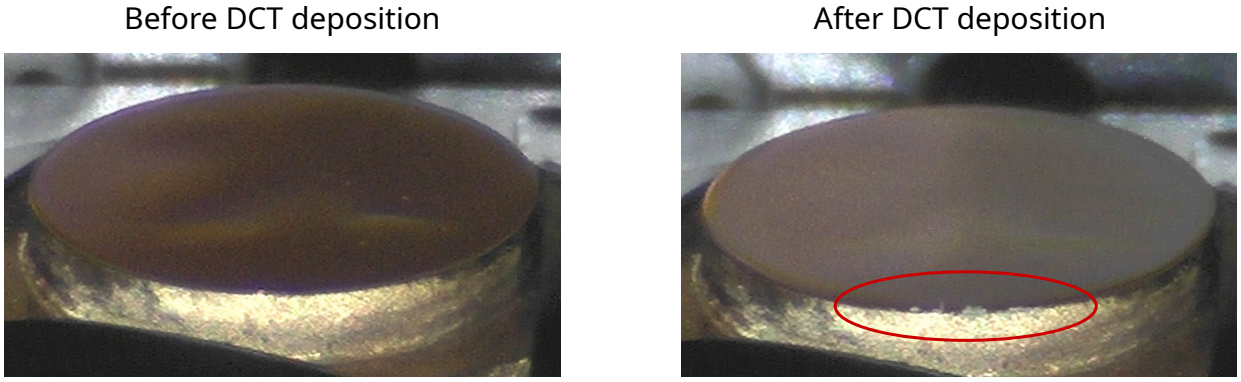

Figure 4.5: Pictures of a Au(111) substrate before and after depositing molecules via DCT at the edge of the crystal. The white powder of the molecules is highlighted by the red oval.

Electro-spray deposition

The set-up for ESD was built by Dr. Felix Baier [30] at the University of Bayreuth as part of his work as a PhD student. For depositing molecules on a substrate via ESD, they have to be dissolved in a suitable solution. The solution is then drawn up by a syringe and the syringe positioned in a syringe pump. High voltage is applied between the cannula of the syringe and the substrate which causes the solution to disperse into an aerosol when the syringe is squeezed due to coulombic repulsion. This fine aerosol consists of microdroplets with a size of several µm [30] that is accelerated towards the substrate. Spraying is done in a glove box with inert gas atmosphere. After spraying, the sample is transferred into the UHV set-up in a passive vacuum suitcase. The pressure within the vacuum suitcase goes up to 10^{-3} mbar during sample transfer [30]. Moderate annealing reduces possible contamination after the transfer.

4.3.3 Overview of GNR precursors

An overview of the precursors used for the on-surface synthesis of polymers and GNRs is provided in this section. The precursors are shown in Fig. 4.6 and their full names are listed below. The precursors were synthesized by Dr. Mamun Sarker at the University of Nebraska-Lincoln.

- **C30** [31–33]:
  Triphenylene, 7,10-dibromo-1,2,3,4-tetraphenyl- (ACI)
- **C30-4Br**:
  Triphenylene, 1,4-diphenyl-2,3-bis(4-bromophenyl)-7,10-dibromo- (ACI)

- **T30**: [18–20, 30, 33]
  Triphenylene, 7,10-dibromo-1,4-diphenyl- (ACI)
- **T90**:
  Triphenylene, 6,11-dibromo-1,4-diphenyl- (ACI)

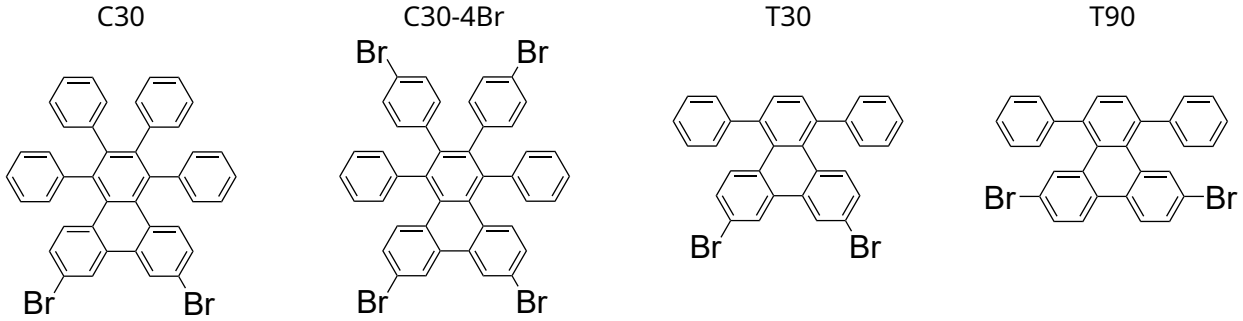

Figure 4.6: Structure drawings of GNR-precursors.

4.4 Self organization and electronic properties of GNRs

I started my work by reproducing the adsorption behavior of T90-polymers and T30-GNRs to verify the sample preparation procedure and functionality of the instrument. Furthermore, the difficulties in obtaining heterojunctions from the on-surface synthesis of molecules with 30° bonding angle are outlined. The main focus is put on the self-assembly of C30-4Br-precursors and GNR structures exhibiting different packing and characteristics depending on the coverage and sample preparation method.

4.4.1 T90 polymeric phase

The first precursors used for synthesizing GNRs via the bottom-up-approach featured a 90° bonding angle [7]. Choosing this angle allows to grow long and straight GNRs. For this reason, a 90° bonding angle was also used for growing C-GNRs from C90-precursors as well as truncated C-GNRs from T90-precursors by the group of Prof. Enders [33]. GNRs synthesized from T90-precursors are A-GNRs that are nine carbon atoms and posses phenyl-sized notches in regular distances along both edges. This unique structure has been shown to modify the band-gap [33]. Since T90-GNRs grow in long, well ordered chains they were used as a starting point to familiarize myself with the sample preparation before moving to new precursors. The polymeric phase of T90 is shown in Fig. 4.7. The sample was prepared by depositing T90-precursors via DCT on Au(111) followed by annealing. The temperature was slowly increased to 124 °C during a period of 20 min. The T90-polymers align in parallel due to the inter-molecular interaction, thus forming islands (Fig. 4.7 a)). In figure 4.7 b) the polymer backbone and the phenyl sites can be distinguished. The backbone has the same apparent height in the STM-topology image, indicating an extended π-electron system. However, there is a contrast between the backbone and the phenyl sites, which

means the phenyl rings are not planarized on the Au(111) surface and are not part of the delocalized π-electron system. The contrast between backbone and sites is a clear sign that cyclodehydrogenation did not yet take place and we are looking at the polymeric phase. The T90 islands follow the herringbone reconstruction (Fig. 4.7 c)) or align along step edges (Fig. 4.7 d)).

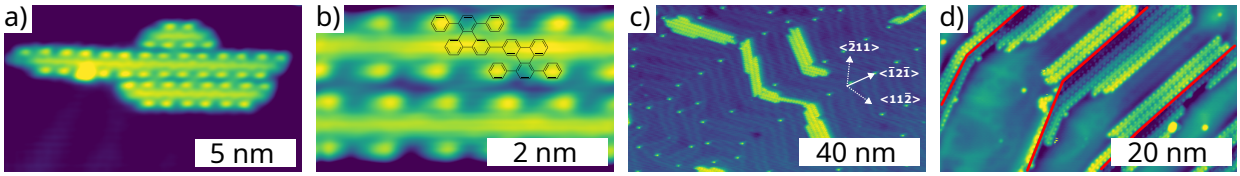

Figure 4.7: T90-polymers on Au(111). a) Polymers islands. (0.9 V, 1 nA). b) Close-up image of two adjacent polymers with assumed structure overlaid. (0.9 V, 1 nA). c) Polymer islands aligning with the herringbone reconstruction. (0.9 V, 300 pA) d) Polymer chains aligning along Au step edges indicated by red lines. (0.3 V, 300 pA).

4.4.2 T30-GNRs

T30-precursors are a variation of T90-precursors with the halogen atoms placed at a 30° instead of a 90° angle to the symmetry axis of the molecule (see Fig. 4.8 b)). This leads to A-GNRs featuring nano pores [18–20, 33] (Fig. 4.8 c)). To my knowledge, the growth and electronic properties of these molecules were first reported by the Enders group [18, 33]. For this reason, they were used as a starting point for the characteristics of molecules resulting from precursors with 30° halogen bonds. A sample was prepared via electro-spraying from a 1mg/10ml acetone solution. The solution was sprayed at a rate of 3 µl/min at a voltage of 3.4 kV for 10 min on a clean Au(111) crystal at room temperature in inert gas atmosphere. The sample was then annealed for 15 min in UHV after ramping the temperature up to 110 °C over a period of 18 min followed by annealing a second time for 23 min at 230 °C after ramping the temperature up over 23 min. The sample was transferred into the 77 K STM system in a vacuum suitcase and annealed shortly at 130 °C for less than one minute before taking STM measurements. This preparation resulted in a sample covered with close to one ML of T30-GNRs (Fig. 4.8 a)). The growth of the GNRs is hindered by defects but also by the halogens being placed at a 30° angle, which opens the possibility for dendritic growth. On this sample, the dendritic growth is mostly suppressed due to the high coverage in favor of ordered linear chains, that allow higher packing.

dI/dV maps of T30-GNRs are shown in Fig. 4.9. There are states localized at the pores of the GNR at 1.5 eV (Fig. 4.9 b)) that have been shown to form delocalized states when two or more T30-GNRs are laterally linked [18]. The differential conductance close to the Fermi energy at -0.1 V (Fig. 4.9 d)) shows vanishing conductance along the GNR. At this voltage, the dI/dV map shows comparatively high conductance within the pores and

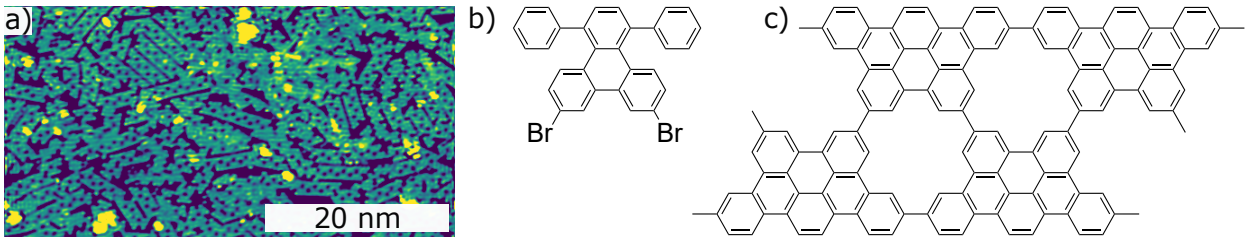

Figure 4.8: a) STM topography of T30-GNR growth on Au(111). (1.5 V, 300 pA). b) Structure of a T30-monomer. c) Structure of a T30-GNR.

along the edges of the GNRs which might arise from probing the underlying substrate [19], although significant differential conductance was reported for T30-GNRs at -0.27 V [33]. In contrast, the differential conductance at 0.7 V (Fig. 4.9 c)) is not entirely determined by the substrate but does also not show a strong indication of conductivity along the GNR. At -1.5 V (Fig. 4.9 e)), the differential conductance is highest along the π-electron system. While a state localized at the pores and along the edges at negative voltages was reported [19, 20], other findings conclude that the pore state only emerges when two or more GNRs are laterally fused [29]. My findings are more in line with the latter. The strong differential conduction at 1.5 V and -1.5 V are in agreement with literature [18–20, 33].

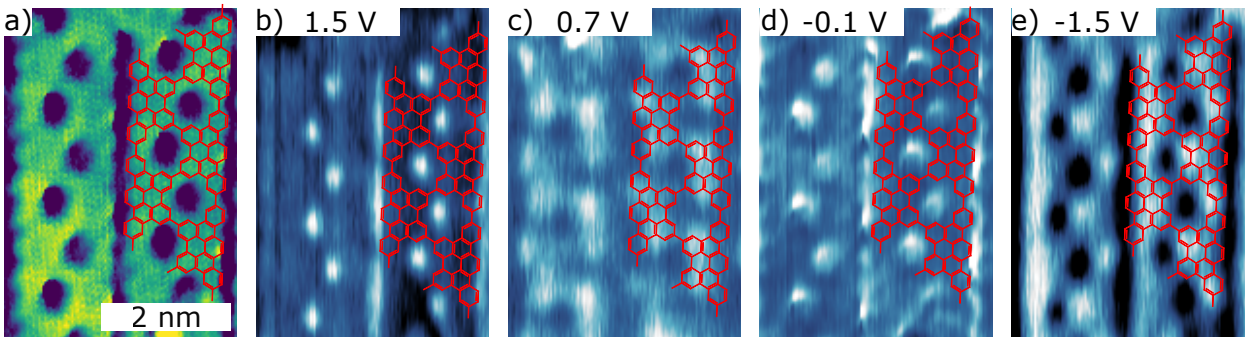

Figure 4.9: a) STM topography of two adjacent T30-GNRs. (-0.1 V, 1 nA). b) - e) corresponding dI/dV maps at different bias voltages. Depending on the bias voltage, the states are located at the pores (b), or at the delocalized electron system (e).

4.4.3 T30-C30-GNRs

A sample of T30-C30 heterostructure GNRs on Au(111) was prepared via DCT. The sample was annealed gradually to 127 °C over a period of 27 min to promote diffusion. It was then annealed gradually to 180 °C over 44 minutes to induce polymerization and cyclodehydrogenation. At high coverage close to 1 ML, the molecules align in chains with lengths of several ten nanometers therefore forming GNRs (Fig. 4.10 a)). At high coverage, the steric hinderance forces the molecules to pack into longer GNRs to increase the packing. These GNRs show the tendency to align in parallel in domains with 60° orientation to one another following the symmetry of the herringbone reconstruction (Fig. 4.10 a)). This is in agreement with previous work [33]. Fig. 4.10 b) shows a spot on the sample with low coverage

($\ll$ 1 ML) after annealing the sample again to 228 °C within 30 min to improve stability. In contrast to the long chains of GNRs at high coverage, the GNRs assemble into islands in areas with low coverage. The growth of these islands is of dendritic nature and hardly impacted by the herringbone reconstruction of the Au(111) surface.

Fig. 4.10 c) shows an isolated triangular molecule synthesized out of three C30-4Br-precursors. Although the formation of molecules with C3 symmetry seems obvious due to the 60° angle between the two halogen bonds, it is rarely observed on samples prepared by DCT [33]. Isolated GNRs at an area of low coverage show the tendency to follow the herringbone reconstruction of Au(111), as expected (Fig. 4.10 d)).

Since T30- and C30-precursor powders were mixed before the DCT-process, they are randomly distributed on the surface. The stochiometric ratio of T30- and C30-molecules does not change significantly across the surface of the substrate. This is in contrast to what was reported for samples of T90-C90-heterostructures [29], where the ratio of both molecules changed depending to the stamping area due to the different diffusivities of both molecules. It can be rationalized that the 30° bonding angle favors dendritic growth which induces an element of randomness. For this reason, finding a heterojunction is a matter of luck. Figure 4.10 e) displays a heterojunction with C30 at the top and T30 at the bottom. The corresponding dI/dV map at 0.2 V in Figure 4.10 f) shows a delocalized edge state along the T30 edge, as well as states localized at the pores of the GNR, while the edge along the C30 part is dark indicating a minimum in the differential conductance. The scan direction was chosen perpendicular to the length of the GNR to rule out an effect by the latency of the feed-back loop. A state localized at the pores is not expected [33] and conductance at these locations might arise from probing the substrate. However, the T30 edge state and the minimum in differential conductance along the edge of C30 can clearly be differentiated from the substrate. A small differential conductance at 0.2 V could arise from the tails of the state at -0.22 V and -0.27 V reported for C30- and T30-GNRs, respectively [33].

Fig. 4.10 g) provides a close-up view of T30-C30-heterostructures. The individual shapes of the molecules are clearly distinguishable which allows to estimate their intactness. 65% of the investigated molecules show defects. This high amount makes growing long defect free GNRs unlikely. Within the scope of this thesis only the small area shown in Fig. 4.10 g) was used for determining the ratio of intact to not intact GNRs, so the high amount of defects could be a result of the small sample size. However, this finding seems to be in agreement with previous results conducted on samples that were manufactured from the same molecular material [33]. A more thorough study on this topic would need to be conducted to draw conclusions on the origin of the defects. So called bite-defects which are missing phenyl moieties in GNRs were reported to originate from phenyl cleaving during the cyclodehydrogentation step in the on surface synthesis route [181]. However, a large amount of defects might rather indicate deterioration of the precursor material which is more likely due to its age of several years.

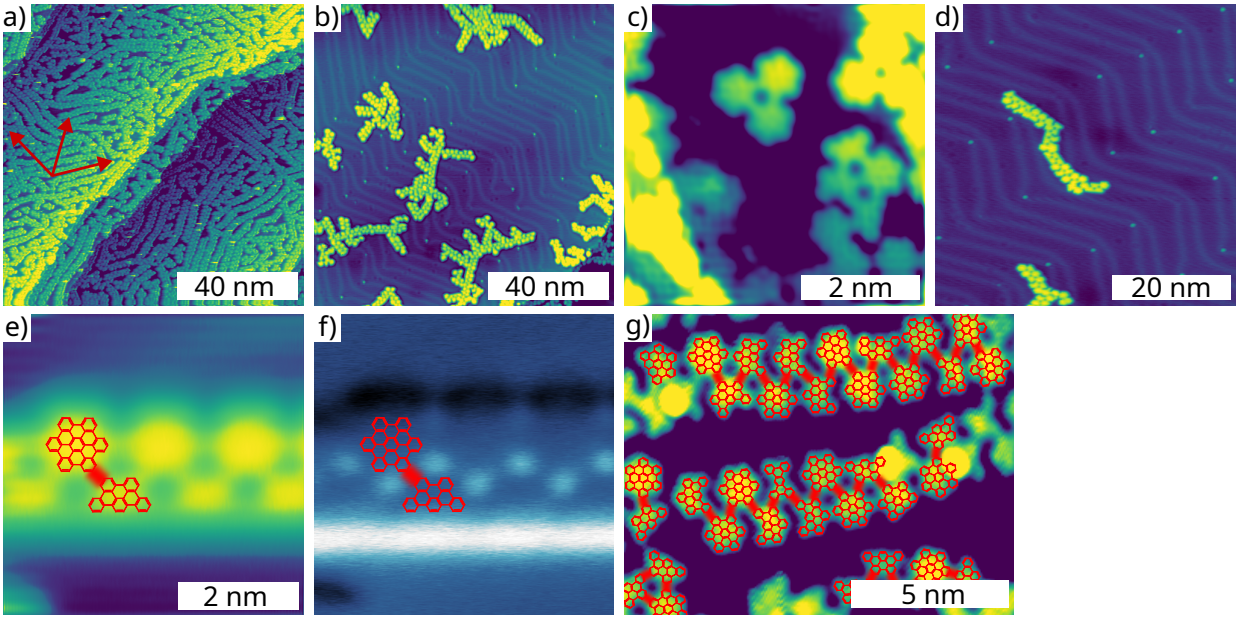

Figure 4.10: STM topography of a) T30-C30-GNR-heterostructures on Au(111) at high coverage (0.9 V, 300 pA) and b) low coverage (0.9 V, 300 pA). c) Isolated closed GNR triangle. (0.9 V, 300 pA). d) A single GNR aligned with the herringbone reconstruction. (0.9 V, 300 pA). e) GNR heterostructure of C30 on the upper side and T30 on the lower side (0.9 V, 300 pA) with d) corresponding dI/dV map and structure exemplary overlaid (0.2 V, 1 nA). g) C30-T30 heterostructure GNRs with structure overlaid highlighting defects. (0.9 V, 300 pA).

4.4.4 C30-4Br-GNRs

Since the electronic properties of porous T30-GNRs seemed promising, precursors with 4 halogen bonds were investigated. These precursors called C30-4Br are a variation to the C30-molecules featuring two additional Br atoms (Fig. 4.11 a)). Similar molecules were proposed by M. Gille et al. [182] for the fabrication of porous GNR sheets but their on-surface synthesis has not yet been investigated.

A sample was prepared by stamping C30-4Br-precursors on Au(111) via DCT followed by annealing at 100 °C for 60 min to promote diffusion. Annealing at this moderate temperature leads to molecules assembling into chains with short range order. At high coverage (Fig. 4.11 b)), domains of such chains aligning next to each other are present. One of these domains is highlighted by parallel red lines. These domains have a 60° orientation to one another induced by the threefold symmetry of the herringbone reconstruction that is depicted by the three red arrows. At low coverage, the molecules assemble into dendritic islands, again consisting of molecular chains with short range order (Fig. 4.11 c)) following the herringbone template to some extent. While there are reports on the on-surface polymerization at temperatures below 100 °C [183–185] sufficient debromination for larger molecules such as C30-4Br is expected at higher temperatures close to 200 °C [18, 33]. Fig 4.11 b) and c) are therefore not depicting the polymeric phase but the self-assembly of individual pre-

cursors. The self-assembly is driven by the interaction between the molecules and between the molecules and the surface. The non-covalent halogen-halogen and halogen-hydrogen interactions across molecules is a known driving mechanism for the self-assembly of organic molecules on metallic surfaces [186–188].

Annealing the sample at 350 °C for about 1 min leads to cyclodehydrogenation (Fig 4.11 d)). The phenyl moieties are now planarized on the surface and the island appears flat with no inter-molecular contrast indicating a delocalized π-electron system. The islands at areas with coverage below 1 ML consist of unordered molecules similar to the islands of precursors. As expected, annealing at high temperatures for a short period of time induces cyclodehydrogenation without changing the self-assembly or long range order. Fig. 4.11 e)-g) show samples prepared by ESD. C30-4Br-precursors in acetone solution with a concentration of 1 mg/10 ml were sprayed on clean Au(111) at a rate of 3 µl/min for 10 min in inert gas atmosphere with a voltage of 3.29 kV. The sample was then transferred in the UHV system in a vacuum suitcase to avoid contamination with atmosphere and annealed by ramping the temperature up to 103 °C over a time span of 40 min. The sample was annealed in three more steps, at 120 °C for 10 min, 140 °C for 20 min and 180 °C, checking the adsorption and stability of the molecules each time with STM. The STM topography shows multilayers of unordered molecules. (Fig. 4.11 e)). Choosing different parameters for ESD, a cleaner sample more suitable for STM was obtained. A solution with the same concentration of 1 mg/10 ml was sprayed at a rate of 4 µl/min onto clean Au(111) at 3.34 kV. The sample was then annealed by ramping the temperature up to 108 °C over 17 min, and to 211 °C over 20 min. This resulted in a sample with coverage close to 1 ML with some multilayer formation (Fig. 4.11 f)). The stacking characteristic becomes more apparent in Fig 4.11 g). The star-shape of the molecules is apparent in the bottom layer and the upper layer. The interaction between the layers is assumed to be due to $\pi - \pi$ overlap.

Figure 4.12 a) shows an island of C30-precursors. The backbone of the chain can be distinguished as a longitudinal darker flat area on the Au(111) surface surrounded by butterfly shapes that consist of 4 phenyl rings. It can be rationalized that the backbone is formed by the more ridged part of the precursors that lies flat on the surface. The rest of the phenyl rings are free to rotate along their bond which allows them to increase the overlap of the π-orbitals. Similar behavior was observed for T30-polymers [33]. The combination of π-π-interaction and halogen-halogen bond formation is assumed to be the main driving mechanism for the island formation. The assumed molecular structure of the chains aligned next to each other is displayed in Fig. 4.12 b). Higher contrast areas indicate a stacking in z-direction due to close packing. The data of the cross-sections as indicated in Fig. 4.12 a) are shown in Fig. 4.12 c) and d). The rotated phenyl rings have an apparent height variation of approximately 40 pm as shown in Fig. 4.12 c), cross-section 1). Cross-section 2 shows the apparent height variation of roughly 10 pm along the backbone. When the brominated phenyl moieties stack on top of each other, the apparent height variation is increased to about 50 pm (Fig. 4.12 c), cross-section 3). Cross-section 4) and 5) in figure 4.12 d) show the height difference between the substrate and the backbone, and the height difference

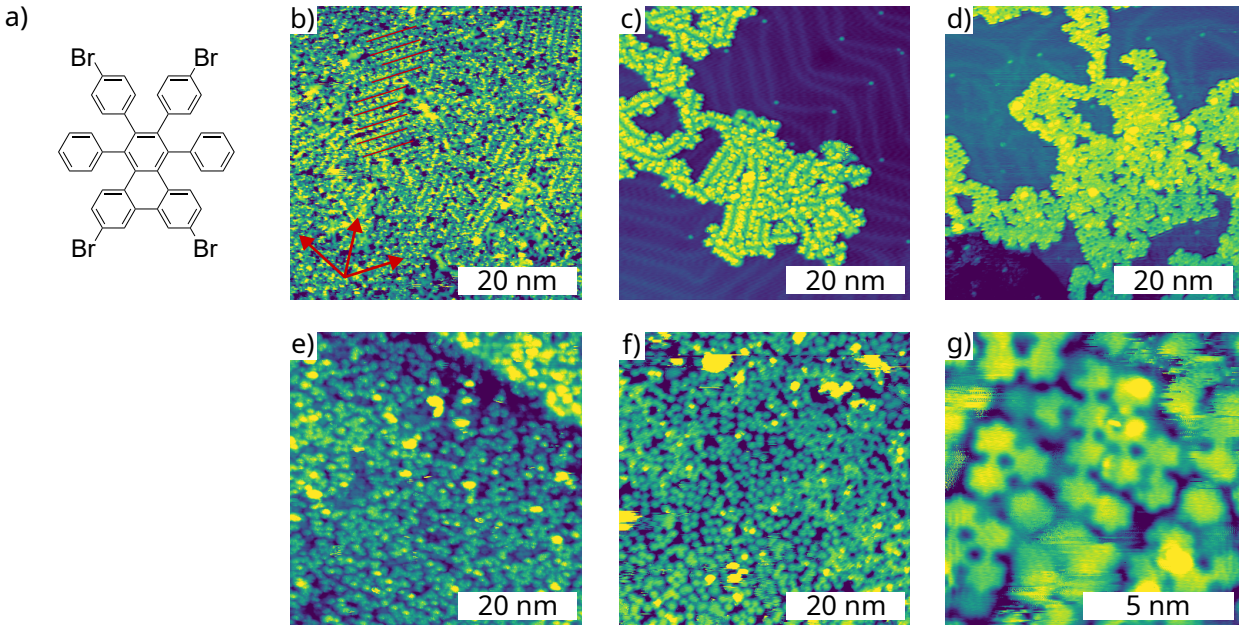

Figure 4.11: STM topography overview of C30-4Br-precursors and GNRs on Au(111) prepared by DCT (b-d) and ESD (e-g). a) Structure drawing of C30-4Br-precursors. b) Chains of precursors forming ordered domains at a coverage close to 1 ML. One domain is highlighted by the parallel red lines. The domains follow the threefold symmetry of the herringbone reconstruction indicated by the red arrows. (0.9 V, 300 pA) c) Precursors assembling into islands consisting of molecular chains. (2.0 V, 300 pA). d) Islands of molecules after cyclodehydrogenation at coverage below 1 ML. (1.5 V, 300 pA). e) Planarized molecules at coverage close to 1 ML. (1.2 V, 300 pA). f) Planarized molecules at coverage above 1 ML. (1.0 V, 300 pA). g) Close-up view of the multi-layer stacking. (1.0 V, 300 pA).

between the substrate and the adjacent chains, respectively.

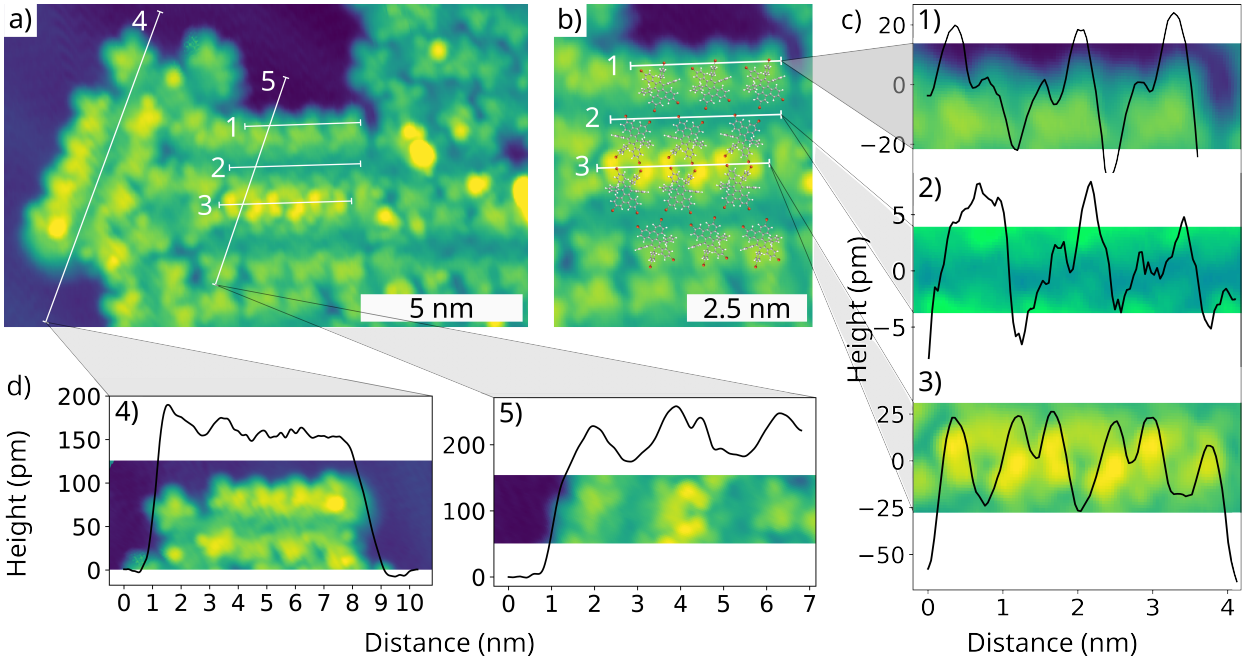

Figure 4.12: a) STM topography of C30-4Br precursor chains on Au(111) with positions of cross-sections. b) Molecular models superimposed to scale showing the arrangement of molecules. c) Cross-sections of 1)-3). d) Cross-sections 4) and 5). (2.0 V, 300 pA).

4.4.5 Summary and discussion

The most relevant findings of my studies of self-assembled GNR structures on surfaces were presented in this section. As a starting point, the polymeric phase of T90 was imaged with STM to familiarize myself with the experimental procedures and verify working principles in preparation for my studies of GNR heterostructures and two dimensional sheets. Building on my predecessor's work [33], samples of T30-GNRs were then prepared, showing the growth characteristic and their potential for manufacturing porous GNRs with unique electronic properties. These properties were investigated with dI/dV maps. The potential of these GNRs for forming two dimensional carbon sheets with a band-gap is substantiated by other work focusing on electronic states localized at the pores that has been published after I switched my topic of research [18–20]. The adsorption behavior and self-assembly of samples prepared by depositing a mixture of T30-C30-precursors were investigated as a potential way to fabricate porous nanostructures, giving a first indication on the electronic properties of such a heterostructure and outlining difficulties to overcome. Finally, STM topography of C30-4Br-GNRs is presented, demonstrating the growth characteristics of samples prepared by DCT and ESD. To my knowledge, no reports exist on the C30-4Br-precursors used for the on-surface synthesis, yet.

5 Outlook and Conclusion

The aim of this thesis was on the one hand to study GNR nanostructures in the group of Prof. Axel Enders at the University of Bayreuth and on the other hand to investigate the photophysical properties of Eu^{3+} complexes with the γ-STM in the group of Prof. Wulf Wulfhekel at the KIT.

Investigating GNRs was a great starting point to familiarize myself with UHV systems and the working principle of an STM. Combining the bottom-up-approach for on surface synthesis with the DCT deposition technique is a powerful method for obtaining a gradient in the coverage on the sample. This allows to investigate the self-assembly of nanostructures at different coverage on the same sample. T90-polymers were used as a starting point since they grow in nicely ordered chains which makes them comparably easy to scan in STM topography. Building on previous work done by my colleague, I moved on from well established molecules to the T30-precursors first reported by the group of Prof. Enders. Their 30° bonding angle allows manufacturing porous GNRs which leads to unique electronic properties. For this reason, porous GNRs synthesized from T30-precursors have since been subject of three publications, one of which from the Enders group [18] and one from its collaborators [20]. Heterostructures were manufactured by depositing a mix of C30- and T30-precursors via DCT. Measuring the differential conductance allowed to verify the principle of obtaining heterostructures with unique electronic properties. This is a promising starting point for future experiments. Heterostructures could potentially be manufactured in a more controlled manner when exploiting the different diffusivities of precursors. Similar experiments were published by the group in the past [29]. Furthermore, precursors and GNRs of C30-4Br-molecules were shown in STM topography. The precursors were found to form ordered domains at areas with high coverage. This could potentially be exploited for obtaining porous nanostructures with long range order. To my knowledge, no reports exist on these molecules, yet.

My research at the group of Prof. Wulfhekel focused on the photophysical properties of Eu^{3+} complexes. The unique electronic structure of these complexes leads to sharp emission lines from long lived states. This makes them interesting to investigate with the γ-STM that allows to combine STM topography with luminescence experiments. A major focus of my work was understanding and optimizing the sublimation process for preparing samples. This required modifying the UHV system by adding a pumping line to the evaporator and later moving the evaporator from the preparation chamber to the load-lock. This increased the flexibility and ease of use when working with the evaporator which was required for the extensive sublimation tests. The sample preparation was constantly checked with STM topography. Starting with the betadiketonate complexes $[Eu(btfa)_3(bpy)]$ and $[Eu(tta)_3(bpy)]$,

it soon became obvious that thorough experiments on the sublimation parameters are necessary. Implementing the quartz crystal microbalance to callibrate the deposition rate was an important improvement and a key factor for depositing the desired molecules on the substrate. Identifying the intactness and orientation of the complexes on the surface is still challenging, but the insights provided in this thesis regarding purifying the molecular material by degassing pave the way for future experiments, especially when approaching luminescence from single molecules. Next to STM topography of the betadiketonate complexes [Eu(btfa)$_3$(bpy)], [Eu(tta)$_3$(bpy)] and [Eu(tta)$_3$(H_2O)$_2$], images of the platform complexes [Eu(trensal)], [Eu(trensal-O-Bn)], [Eu(trensal)Ph-SMe] and [Tb(Tacn)] were provided in this work. To my knowledge, no reports on [Eu(trensal-Ph-SMe)], [Eu(trensal-O-Bn)] and [Tb(TACN)] exist, yet.

Electro-luminescence of Eu^{3+} complexes which was considered straight-forward to achieve at first was not observed. The idea was to excite luminescence with tunneling electrons, which was successfully done in the past by the Wulfhekel group [60–62]. Complexes were at first deposited on an insulating layer of NaCl on Au(111), a technique also previously used to reduce quenching by electron transport to the substrate. Later complexes expected to self-decouple from the substrate were deposited on Ag(111) due to its low absorbance across a wide wavelength range. Different tunneling parameters were tested based on the expertise gained from previous experiments. However, there was no clear indication on light emission due to electro-luminescence.

Experiments on bulk samples prepared by subliming complexes on glass substrates proofed the feasibility of performing PL experiments on sublimed samples. Comparing the PL spectra of sublimed samples and samples drop-casted from solution furthermore demonstrated how different sample preparation methods and the resulting film growths are reflected in the PL spectra. The PL decay dynamics of these samples where supplemented by TCSPC measurements of powder samples and complexes in solution. A comparison between [Eu(btfa)$_3$(bpy)] and [Eu(tta)$_3$(bpy)] that are similar in structure and [Eu(tta)$_3$(H_2O)$_2$] which features water ligands further proofed the principle of determining quenching mechanisms inherent to inter-molecular vibrations, as well as quenching due to interaction with the surrounding medium.

The implementation of the quartz crystal microbalance to callibrate the deposition rate was an important improvement and a key factor for growing molecular films with precise thicknesses. These films played a fundamental part in understanding the excitation, relaxation and charge transfer dynamics within Eu^{3+} complexes. Thin film samples with controlled thicknesses could thus be prepared. This allowed me to compare nominally identical samples of films sublimed on dielectric and metallic substrates. This improved the understanding of luminescence from molecules adsorbed on metal surfaces which is also highly interesting for EL experiments. Furthermore, the PL and TCSPC data from the betadiketonate complexes [Eu(btfa)$_3$(bpy)] and [Eu(tta)$_3$(bpy)] was compared to [Eu(trensal)]. The difficulties in the sample preparation of betadiketonate complexes and their fragility shifted me towards more rigid platform complexes. Comparing the experimental results, [Eu(trensal)] indeed seems

to be more stable with regard to intactness upon sublimation, however, the luminescence is overall weaker.

The future aim could now be to focus on manufacturing Eu^{3+} ions incorporated in a self-decoupling platform scaffold. In the best case, a tripodal platform structure would lead to most molecules standing on the substrate in the same manner. They would therefore have the same orientation on the substrate which facilitates the identification with STM. Furthermore, molecules with the same orientation would also have dipole moments aligned in the same direction. Having a defined dipole moment and self-decoupling molecules eliminates the element of randomness in luminescence experiments. Thanks to the fruitful collaboration with the group of Prof. Michael Seitz at the University of Tuebingen, the charge transfer dynamics of several platform complexes could be investigated. Performing TCSPC measurements on simple powder samples at different wavelengths already reveals the excitation and relaxation mechanisms within the complexes and their timescales. This method is a powerful tool for determining the suitability of complexes for luminescence experiments. It immediately provides information on the overall luminescence intensity from the first and second excited states of Eu^{3+} and on the charge transfer between them.

The modification of luminescence from molecules adsorbed on metal surfaces is a well known effect. Initially, we expected electron transport from the complex to the substrate to be responsible for the failing EL experiments. This assumption was based on previous findings from the group on chromophores that require decoupling from the substrate by an insulating layer for sufficient EL. However, growing molecular thin films on a metal substrate, which was only possible after establishing a finely controllable sublimation process, allowed to investigate the energy transfer mechanism more thoroughly. The modification of the dipole emission due to the presence of a metal surface was determined to be mainly responsible for the reduction in luminescence into the far field. This fundamentally changed our understanding of the experimental properties. A comparison with the theoretical model for dipole emission in proximity to metal surfaces suggests that luminescence may be reduced due to the excitation of SPPs and gap plasmons that decay without radiating into the far field. This assumption can be tested by using a structured substrate which then allows SPPs to also radiate into the far field. Experiments on this matter are already in preparation.

List of Figures

List of Tables

Bibliography

[1] B. Lounis and W. E. Moerner. “Single photons on demand from a single molecule at room temperature”. In: *Nature* 407.6803 (2000), pp. 491–493.

[2] X. Li, X. Wang, L. Zhang, S. Lee, and H. Dai. “Chemically Derived, Ultrasmooth Graphene Nanoribbon Semiconductors”. In: *Science* 319.5867 (2008), pp. 1229–1232.

[3] Z. Geng, B. Hähnlein, R. Granzner, M. Auge, A. A. Lebedev, V. Y. Davydov, M. Kittler, J. Pezoldt, and F. Schwierz. “Graphene Nanoribbons for Electronic Devices”. In: *Annalen der Physik* 529.11 (2017), p. 1700033.

[4] K. S. Novoselov, A. K. Geim, S. V. Morozov, D. Jiang, Y. Zhang, S. V. Dubonos, I. V. Grigorieva, and A. A. Firsov. “Electric Field Effect in Atomically Thin Carbon Films”. In: *Science* 306.5696 (2004), pp. 666–669.

[5] L. Jiao, L. Zhang, X. Wang, G. Diankov, and H. Dai. “Narrow graphene nanoribbons from carbon nanotubes”. In: *Nature* 458.7240 (2009), pp. 877–880.

[6] A. Fasoli, A. Colli, A. Lombardo, and A. C. Ferrari. “Fabrication of graphene nanoribbons via nanowire lithography”. In: *physica status solidi (b)* 246.11-12 (2009), pp. 2514–2517.

[7] J. Cai, P. Ruffieux, R. Jaafar, M. Bieri, T. Braun, S. Blankenburg, M. Muoth, A. P. Seitsonen, M. Saleh, X. Feng, K. Müllen, and R. Fasel. “Atomically precise bottom-up fabrication of graphene nanoribbons”. In: *Nature* 466.7305 (2010), pp. 470–473.

[8] L. Yang, C.-H. Park, Y.-W. Son, M. L. Cohen, and S. G. Louie. “Quasiparticle Energies and Band Gaps in Graphene Nanoribbons”. In: *Physical Review Letters* 99.18 (2007), p. 186801.

[9] V. Barone, O. Hod, and G. E. Scuseria. “Electronic Structure and Stability of Semiconducting Graphene Nanoribbons”. In: *Nano Letters* 6.12 (2006), pp. 2748–2754.

[10] N. Merino-Díez, A. Garcia-Lekue, E. Carbonell-Sanromà, J. Li, M. Corso, L. Colazzo, F. Sedona, D. Sánchez-Portal, J. I. Pascual, and D. G. de Oteyza. “Width-Dependent Band Gap in Armchair Graphene Nanoribbons Reveals Fermi Level Pinning on Au(111)”. In: *ACS Nano* 11.11 (2017), pp. 11661–11668.

[11] Y.-W. Son, M. L. Cohen, and S. G. Louie. “Energy Gaps in Graphene Nanoribbons”. In: *Physical Review Letters* 97 (21 2006), p. 216803.

[12] C. Tao, L. Jiao, O. V. Yazyev, Y.-C. Chen, J. Feng, X. Zhang, R. B. Capaz, J. M. Tour, A. Zettl, S. G. Louie, H. Dai, and M. F. Crommie. “Spatially resolving edge states of chiral graphene nanoribbons”. In: *Nature Physics* 7.8 (2011), pp. 616–620.

[13] K. A. Ritter and J. W. Lyding. "The influence of edge structure on the electronic properties of graphene quantum dots and nanoribbons". In: *Nature Materials* 8.3 (2009), pp. 235–242.

[14] J. D. Teeter, P. Zahl, M. Mehdi Pour, P. S. Costa, A. Enders, and A. Sinitskii. "On-Surface Synthesis and Spectroscopic Characterization of Laterally Extended Chevron Graphene Nanoribbons". In: *ChemPhysChem* 20.18 (2019), pp. 2281–2285.

[15] J. Cai, C. A. Pignedoli, L. Talirz, P. Ruffieux, H. Söde, L. Liang, V. Meunier, R. Berger, R. Li, X. Feng, K. Müllen, and R. Fasel. "Graphene nanoribbon heterojunctions". In: *Nature Nanotechnology* 9.11 (2014), pp. 896–900.

[16] C. Bronner, S. Stremlau, M. Gille, F. Brauße, A. Haase, S. Hecht, and P. Tegeder. "Aligning the Band Gap of Graphene Nanoribbons by Monomer Doping". In: *Angewandte Chemie International Edition* 52.16 (2013), pp. 4422–4425.

[17] A. Baskin and P. Král. "Electronic structures of porous nanocarbons". In: *Scientific Reports* 1.36 (2011).

[18] M. Sarker, C. Dobner, P. Zahl, C. Fiankor, J. Zhang, A. Saxena, N. Aluru, A. Enders, and A. Sinitskii. "Porous Nanographenes, Graphene Nanoribbons, and Nanoporous Graphene Selectively Synthesized from the Same Molecular Precursor". In: *Journal of the American Chemical Society* 146.21 (2024), pp. 14453–14467.

[19] Q. Fan, Z. Ruan, S. Werner, T. Naumann, R. Bolat, J. Martinez-Castro, T. Koehler, T. Vollgraff, W. Hieringer, R. Mandalia, C. Neiß, A. Görling, F. S. Tautz, J. Sundermeyer, and J. M. Gottfried. "Bottom-up Synthesis and Characterization of Porous 12-Atom-Wide Armchair Graphene Nanoribbons". In: *Nano Letters* 24.35 (2024), pp. 10718–10723.

[20] P. Angulo-Portugal, M. Irizar, L. Huang, M. Sarker, M. A. Ashoush, Z. M. A. El-Fattah, J. Barth, F. Schiller, A. El-Sayed, F. Gao, D. G. de Oteyza, A. Sinitskii, A. Garcia-Lekue, M. Corso, and I. Piquero-Zulaica. "A Functional 2D Carbon Allotrope Combining Nanoporous Graphene and Biphenylene Segments". In: *Advanced Materials* (2025), e11706.

[21] A. Ghadiyani and H. Karimiyan Alidash. "Optimization of quantum capacitance and improvement of RF performance in dual-ribbon GNRFET by tuning the GNR-to-GNR distance". In: *Journal of Computational Electronics* 24.102 (2025).

[22] O. Gröning, S. Wang, X. Yao, C. A. Pignedoli, G. Borin Barin, C. Daniels, A. Cupo, V. Meunier, X. Feng, A. Narita, K. Müllen, P. Ruffieux, and R. Fasel. "Engineering of robust topological quantum phases in graphene nanoribbons". In: *Nature* 560.7717 (2018), pp. 209–213.

[23] S. Wang, N. Kharche, E. Costa Girão, X. Feng, K. Müllen, V. Meunier, R. Fasel, and P. Ruffieux. "Quantum Dots in Graphene Nanoribbons". In: *Nano Letters* 17.7 (2017), pp. 4277–4283.

[24] Y.-W. Son, M. L. Cohen, and S. G. Louie. "Half-metallic graphene nanoribbons". In: *Nature* 444.7117 (2006), pp. 347–349.

[25] R. E. Blackwell, F. Zhao, E. Brooks, J. Zhu, I. Piskun, S. Wang, A. Delgado, Y.-L. Lee, S. G. Louie, and F. R. Fischer. "Spin splitting of dopant edge state in magnetic zigzag graphene nanoribbons". In: *Nature* 600.7890 (2021), pp. 647–652.

[26] S. Darbari, V. Ahmadi, P. Afzali, and Y. Abdi. "Photocatalytic reduction of GO/ZnO to achieve GNRs for optoelectronic applications". In: *Journal of Physics D: Applied Physics* 46.38 (2013), p. 385101.

[27] A. Tavousi, M. A. Mansouri-Birjandi, and M. Janfaza. "Optoelectronic application of graphene nanoribbon for mid-infrared bandpass filtering". In: *Applied Optics* 57.20 (2018), pp. 5800–5805.

[28] P. Xin-Xiang, L. Wen-Ru, and Z. Guang-Hui. "Optoelectronic Properties for Armchair-Edge Graphene Nanoribbons". In: *Chinese Physics Letters* 25.9 (2008), p. 3436.

[29] C. Dobner, G. Li, M. Sarker, A. Sinitskii, and A. Enders. "Diffusion-controlled on-surface synthesis of graphene nanoribbon heterojunctions". In: *RSC Advances* 12 (11 2022), pp. 6615–6618.

[30] F. Baier. "Elektrospray-Deposition und rastertunnelmikroskopische Untersuchung unter Ultrahochvakuum von in Lösung synthetisierten Molekülen". Ph.D. Dissertation. Bayreuth, Germany: University of Bayreuth, 2024.

[31] Y. S. Kim, S. J. Jeong, H. W. Lee, J. Kim, S. E. Lee, Y. K. Kim, and S. S. Yoon. "Efficient blue organic light-emitting diodes using N^2,N^2,N^{11},N^{11},5,6,7,8-octaphenyltriphenylene-2,11-diamine derivatives". In: *Luminescence* 31.4 (2016), pp. 1031–1036.

[32] A. Thiessen, H. Wettach, K. Meerholz, F. Neese, S. Höger, and D. Hertel. "Control of electronic properties of triphenylene by substitution". In: *Organic Electronics* 13.1 (2012), pp. 71–83.

[33] C. Dobner. "Synthesis and electronic characterization of bottom-up synthesized graphene nanoribbons and porous nanographenes." Ph.D. Dissertation. Bayreuth, Germany: University of Bayreuth, 2022.

[34] K. Binnemans. "Interpretation of europium(III) spectra". In: *Coordination Chemistry Reviews* 295 (2015), pp. 1–45.

[35] P. Porcher and P. Caro. "Influence of J-mixing on the phenomenological interpretation of the Eu^{3+} ion spectroscopic properties". In: *Journal of Luminescence* 21.2 (1980), pp. 207–216.

[36] M. Tanaka, G. Nishimura, and T. Kushida. "Contribution of J mixing to the $^5D_0$-$^7F_0$ transition of Eu^{3+} ions in several host matrices". In: *Physical Review B* 49.24 (1994), pp. 16917–16925.

[37] M. Tanaka and T. Kushida. "Effects of static crystal field on the homogeneous width of the $^5D_0 - ^7F_0$ line of Eu^{3+} and Sm^{2+} in solids". In: *Physical Review B* 52.6 (1995), pp. 4171–4178.

[38] O. L. Malta. "Lanthanide f↔f transitions hypersensitive to the environment". In: *Molecular Physics* 42.1 (1981), pp. 65–72.

[39] X. Y. Chen and G. K. Liu. "The standard and anomalous crystal-field spectra of Eu^{3+}". In: *Journal of Solid State Chemistry* 178.2 (2005), pp. 419–428.

[40] B. Doppagne, M. C. Chong, H. Bulou, A. Boeglin, F. Scheurer, and G. Schull. "Electrofluorochromism at the single-molecule level". In: *Science* 361.6399 (2018), pp. 251–255.

[41] E. Kreidt, C. Kruck, and M. Seitz. "Chapter 300 - Nonradiative Deactivation of Lanthanoid Luminescence by Multiphonon Relaxation in Molecular Complexes". In: *Including Actinides*. Ed. by J.-C. G. Bünzli and V. K. Pecharsky. Vol. 53. Handbook on the Physics and Chemistry of Rare Earths. Elsevier, 2018, pp. 35–79.

[42] O. L. Malta, H. F. Brito, J. F. S. Menezes, F. R. Gonçalves e Silva, S. Alves, F. S. Farias, and A. V. M. de Andrade. "Spectroscopic properties of a new light-converting device Eu(thenoyltrifluoroacetonate)$_3$ 2(dibenzyl sulfoxide). A theoretical analysis based on structural data obtained from a sparkle model". In: *Journal of Luminescence* 75.3 (1997), pp. 255–268.

[43] J. Guan, B. Chen, Y. Sun, H. Liang, and Q. Zhang. "Effects of synergetic ligands on the thermal and radiative properties of Eu(TTA)$_3n$L-doped poly(methyl methacrylate)". In: *Journal of Non-Crystalline Solids* 351.10-11 (2005), pp. 849–855.

[44] S. V. Eliseeva, D. N. Pleshkov, K. A. Lyssenko, L. S. Lepnev, J.-C. G. Bünzli, and N. P. Kuzmina. "Highly Luminescent and Triboluminescent Coordination Polymers Assembled from Lanthanide β-Diketonates and Aromatic Bidentate *O*-Donor Ligands". In: *Inorganic Chemistry* 49.20 (2010), pp. 9300–9311.

[45] B. N. J. Persson. "Theory of the damping of excited molecules located above a metal surface". In: *Journal of Physics C: Solid State Physics* 11.20 (1978), p. 4251.

[46] A. Campion, A. R. Gallo, C. B. Harris, H. J. Robota, and P. M. Whitmore. "Electronic energy transfer to metal surfaces: a test of classical image dipole theory at short distances". In: *Chemical Physics Letters* 73.3 (1980), pp. 447–450.

[47] S. C. Kitson, W. L. Barnes, and J. R. Sambles. "Surface-plasmon energy gaps and photoluminescence". In: *Physical Review B* 52 (15 1995), pp. 11441–11445.

[48] I. Pockrand, A. Brillante, and D. Möbius. "Nonradiative decay of excited molecules near a metal surface". In: *Chemical Physics Letters* 69.3 (1980), pp. 499–504.

[49] R. Faggiani, J. Yang, and P. Lalanne. "Quenching, Plasmonic, and Radiative Decays in Nanogap Emitting Devices". In: *ACS Photonics* 2.12 (2015), pp. 1739–1744.

[50] D. Toptygin. "Effects of the Solvent Refractive Index and Its Dispersion on the Radiative Decay Rate and Extinction Coefficient of a Fluorescent Solute". In: *Journal of Fluorescence* 13.3 (2003), pp. 201–219.

[51] C. L. Tregidgo, J. A. Levitt, and K. Suhling. "Effect of refractive index on the fluorescence lifetime of green fluorescent protein". In: *Journal of Biomedical Optics* 13.3 (2008), p. 031218.

[52] A. Ebert, L. Gerhard, J. Feye, S. K. Kuppusamy, B. Brachnakova, M. Ruben, P. W. Roesky, and W. Wulfhekel. "Photoluminescence and self-assembly of three different Eu complexes. Licensed under CC BY 4.0 (`https://creativecommons.org/licenses/by/4.0/`). Changes made." In: *Physical Chemistry Chemical Physics* 27 (26 2025), pp. 13984–13990.

[53] R. S. Knox and H. van Amerongen. "Refractive Index Dependence of the Förster Resonance Excitation Transfer Rate". In: *The Journal of Physical Chemistry B* 106.20 (2002), pp. 5289–5293.

[54] J. Fischer, J. B. Mueller, J. Kaschke, T. J. A. Wolf, A.-N. Unterreiner, and M. Wegener. "Three-dimensional multi-photon direct laser writing with variable repetition rate". In: *Optics Express* 21.22 (2013), pp. 26244–26260.

[55] J. Fischer and M. Wegener. "Three-dimensional direct laser writing inspired by stimulated-emission-depletion microscopy [Invited]". In: *Optical Materials Express* 1.4 (2011), pp. 614–624.

[56] M. Thiel, J. Fischer, G. von Freymann, and M. Wegener. "Direct laser writing of three-dimensional submicron structures using a continuous-wave laser at 532 nm". In: *Applied Physics Letters* 97.22 (2010), p. 221102.

[57] M. Deubel, G. von Freymann, M. Wegener, S. Pereira, K. Busch, and C. M. Soukoulis. "Direct laser writing of three-dimensional photonic-crystal templates for telecommunications". In: *Nature Materials* 3.7 (2004), pp. 444–447.

[58] K. Edelmann, L. Gerhard, M. Winkler, L. Wilmes, V. Rai, M. Schumann, C. Kern, M. Meyer, M. Wegener, and W. Wulfhekel. "Light collection from a low-temperature scanning tunneling microscope using integrated mirror tips fabricated by direct laser writing". In: *Review of Scientific Instruments* 89.12 (2018), p. 123107.

[59] K. Edelmann. "Electroluminescence from Plasmonic Excitations in a Scanning Tunnelling Microscope". PhD thesis. Karlsruher Institut für Technologie (KIT), 2019. 136 pp.

[60] V. Rai, N. Balzer, G. Derenbach, C. Holzer, M. Mayor, W. Wulfhekel, L. Gerhard, and M. Valášek. "Hot luminescence from single-molecule chromophores electrically and mechanically self-decoupled by tripodal scaffolds". In: *Nature Communications* 14.8253 (2023).

[61] V. Rai, L. Gerhard, Q. Sun, C. Holzer, T. Repän, M. Krstić, L. Yang, M. Wegener, C. Rockstuhl, and W. Wulfhekel. "Boosting Light Emission from Single Hydrogen Phthalocyanine Molecules by Charging". In: *Nano Letters* 20.10 (2020), pp. 7600–7605.

[62] V. N. Rai. "Light Emission from Single Self-decoupled Molecules in a Scanning Tunnelling Microscope". Ph.D. Dissertation. Karlsruhe, Germany: Karlsruhe Institute of Technology, 2021.

[63] D. Meschede. *Gerthsen Physik*. 25th ed. Springer-Lehrbuch. Springer Spektrum, Berlin, Heidelberg, 2015, pp. XVI, 1052.

[64] G. Binnig, H. Rohrer, C. Gerber, and E. Weibel. “Surface Studies by Scanning Tunneling Microscopy”. In: *Physical Review Letters* 49.1 (1982), pp. 57–61.

[65] C. J. Chen. *Introduction to Scanning Tunneling Microscopy*. Oxford University Press, 2021.

[66] K. Kaiser, L.-A. Lieske, J. Repp, and L. Gross. “Charge-state lifetimes of single molecules on few monolayers of NaCl”. In: *Nature Communications* 14.4988 (2023).

[67] Y. Zhang, Y. Luo, Y. Zhang, Y.-J. Yu, Y.-M. Kuang, L. Zhang, Q.-S. Meng, Y. Luo, J.-L. Yang, Z.-C. Dong, and J. G. Hou. “Visualizing coherent intermolecular dipole-dipole coupling in real space”. In: *Nature* 531.7596 (2016), pp. 623–627.

[68] X. H. Qiu, G. V. Nazin, and W. Ho. “Vibrationally Resolved Fluorescence Excited with Submolecular Precision”. In: *Science* 299.5606 (2003), pp. 542–546.

[69] E. Ćavar, M.-C. Blüm, M. Pivetta, F. Patthey, M. Chergui, and W.-D. Schneider. “Fluorescence and Phosphorescence from Individual C_{60} Molecules Excited by Local Electron Tunneling”. In: *Physical Review Letters* 95 (19 2005), p. 196102.

[70] A. Köhler and H. Bässler. *Electronic Processes in Organic Semiconductors*. Weinheim: Wiley-VCH, 2015.

[71] E. M. Purcell, H. C. Torrey, and R. V. Pound. “Resonance Absorption by Nuclear Magnetic Moments in a Solid”. In: *Physical Review* 69 (1-2 1946), pp. 37–38.

[72] L. Douillard and F. Charra. “High-resolution microscopy of plasmon field distributions by scanning tunneling luminescence and photoemission electron microscopies”. In: *Comptes Rendus Physique* 13.8 (2012), pp. 815–829.

[73] L. Novotny and B. Hecht. *Principles of Nano-Optics*. 2nd ed. Cambridge University Press, 2012.

[74] H. Morawitz and M. R. Philpott. “Coupling of an excited molecule to surface plasmons”. In: *Physical Review B* 10 (12 1974), pp. 4863–4868.

[75] A. V. Zayats, I. I. Smolyaninov, and A. A. Maradudin. “Nano-optics of surface plasmon polaritons”. In: *Physics Reports* 408 (3-4 2005), pp. 131–314.

[76] J. Lambe and S. L. McCarthy. “Light Emission from Inelastic Electron Tunneling”. In: *Physical Review Letters* 37 (14 1976), pp. 923–925.

[77] K. H. Drexhage. “Influence of a dielectric interface on fluorescence decay time”. In: *Journal of Luminescence* 1-2 (1970), pp. 693–701.

[78] H. Kuhn. “Classical Aspects of Energy Transfer in Molecular Systems”. In: *The Journal of Chemical Physics* 53.1 (1970), pp. 101–108.

[79] H. Morawitz. “Self-Coupling of a Two-Level System by a Mirror”. In: *Physical Review* 187 (5 1969), pp. 1792–1796.

[80] R. R. Chance, A. Prock, and R. Silbey. “Molecular Fluorescence and Energy Transfer Near Interfaces”. In: *Advances in Chemical Physics*. Vol. 37. John Wiley & Sons, Ltd, 1978, pp. 1–65.

[81] A. Sommerfeld. *Partial differential equations in physics*. Vol. 1. Academic press, 1949.

[82] G. W. Ford and W. H. Weber. “Electromagnetic interactions of molecules with metal surfaces”. In: *Physics Reports* 113.4 (1984), pp. 195–287.

[83] P. Bharadwaj and L. Novotny. “Spectral dependence of single molecule fluorescence enhancement”. In: *Optics Express* 15.21 (2007), pp. 14266–14274.

[84] H. U. Yang, J. D’Archangel, M. L. Sundheimer, E. Tucker, G. D. Boreman, and M. B. Raschke. “Optical dielectric function of silver”. In: *Physical Review B* 91.23 (2015), p. 235137.

[85] N. Noginova, R. Hussain, M. A. Noginov, J. Vella, and A. Urbas. “Modification of electric and magnetic dipole emission in anisotropic plasmonic systems”. In: *Optics Express* 21.20 (2013), pp. 23087–23096.

[86] J. C. Deàk, S. T. Rhea, L. K. Iwaki, and D. D. Dlott. “Vibrational Energy Relaxation and Spectral Diffusion in Water and Deuterated Water”. In: *The Journal of Physical Chemistry A* 104.21 (2000), pp. 4866–4875.

[87] C. A. Hutchison and B. W. Mangum. “Effect of Deuterium Substitution on the Lifetime of the Phosphorescent Triplet State of Naphthalene”. In: *The Journal of Chemical Physics* 32.4 (1960), pp. 1261–1262.

[88] B. R. Judd. “Optical Absorption Intensities of Rare-Earth Ions”. In: *Physical Review* 127 (3 1962), pp. 750–761.

[89] P. A. Tanner. “Some misconceptions concerning the electronic spectra of tri-positive europium and cerium”. In: *Chemical Society Reviews* 42 (12 2013), pp. 5090–5101.

[90] G. Santos, F. J. Fonseca, A. M. Andrade, V. Deichmann, L. Akcelrud, S. S. Braga, A. C. Coelho, I. S. Gonçalves, M. Peres, W. Simões, T. Monteiro, and L. Pereira. “Organic light emitting diodes with europium (III) emissive layers based on β-diketonate complexes: The influence of the central ligand”. In: *Journal of Non-Crystalline Solids. Amorphous and Nanocrystalline Semiconductors* 354 (19-25 2008), pp. 2897–2900.

[91] W. Quirino, R. Reyes, C. Legnani, P. C. Nóbrega, P. A. Santa-Cruz, and M. Cremona. “Eu-β-diketonate complex OLED as UV portable dosimeter”. In: *Synthetic Metals* 161.11 (2011), pp. 964–968.

[92] J. Liu, K. Wang, W. Zheng, W. Huang, C.-H. Li, and X.-Z. You. “Improving spectral response of monocrystalline silicon photovoltaic modules using high efficient luminescent down-shifting Eu^{3+} complexes”. In: *Progress in Photovoltaics: Research and Applications* 21.4 (2013), pp. 668–675.

[93] G. E. Khalil, K. Lau, G. D. Phelan, B. Carlson, M. Gouterman, J. B. Callis, and L. R. Dalton. “Europium beta-diketonate temperature sensors: Effects of ligands, matrix, and concentration”. In: *Review of Scientific Instruments* 75.1 (2004), pp. 192–206.

[94] W. W. Al-Qaysi and A. Duerkop. “A luminescent europium complex for wide-range pH sensors and sensor microtiterplates”. In: *Analyst* 143.13 (2018), pp. 3176–3183.

[95] S. Chen, S. Fan, G. Zhao, X. Fu, and F. Zhang. “A fluorescent functionalized PET fabric with dual-response to aqueous copper and pH”. In: *Reactive and Functional Polymers* 201 (2024), p. 105942.

[96] T.-T. Li, J.-Z. Liu, S.-J. Zheng, F. Jiang, J.-Y. Liu, W.-N. Dong, Y. Zhang, S.-P. Zheng, Y.-N. Li, Z.-N. Wu, and X. Bai. "Heteronuclear lanthanide titanium-oxygen cluster luminescence thermometer with adjustable operating range and sensitivity". In: *Rare Metals* 44.4 (2025), pp. 2438–2449.

[97] A. S. Borukhovich, N. I. Ignat'eva, K. I. Yanushkevich, A. I. Stognii, and Y. A. Fedotova. "Mössbauer spectroscopy study of the EuO:Fe spintronic material". In: *Jetp Letters* 89.4 (2009), pp. 191–193.

[98] C. Belman-Rodriguez, J. Guerrero-Sánchez, J. López-Medina, S. Sharma, N. Tabaray, C. Velez, A. Reyes-Serrato, M. H. Farías, S. A. Aguila, and R. Ponce-Perez. "Europium-Induced Ferromagnetism on Bismuth Germanium Oxide Nanoparticles toward Spintronics Applications". In: *ACS Omega* 10.12 (2025), pp. 11762–11769.

[99] R. Renata. "Optical Properties of Lanthanides in Condensed Phase, Theory and Applications". In: *AIMS Materials Science* 2 (2 2015), pp. 37–60.

[100] M. H. V. Werts, R. T. F. Jukes, and J. W. Verhoeven. "The emission spectrum and the radiative lifetime of Eu^{3+} in luminescent lanthanide complexes". In: *Physical Chemistry Chemical Physics* 4.9 (2002), pp. 1542–1548.

[101] A. N. Carneiro Neto, R. T. Moura Jr., L. D. Carlos, O. L. Malta, M. Sanadar, A. Melchior, E. Kraka, S. Ruggieri, M. Bettinelli, and F. Piccinelli. "Dynamics of the Energy Transfer Process in Eu(III) Complexes Containing Polydentate Ligands Based on Pyridine, Quinoline, and Isoquinoline as Chromophoric Antennae". In: *Inorganic Chemistry* 61.41 (2022), pp. 16333–16346.

[102] G. A. Crosby, R. E. Whan, and J. J. Freeman. "Spectroscopic studies of rare earth chelates". In: *The Journal of Physical Chemistry* 66.12 (1962), pp. 2493–2499.

[103] M. W. Mara, D. S. Tatum, A.-M. March, G. Doumy, E. G. Moore, and K. N. Raymond. "Energy Transfer from Antenna Ligand to Europium(III) Followed Using Ultrafast Optical and X-ray Spectroscopy". In: *Journal of the American Chemical Society* 141.28 (2019), pp. 11071–11081.

[104] G. Crosby, R. Whan, and R. Alire. "Intramolecular energy transfer in rare earth chelates. Role of the triplet state". In: *The Journal of Chemical Physics* 34.3 (1961), pp. 743–748.

[105] D. Chitnis, N. Thejo Kalyani, and S. J. Dhoble. "Comprehensive study on photophysical properties of $Eu(TTA)_3bipy$ phosphor molecularly doped in PMMA and PS matrices". In: *Results in Physics* 13 (2019), p. 102302.

[106] D. Chitnis, N. Thejo Kalyani, and S. J. Dhoble. "Portrayal of structural, thermal and optical properties of pH sensitive $Eu(TTA)_3bipy$ hybrid organic complex for OLEDs". In: *Optik* 130 (2017), pp. 237–244.

[107] X. Zhang. "Spectroscopic studies on the luminescence properties of ternary europium complexes with different ligands". In: *Journal of Luminescence* 130.6 (2010), pp. 1060–1066.

[108] H. J. Batista, A. V. M. de Andrade, R. L. Longo, A. M. Simas, G. F. de Sá, N. K. Ito, and L. C. Thompson. "Synthesis, X-ray Structure, Spectroscopic Characterization, and Theoretical Prediction of the Structure and Electronic Spectrum of $Eu(btfa)_3 \cdot bipy$ and an Assessment of the Effect of Fluorine as a β-Diketone Substituent on the Ligand-Metal Energy Transfer Process". In: *Inorganic Chemistry* 37.14 (1998), pp. 3542–3547.

[109] G. F. de Sá, S. Alves Jr, B. J. P. da Silva, and E. F. da Silva Jr. "A novel fluorinated Eu(III) β-diketone complex as thin film for optical device applications". In: *Optical Materials* 11.1 (1998), pp. 23–28.

[110] I. J. Al-Busaidi, R. Ilmi, D. Zhang, J. D. L. Dutra, W. F. Oliveira, N. K. Al Rasbi, L. Zhou, W.-Y. Wong, P. R. Raithby, and M. S. Khan. "Synthesis and photophysical properties of ternary β-diketonate europium(III) complexes incorporating bipyridine and its derivatives". In: *Dyes and Pigments* 197 (2022), p. 109879.

[111] A. V. S. Lourenço, C. A. Kodaira, E. M. Ramos-Sanchez, M. C. F. C. Felinto, H. Goto, M. Gidlund, O. L. Malta, and H. F. Brito. "Luminescent material based on the $[Eu(TTA)_3(H_2O)_2]$ complex incorporated into modified silica particles for biological applications". In: *Journal of Inorganic Biochemistry* 123 (2013), pp. 11–17.

[112] W. M. Faustino, L. A. Nunes, I. A. A. Terra, M. C. F. C. Felinto, H. F. Brito, and O. L. Malta. "Measurement and model calculation of the temperature dependence of ligand-to-metal energy transfer rates in lanthanide complexes". In: *Journal of Luminescence* 137 (2013), pp. 269–273.

[113] S. K. Kuppusamy, E. Vasilenko, W. Li, J. Hessenauer, C. Ioannou, O. Fuhr, D. Hunger, and M. Ruben. "Observation of Narrow Optical Homogeneous Linewidth and Long Nuclear Spin Lifetimes in a Prototypical [Eu(trensal)] Complex". In: *The Journal of Physical Chemistry C* 127.22 (2023), pp. 10670–10679.

[114] A. G. Bispo-Jr, I. O. Mazali, and F. A. Sigoli. "Sensitization of lanthanide complexes through direct spin-forbidden singlet → triplet excitation". In: *Physical Chemistry Chemical Physics* 24 (22 2022), pp. 13565–13570.

[115] S. Miyazaki, K. Miyata, H. Sakamoto, F. Suzue, Y. Kitagawa, Y. Hasegawa, and K. Onda. "Dual Energy Transfer Pathways from an Antenna Ligand to Lanthanide Ion in Trivalent Europium Complexes with Phosphine-Oxide Bridges". In: *The Journal of Physical Chemistry A* 124.33 (2020), pp. 6601–6606.

[116] S. H. Pan, E. W. Hudson, and J. C. Davis. "^{3}He refrigerator based very low temperature scanning tunneling microscope". In: *Review of Scientific Instruments* 70.2 (1999), pp. 1459–1463.

[117] L. Zhang, T. Miyamachi, T. Tomanić, R. Dehm, and W. Wulfhekel. "A compact sub-Kelvin ultrahigh vacuum scanning tunneling microscope with high energy resolution and high stability". In: *Review of Scientific Instruments* 82.10 (2011), p. 103702.

[118] M. Bianco, A. Balena, M. Pisanello, F. Pisano, L. Sileo, B. Spagnolo, C. Montinaro, B. L. Sabatini, M. De Vittorio, and F. Pisanello. "Comparative study of autofluorescence in flat and tapered optical fibers towards application in depth-resolved fluorescence lifetime photometry in brain tissue". In: *Biomedical Optics Express* 12.2 (2021), pp. 993–1009.

[119] L. Xiang, R. Chen, J. T. M. Tan, V. Nankivell, C. A. Bursill, R. A. McLaughlin, and J. Li. "Identification and removal of system-induced autofluorescence in miniaturized fiber-optic fluorescence endoscopes". In: *PNAS Nexus* 4.8 (2025), pgaf226.

[120] R. Zhang, R. Chouket, A. G. Tebo, M.-A. Plamont, Z. Kelemen, L. Gissot, J.-D. Faure, A. Gautier, V. Croquette, L. Jullien, and T. Le Saux. "Simple imaging protocol for autofluorescence elimination and optical sectioning in fluorescence endomicroscopy". In: *Optica* 6.8 (2019), pp. 972–980.

[121] M. Poirier, S. Thibault, J. Lauzon, and F. Ouellette. "Dynamic and orientational behavior of UV-induced luminescence bleaching in Ge-doped silica optical fiber". In: *Optics Letters* 18.11 (1993), pp. 870–872.

[122] S. LaRochelle, F. Ouellette, and J. Lauzon. "Two-photon excitation and bleaching of the 400 nm luminescence band in germanium-doped-silica optical fibres". In: *Canadian Journal of Physics* 71.1-2 (1993), pp. 79–84.

[123] Doric Lenses Inc. *Application Note: Patch Cord Photobleaching*. Version 1.0.0. 2026.

[124] S. V. Firstov, E. G. Firstova, S. V. Alyshev, V. F. Khopin, K. E. Riumkin, M. A. Melkumov, A. N. Guryanov, and E. M. Dianov. "Recovery of IR luminescence in photobleached bismuth-doped fibers by thermal annealing". In: *Laser Physics* 26.8 (2016), p. 084007.

[125] S. V. Firstov, S. V. Alyshev, A. V. Kharakhordin, K. E. Riumkin, and E. M. Dianov. "Laser-induced bleaching and thermo-stimulated recovery of luminescent centers in bismuth-doped optical fibers". In: *Optical Materials Express* 7.9 (2017), pp. 3422–3432.

[126] L. Zschumme. "Charakterisierung der Photolumineszenz an ausgewählten Eu(III)-Komplexen und der Einfluss von Substrat und Lösungsmittel auf ihr Spektrum". Master's thesis. Karlsruhe Institute of Technology, IQMT, 2026.

[127] qutools GmbH. *Time correlated Single Photon Counting*. 2025. URL: `https://qutools.com/qutag/time-correlated-single-photon-counting/` (visited on 2025–11/0011).

[128] M. L. Bhaumik and L. J. Nugent. "Time-Resolved Spectroscopy of Europium Chelates". In: *The Journal of Chemical Physics* 43.5 (1965), pp. 1680–1687.

[129] S. Miyazaki, M. Gotanda, Y. Kitagawa, Y. Hasegawa, K. Miyata, and K. Onda. "Full Picture of Energy Transfer in a Trivalent Europium Complex with Bidentate β-Diketonate Ligand". In: *The Journal of Physical Chemistry Letters* 15.42 (2024), pp. 10718–10724.

[130] W. Thor, H.-Y. Kai, Y.-H. Yeung, Y. Wu, T.-L. Cheung, L. K. B. Tam, Y. Zhang, L. J. Charbonnière, P. A. Tanner, and K.-L. Wong. "Unearthing the Real-Time Excited State Dynamics from Antenna to Rare Earth Ions Using Ultrafast Transient Absorption". In: *JACS Au* 4.10 (2024), pp. 3813–3822.

[131] M. Valášek, K. Edelmann, L. Gerhard, O. Fuhr, M. Lukas, and M. Mayor. "Synthesis of Molecular Tripods Based on a Rigid 9,9'-Spirobifluorene Scaffold". In: *Journal of Organic Chemistry* 79.16 (2014), pp. 7342–7357.

[132] T. Frauhammer, L. Gerhard, K. Edelmann, M. Lindner, M. Valášek, M. Mayor, and W. Wulfhekel. "Addressing a lattice of rotatable molecular dipoles with the electric field of an STM tip". In: *Physical Chemistry Chemical Physics* 23.8 (2021), pp. 4874–4881.

[133] C. G. Gameiro, C. A. Achete, R. A. Simão, E. F. da Silva, and P. A. Santa-Cruz. "Molecular UV dosimeters of lanthanide complex thin films: AFM as a function of ultraviolet exposure". In: *Journal of Alloys and Compounds* 344.1 (2002), pp. 385–388.

[134] D. Chitnis, N. Thejo Kalyani, and S. J. Dhoble. "Exploration of spectroscopic properties of solvated tris(thenoyltrifluoroacetonate)(2,2'-bipyridine)europium(III)red hybrid organic complex for solution processed OLEDs and displays". In: *Journal of Luminescence* 185 (2017), pp. 61–71.

[135] R. G. Charles and R. C. Ohlmann. "Europium thenoyltrifluoroacetonate, preparation and fluorescence properties". In: *Journal of Inorganic and Nuclear Chemistry* 27.1 (1965), pp. 255–259.

[136] B. M. Flanagan, P. V. Bernhardt, E. R. Krausz, S. R. Lüthi, and M. J. Riley. "A Ligand-Field Analysis of the trensal (H_3trensal = 2,2',2"-Tris(salicylideneimino)triethylamine) Ligand. An Application of the Angular Overlap Model to Lanthanides". In: *Inorganic Chemistry* 41.20 (2002), pp. 5024–5033.

[137] P. V. Bernhardt, B. M. Flanagan, and M. J. Riley. "Isomorphous Lanthanide Complexes of a Tripodal N4O3 Ligand". In: *Australian Journal of Chemistry* 53.3 (2000), pp. 229–231.

[138] F. C. Machado, M. Quintano, C. V. Santos-Jr, A. N. Carneiro Neto, E. Kraka, R. L. Longo, and R. T. Moura Jr. "Theoretical insights into the vibrational spectra and chemical bonding of Ln(III) complexes with a tripodal N_4O_3 ligand along the lanthanide series". In: *Physical Chemistry Chemical Physics* 27 (4 2025), pp. 1794–1803.

[139] E. Lucaccini, L. Sorace, M. Perfetti, J.-P. Costes, and R. Sessoli. "Beyond the anisotropy barrier: slow relaxation of the magnetization in both easy-axis and easy-plane Ln(trensal) complexes". In: *Chemical Communications* 50 (14 2014), pp. 1648–1651.

[140] T. Knaak, C. González, Y. J. Dappe, G. D. Harzmann, T. Brandl, M. Mayor, R. Berndt, and M. Gruber. "Fragmentation and Distortion of Terpyridine-Based Spin-Crossover Complexes on Au(111)". In: *The Journal of Physical Chemistry C* 123.7 (2019), pp. 4178–4185.

[141] T. Dretschkow, D. Lampner, and T. Wandlowski. "Structural transitions in 2,2'-bipyridine adlayers on Au(111)-an in-situ STM study". In: *Journal of Electroanalytical Chemistry* 458.1 (1998), pp. 121–138.

[142] F. Cunha, N. J. Tao, X. W. Wang, Q. Jin, B. Duong, and J. D'Agnese. "Potential-Induced Phase Transitions in 2,2'-Bipyridine and 4,4'-Bipyridine Monolayers on Au(111) Studied by *in Situ* Scanning Tunneling Microscopy and Atomic Force Microscopy". In: *Langmuir* 12.26 (1996), pp. 6410–6418.

[143] P. Stoll, M. Bernien, D. Rolf, F. Nickel, Q. Xu, C. Hartmann, T. R. Umbach, J. Kopprasch, J. N. Ladenthin, E. Schierle, E. Weschke, C. Czekelius, W. Kuch, and K. J. Franke. "Magnetic anisotropy in surface-supported single-ion lanthanide complexes". In: *Physical Review B* 94.22 (2016), p. 224426.

[144] D. D. Chambliss, R. J. Wilson, and S. Chiang. "Nucleation of ordered Ni island arrays on Au(111) by surface-lattice dislocations". In: *Physical Review Letters* 66.13 (1991), pp. 1721–1724.

[145] M. Böhringer, K. Morgenstern, W.-D. Schneider, R. Berndt, F. Mauri, A. De Vita, and R. Car. "Two-Dimensional Self-Assembly of Supramolecular Clusters and Chains". In: *Physical Review Letters* 83.2 (1999), pp. 324–327.

[146] L. W. Liu, K. Yang, W. D. Xiao, Y. H. Jiang, B. Q. Song, S. X. Du, and H.-J. Gao. "Selective adsorption of metal-phthalocyanine on Au(111) surface with hydrogen atoms". In: *Applied Physics Letters* 103.2 (2013), p. 023110.

[147] M. Edmondson and A. Saywell. "Molecular Diffusion and Self-Assembly: Quantifying the Influence of Substrate hcp and fcc Atomic Stacking". In: *Nano Letters* 22.20 (2022), pp. 8210–8215.

[148] X. Zhang, L. Tang, and Q. Guo. "Low-Temperature Growth of C_{60} Monolayers on Au(111): Island Orientation Control with Site-Selective Nucleation". In: *The Journal of Physical Chemistry C* 114.14 (2010), pp. 6433–6439.

[149] K. S. Pedersen, L. Ungur, M. Sigrist, A. Sundt, M. Schau-Magnussen, V. Vieru, H. Mutka, S. Rols, H. Weihe, O. Waldmann, L. F. Chibotaru, J. Bendix, and J. Dreiser. "Modifying the properties of 4f single-ion magnets by peripheral ligand functionalisation". In: *Chemical Science* 5 (4 2014), pp. 1650–1660.

[150] J. Dreiser, G. E. Pacchioni, F. Donati, L. Gragnaniello, A. Cavallin, K. S. Pedersen, J. Bendix, B. Delley, M. Pivetta, S. Rusponi, and H. Brune. "Out-of-Plane Alignment of Er(trensal) Easy Magnetization Axes Using Graphene". In: *ACS Nano* 10.2 (2016), pp. 2887–2892.

[151] S. Goyat, V. Lather, A. Khatkar, P. Ahlawat, P. Kumari, B. Rathee, and R. Kumar. "Photophysical and Optical Properties of β-keto Carboxylate Tb(III) Complexes with Heterocyclic Sensitizers". In: *Journal of Fluorescence* 35.12 (2025), pp. 13783–13802.

[152] J. Repp, G. Meyer, S. M. Stojković, A. Gourdon, and C. Joachim. "Molecules on Insulating Films: Scanning-Tunneling Microscopy Imaging of Individual Molecular Orbitals". In: *Physical Review Letters* 94.2 (2005), p. 026803.

[153] H.-C. Ploigt, C. Brun, M. Pivetta, F. Patthey, and W.-D. Schneider. "Local work function changes determined by field emission resonances: NaCl/Ag(100)". In: *Physical Review B* 76.19 (2007), p. 195404.

[154] K. Lauwaet, K. Schouteden, E. Janssens, C. Van Haesendonck, and P. Lievens. "Dependence of the NaCl/Au(111) interface state on the thickness of the NaCl layer". In: *Journal of Physics: Condensed Matter* 24.47 (2012), p. 475507.

[155] N. Radenović, W. van Enckevort, P. Verwer, and E. Vlieg. "Growth and characteristics of the {111} NaCl crystal surface grown from solution". In: *Surface Science* 523.3 (2003), pp. 307–315.

[156] X. Sun, M. Felicissimo, P. Rudolf, and F. Silly. "NaCl multi-layer islands grown on Au(111)-$(22 \times \sqrt{3})$ probed by scanning tunneling microscopy". In: *Nanotechnology* 19 (2008), p. 495307.

[157] Y. Zhang, Q.-S. Meng, L. Zhang, Y. Luo, Y.-J. Yu, B. Yang, Y. Zhang, R. Esteban, J. Aizpurua, Y. Luo, J.-L. Yang, Z.-C. Dong, and J. G. Hou. "Sub-nanometre control of the coherent interaction between a single molecule and a plasmonic nanocavity". In: *Nature Communications* 8.1 (2017), p. 15225.

[158] W. D. Horrocks and D. R. Sudnick. "Lanthanide ion probes of structure in biology. Laser-induced luminescence decay constants provide a direct measure of the number of metal-coordinated water molecules". In: *Journal of the American Chemical Society* 101.2 (1979), pp. 334–340.

[159] R. E. Kunz and W. Lukosz. "Changes in fluorescence lifetimes induced by variable optical environments". In: *Physical Review B* 21.10 (1980), pp. 4814–4828.

[160] A. S. Borges, E. V. Caliman, J. D. L. Dutra, J. G. Da Silva, and M. H. Araujo. "Structure and luminescent investigation of new Ln(III)-TTA complexes containing N-methyl-ε-caprolactam as ligand". In: *Journal of Luminescence*. SI: Lanthanide spectroscopy 170 (2016), pp. 654–662.

[161] S. Fromme. "Zeitaufgelöste Lumineszenz von Eu^{3+}-Komplexen: Experimentelle Aufbauten". Master's thesis. Karlsruhe Institute of Technology, PHI, 2026.

[162] P. Nockemann, E. Beurer, K. Driesen, R. Van Deun, K. Van Hecke, L. Van Meervelt, and K. Binnemans. "Photostability of a highly luminescent europium β-diketonate complex in imidazolium ionic liquids". In: *Chemical Communications* (34 2005), pp. 4354–4356.

[163] G. Lesly Jiménez, J. L. Reyes-Rodríguez, I. Padilla, G. Alarcón-Flores, and C. Falcony. "Reducing the photo-bleaching effect of a new europium complex embedded in styrene butadiene copolymer". In: *Optical Materials* 76 (2018), pp. 271–277.

[164] T. Pagnot, P. Audebert, and G. Tribillon. "Photostability study of europium dibenzolymethide embedded in polystyrene thin films with high concentration". In: *Chemical Physics Letters* 322.6 (2000), pp. 572–578.

[165] C. G Gameiro, E. F da Silva Jr., S Alves Jr., G. F de Sá, and P. A Santa-Cruz. "Lanthanide complexes dispersed in enamel: a promising new material for photonic devices". In: *Journal of Alloys and Compounds* 323-324 (2001), pp. 820–823.

[166] Q. Xu, L. Li, B. Li, J. Yu, and R. Xu. "Encapsulation and luminescent property of tetrakis (1-(2-thenoyl)-3,3,3-trifluoracetate) europium N-hexadecyl pyridinium in modified Si-MCM-41". In: *Microporous and Mesoporous Materials* 38.2 (2000), pp. 351–358.

[167] P. P. Lima, M. M. Nolasco, F. A. A. Paz, R. A. S. Ferreira, R. L. Longo, O. L. Malta, and L. D. Carlos. "Photo–Click Chemistry to Design Highly Efficient Lanthanide β-Diketonate Complexes Stable under UV Irradiation". In: *Chemistry of Materials* 25.4 (2013), pp. 586–598.

[168] A. Ebert, S. Fromme, L. Burgert, U. Rashid, L. Gerhard, J. Feye, S. K. Kuppusamy, B. Brachnakova, T. Neumann, M. Ruben, P. W. Roesky, M. Seitz, and W. Wulfhekel. "Photophysical properties of Eu3+ complexes approaching electronic contact to a metal surface". In: *arXiv* (2026).

[169] C. Eggeling, J. Widengren, R. Rigler, and C. A. M. Seidel. "Photobleaching of Fluorescent Dyes under Conditions Used for Single-Molecule Detection: Evidence of Two-Step Photolysis". In: *Analytical Chemistry* 70.13 (1998), pp. 2651–2659.

[170] L. L. L. S. Melo, G. P. Castro Jr., M. Navarro, S. M. C. Gonçalves, and A. M. Simas. "Unmasking the UV Photobleaching of β-Diketonate $[Eu(BTFA)_4]^-$ Complexes as an Energy-Driven Photoreduction Process". In: *Inorganic Chemistry* 64.8 (2025), pp. 3842–3856.

[171] N. Noginova, Y. Barnakov, H. Li, and M. A. Noginov. "Effect of metallic surface on electric dipole and magnetic dipole emission transitions in Eu^{3+} doped polymeric film". In: *Optics Express* 17.13 (2009), pp. 10767–10772.

[172] N. M. Shavaleev, S. V. Eliseeva, R. Scopelliti, and J.-C. G. Bünzli. "Influence of Symmetry on the Luminescence and Radiative Lifetime of Nine-Coordinate Europium Complexes". In: *Inorganic Chemistry* 54.18 (2015), pp. 9166–9173.

[173] C. Seward and S. Wang. "Dimeric and polymeric $[Eu(tta)_3L]$ complexes (tta = thenoyltrifluoroacetonato, L = 4,4'-bipyridine, *trans*-1,2-bis(4-pyridyl)ethylene, 4,4'-bipyridine- *N,N'*-dioxide)". In: *Canadian Journal of Chemistry* 79.7 (2001), pp. 1187–1193.

[174] Z. Chen, A. Narita, and K. Müllen. "Graphene Nanoribbons: On-Surface Synthesis and Integration into Electronic Devices". In: *Advanced Materials* 32.45 (2020), p. 2001893.

[175] S. Hembacher, F. J. Giessibl, J. Mannhart, and C. F. Quate. "Revealing the hidden atom in graphite by low-temperature atomic force microscopy". In: *Proceedings of the National Academy of Sciences* 100.22 (2003), pp. 12539–12542.

[176] Y. Zhang, Y.-W. Tan, H. L. Stormer, and P. Kim. "Experimental observation of the quantum Hall effect and Berry's phase in graphene". In: *Nature* 438.7065 (2005), pp. 201–204.

[177] Wikimedia Commons. *File:Electronic band structure of graphene.svg — Wikimedia Commons, the free media repository. Licensed under CC BY-SA 4.0 (https://creativecommons.org/licenses/by-sa/4.0/). No changes made.* 2025. URL: https://commons.wikimedia.org/w/index.php?title=File:Electronic_band_structure_of_graphene.svg&oldid=1122615628 (visited on 06/07/2025).

[178] F. Ullmann and J. Bielecki. "Ueber Synthesen in der Biphenylreihe". In: *Berichte der deutschen chemischen Gesellschaft* 34.2 (1901), pp. 2174–2185.

[179] K. Nakada, M. Fujita, G. Dresselhaus, and M. S. Dresselhaus. "Edge state in graphene ribbons: Nanometer size effect and edge shape dependence". In: *Physical Review B* 54 (24 1996), pp. 17954–17961.

[180] O. V. Yazyev, R. B. Capaz, and S. G. Louie. "Theory of magnetic edge states in chiral graphene nanoribbons". In: *Physical Review B* 84.11 (2011).

[181] M. Pizzochero, K. Čerņevičs, G. Borin Barin, S. Wang, P. Ruffieux, R. Fasel, and O. V. Yazyev. "Quantum electronic transport across 'bite' defects in graphene nanoribbons". In: *2D Materials* 8.3 (2021), p. 035025.

[182] M. Gille, A. Viertel, S. Weidner, and S. Hecht. "Modular Synthesis of Monomers for On-Surface Polymerization to Graphene Architectures". In: *Synlett* 24.02 (2013), pp. 259–263.

[183] C. Zhang, E. Kazuma, and Y. Kim. "Atomic-Scale Visualization of the Stepwise Metal-Mediated Dehalogenative Cycloaddition Reaction Pathways: Competition between Radicals and Organometallic Intermediates". In: *Angewandte Chemie International Edition* 58.49 (2019), pp. 17736–17744.

[184] M. Ammon, M. Haller, S. Sorayya, and S. Maier. "On-Surface Synthesis of Porous Carbon Nanoribbons on Silver: Reaction Kinetics and the Influence of the Surface Structure". In: *ChemPhysChem* 20.18 (2019), pp. 2333–2339.

[185] M. Fritton, D. A. Duncan, P. S. Deimel, A. Rastgoo-Lahrood, F. Allegretti, J. V. Barth, W. M. Heckl, J. Björk, and M. Lackinger. "The Role of Kinetics versus Thermodynamics in Surface-Assisted Ullmann Coupling on Gold and Silver Surfaces". In: *Journal of the American Chemical Society* 141.12 (2019), pp. 4824–4832.

[186] Z. Yang, L. Fromm, T. Sander, J. Gebhardt, T. A. Schaub, A. Görling, M. Kivala, and S. Maier. "On-Surface Assembly of Hydrogen- and Halogen-Bonded Supramolecular Graphyne-Like Networks". In: *Angewandte Chemie International Edition* 59.24 (2020), pp. 9549–9555.

[187] Z.-Y. Yi, X.-Q. Yang, J.-J. Duan, X. Zhou, T. Chen, D. Wang, and L.-J. Wan. "Evolution of Br$\cdots$Br contacts in enantioselective molecular recognition during chiral 2D crystallization". In: *Nature Communications* 13.5850 (2022).

[188] L. Xing, W. Jiang, Z. Huang, J. Liu, H. Song, W. Zhao, J. Dai, H. Zhu, Z. Wang, P. S. Weiss, and K. Wu. "Steering Two-Dimensional Porous Networks with σ-Hole Interactions of Br$\cdots$S and Br$\cdots$Br". In: *Chemistry of Materials* 31.8 (2019), pp. 3041–3048.

Acknowledgments

First of all, I have to thank **Prof. Dr. Wulf Wulfhekel** for his constant encouragement and expert advice over the past years. It goes without saying that this work would not have been possible without his belief in the project and his dedication to my professional development. When I joined his group, I was convinced that this was the best possible position for me to obtain my PhD. I still consider this to be true.

Second, I also thank my former supervisor **Prof. Dr. Axel Enders** for his constant support during my time in Bayreuth and also afterwards.

I furthermore want to thank **Prof. Dr. David Hunger** for taking the time to be my co-supervisor and providing feedback on my progress during our regular meetings, which I greatly enjoyed.

I also have to mention the collaboration with **Prof. Dr. Michael Seitz** who shared his expertise and men power and helped us to enter the field of research when we were just starting.

A special thank-you goes to **Dr. Lukas Gerhard** who I truly enjoyed working with, on a professional and personal level. He was a great support in the everyday lab work and always found some time in his busy schedule when he was needed, even if this meant sacrificing his sparse free time.

Of course I thank all of my colleagues for always lending a helping hand when needed and being enjoyable people in general.

I also thank **Paul Maier** for always being helpful when needed without hesitation and also in particular for coating the mirror tips and substrates.

I would also like to thank **Dr. Barbora Brachnakova**, **Dr. Julia Feye** and **Dr. Senthil Kumar Kuppusamy** for providing the betadiketonate based complexes.

I furthermore have to thank **Timo Neumann** and **Lisa Biener** for providing the platform complexes and also for some nice conversations during conferences.

I thank **Lisa Burgert** and **Simon Fromme** for their great work. Their support and genuine interest for the topic accelerated our experiments immensely. Both of them saved me a lot of work and I wish them all the best for whatever is to come after finishing their Master's degrees.

Of course I thank all collaborators not mentioned so far that contributed to my publications with their expertise.

I am furthermore thankful for the financial support from the Deutsche Physikalische Gesellschaft and for the 4f4f SFB which fortunately organized more than enjoyable conferences and tried to reduce additional workload as much as possible.

I have to thank **Dr. Richard Kellnberger**, **Thomas Bergler** and **Kai Widmaier** for sticking with me since my undergraduate studies. I appreciate their professional advice but most of all their friendship.

I am thankful for my parents **Petra Ebert** and **Hans-Jürgen Ebert** who obviously managed to raise me halfway decently and enabled me to study. I am also thankful for my grandparents **Margot Senese** and late **Giancarlo Senese**. My happiest childhood memories are connected to them.

Finally, I express true gratitude for the emotional support from my family, in particular my sister **Tatjana Grabl** and my partner **Anna Holst**. In stressfull times, which there are plenty as a PhD. student, it is easy to lose focus on the things that truly matter in life. Thank you for always reminding me.